TABLE OF CONTENTS

Page

LIST OF TABLES

Page

LIST OF FIGURES

LIST OF ABREVIATIONS

AUPALE	AUgmentation de la Puissance des Alternateurs Existants
CAD	Computer Aided Design
CFD	Computational Fluid Dynamics
CHTC	Convective Heat Transfer Coefficient
CVFEM	Control Volume based Finite Element Method
DNS	Direct Numerical Simulation
GGI	General Grid Interface
IEA	International Energy Agency
IREQ	Institut de Recherche d'Hydro-Québec
LES	Large Eddy Simulation
LPTN	Lumped-Parameters Thermal Network
LRNM	Low-Reynolds Number Model
MFR	Multiple Frames of References
PIV	Particle Image Velocimetry
RANS	Reynolds-Averaged Navier-Stokes
RNG	ReNormalization Group
WF	Wall Function
SKE	Standard $k-\varepsilon$
SKO	Standard $k-\omega$
SST	Shear Stress Transport

LISTE OF SYMBOLS AND UNITS OF MEASUREMENTS

h_{total}	Total specific enthalpy (J)
c_p	Specific heat capacity ($J \cdot kg^{-1} \cdot K^{-1}$)
h	Heat transfer coefficient ($W \cdot m^{-2} \cdot K^{-1}$)
λ	Thermal conductivity ($W \cdot m^{-1} \cdot K^{-1}$)
p	Instantaneous pressure (Pa)
P	Time-averaged pressure (Pa)
Pr_t	Turbulent Prandtl number (-)
q_w	Wall heat flux ($W \cdot m^{-2}$)
T	Temperature (K)
u_i	Instantaneous velocity component ($m \cdot s^{-1}$)
U_i	Time-averaged velocity component ($m \cdot s^{-1}$)
u_i'	Fluctuation velocity component ($m \cdot s^{-1}$)
y^+	Dimensionless wall distance (-)
ε	Turbulent kinetic energy dissipation rate ($m^2 \cdot s^{-3}$)
ε_{ijk}	third-order alternating tensor (-)
θ	Angular coordinate (°)
ν	Kinematic viscosity ($m^2 \cdot s^{-1}$)
ρ	Density ($kg \cdot m^{-3}$)
ω	Specific dissipation rate (s^{-1})

μ	Molecular dynamic viscosity ($kg \cdot m^{-1} \cdot s^{-1}$)
μ_t	Turbulent dynamic viscosity ($kg \cdot m^{-1} \cdot s^{-1}$)

INTRODUCTION

Hydroelectric power is currently the most common form of renewable energy and plays a very important role in global electric power generation. It accounts for approximately 17.5% of total electricity production, and almost 85% of electricity produced from renewable sources (Internaltional Energy Agency, 2017).

Hydroelectric power uses unique technology that allows us to store the energy in a reservoir and extracts the power on demand, as illustrated in Figure 0.1. Thus, it allows for a flexible production, where the output can be controlled by adjusting the mass flow rate exiting from the stored reservoir into the hydraulic turbine. Moreover, hydroelectric power is associated with a weak emission of greenhouse gas, and therefore it has a less destructive effect on the environment.

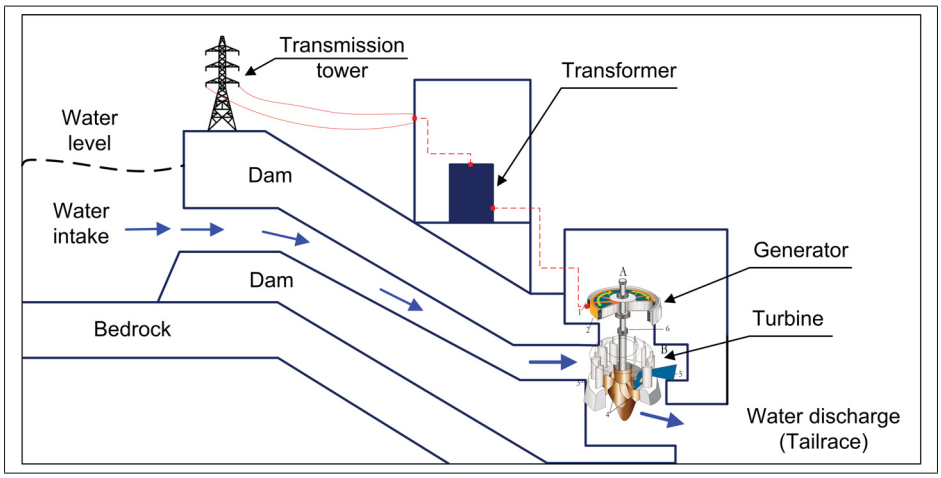

Figure 0.1 Scheme of the hydroelectric power plant.

One of the most important sets of equipment in hydro power plants is the turbine-generator group, illustrated in Figure 0.2. The hydraulic turbine extracts a part of mechanical energy of water flow from the waterfall and transmits it to the generator through the rotating shaft, on which the rotating part of the generator, the rotor, is attached. The function of hydro-generators is to convert this mechanical energy into electricity.

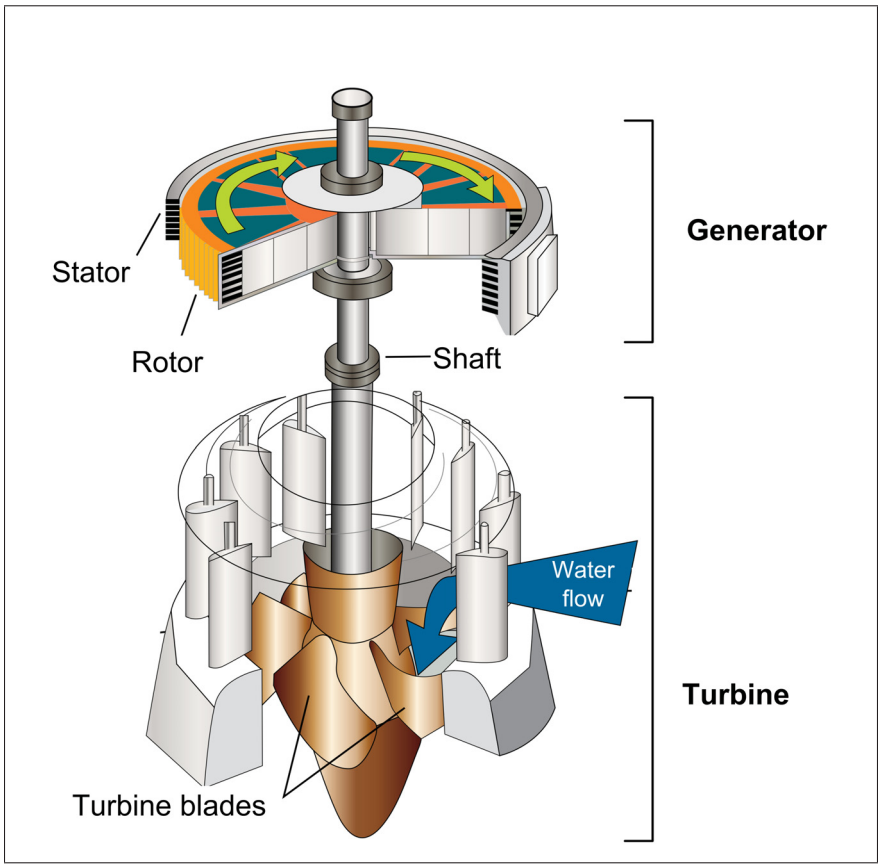

Figure 0.2 Illustration of turbine-generator group."Hydraulic turbine and electrical generator, cut-away view," by U.S. Army Corps of Engineers, 2008, Public Domain.

Hydro-generators are high performance electrical machines, they have an efficiency rate up to 98%. However, during the conversion from the mechanical energy into electricity, a certain amount of energy is lost (Traxler-Samek *et al.*, 2010a). The power losses associated with the electricity production by hydro-generators include:

- Electrical losses: the losses generated as a result of the electrical resistance in the rotor and stator windings.
- Magnetic losses: the losses generated as a result of the rotating magnetic field, appeared due to the motion of the rotor core relatively to the stator core.

- Mechanical losses: consists of the bearing loss and the windage losses caused by the air friction on the solid surface.

These losses manifest mainly in the form of volumetric heat source and cause the temperature rise in the solid components of hydro-generators. It is well known that the thermal performance and lifetime of the generator depend strongly on the maximum temperature of solid components, particularly thermally-limited dielectric insulators. As a result, it is required to consider the thermal aspect, besides the mechanical and electromagnetic analysis in the design and upgrading of hydro-generators.

In order to maintain the maximum temperature within the critical value, the heat generated must be extracted away from the machine. The cooling of the generator is conventionally assured by a forced convection using a closed-loop cooling air circuit passing over solid components. After passing through the active components of the generator (rotor ventilation ducts, salient pole surfaces, stator ducts, windings, etc.), the air directs towards the radiators, where the accumulated heat is dissipated. The energy required to maintain this flow induces the windage loss, that accounts for 20%-30% of total losses in the generator (Toussaint *et al.*, 2011). As a consequence, an efficient ventilation system is also an important attribute in the generator's design and uprating.

The province of Québec benefits from an abundant water resource in the form of 500,000 lakes and 4,500 rivers that cover 12% of its surface area, which motivates the installation of many hydroelectric power plants over provincial territory. Hydro-Québec is currently operating 63 hydroelectric power units with an output capacity of 36 908 MW, accounting for 99% capacity of its total production (Hydro-Québec, 2017). The majority of hydroelectric power plants in Québec were built before the 1970s. At that time, the electrical machine designers did not benefit from the highly accurate measurement instruments, nor the numerical analysis techniques which are now widely available, such as the finite element analysis (FEA) or computational fluid dynamics (CFD). Instead, engineers mainly relied on past experience and on empirical

approach to build the machines. Consequently, large safety factors have been assigned to the electrical machines due to the uncertainty of the calculation method. With the aid of novel technologies, these factors of safety can be reduced, allowing for an improvement of the power rating of existing generators.

For this reason, Hydro-Québec started the project AUPALE (Augmentation de la Puissance des Alternateurs Existants) in 2002 at the company's research center, *Institut de Recherche d'Hydro-Québec (IREQ)*. The ultimate goal of this project is to evaluate the potential of increasing the rated maximum capacity of certain existing generators without compromising the machines' lifetime. As the power of generators increases, the power losses consequently elevate and result in a temperature rise, which might damage the generator or cause an overheating problem. The AUPALE project therefore has also been required to assess the impact of this power upgrading on the lifetime of generators. This project is a multi-physics consideration of the hydro-generator as an entire single unit, involving the electromagnetic, structural, and thermo-fluid aspects. The electromagnetic simulations allow one to calculate the power losses in the active components of the machine, then transferred to an in-house code developed at IREQ to calculate the temperature field in solid components. In order to accomplish the thermal analysis, one requires an understanding of convective cooling on the surfaces of the active solid components of the generator. An investigation of the ventilation flow in the machine is thus important to fully predict the thermal performance of the machine. Due to safety reasons, the access to power plants to carry out flow measurements is very limited. Moreover, it is frequently necessary to stop or remove a part of the generator to install measurement instruments. Since a halt of the generator's operation is highly costly, the instrumentation must be synchronized with a maintenance period, which is strictly time-bounded. To date, the measurement of the air ventilation flow rate at power plants is insufficient to fully analyze the ventilation circuit.

The computational fluid dynamics (CFD) is a cutting-edge tool that allows one to carry out the

ventilation flow analysis with high efficiency without facing the inconvenience of measuring at power plants. However, due to the geometrical complexity of generators, the CFD modelling contains numerous uncertainties and a validation procedure is thus required to increase the reliability of numerical methodology. To this end, a scale rotating model of the hydro-generator prototype was designed and built at IREQ to perform flow and thermal measurements.

The experimental rotating scale model is illustrated in Figure 0.3. Since the purpose of the study on the airflow in the experimental model is to develop and validate the numerical and experimental methodology for this specific ventilation flow type, many simplifications have been made in the experiments in order to facilitate the design, fabrication, CFD analysis, and PIV measurements. The simplifications that were made to the experimental model on one hand aim to enable the measuring procedure, on the other hand to reduce the geometrical complexity for meshing in the numerical approach.

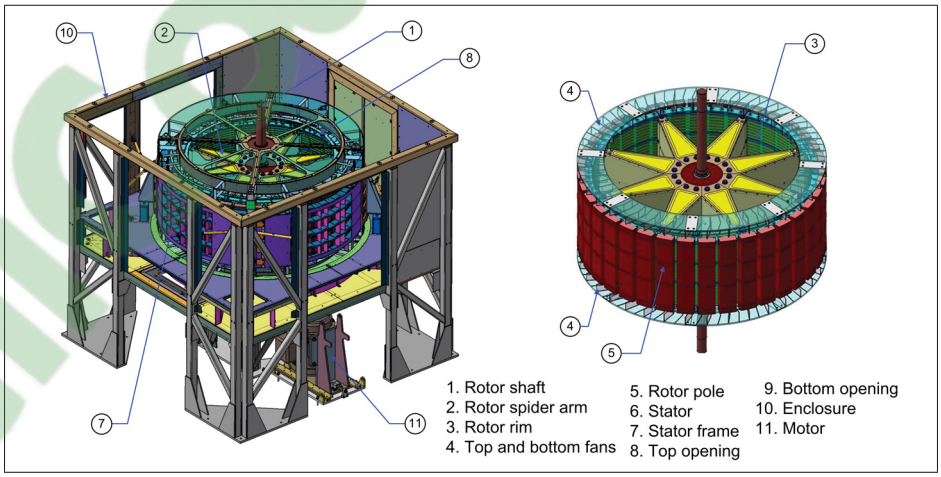

Figure 0.3 Experimental rotating scale model.

In order to analyze the heat transfer phenomena on the surface of the rotor pole, one of the poles is equipped with heating elements to generate a heat flux at its surface. The pole surface temperature is measured with thermistors and a high-frequency pyrometer probe placed in the stator ducts. Then, the temperature distribution in the solid rotor and the resulting heat flux

at the pole surface, q''_w, were calculated with the ANSYS−CFX code, using the measured wall temperature, T_w, as a boundary condition for the outer surface of the heated pole. Finally, the convective heat transfer coefficient (CHTC) distribution on the pole surfaces was obtained from $h = q''_w/(T_w - T_{ref})$, where T_{ref} is the fluid reference temperature. More detailed information on the experimental setup and procedure to determine the CHTC distribution can be found in Torriano *et al.* (2014). In the current study, the CHTC values obtained by the experiment were used to validate the numerical model.

Objectives of this thesis:

This research aims to address one of the most challenging problems in the thermal analysis of rotating electrical machines; the flow and heat transfer features in the air gap region. The air gap convective flow exhibits an extremely complex flow structure, where the interaction between the rotor and stator components has a strong impact. In addition, this region is critically important to the thermal performance prediction of the machine, since a concentration of magnetic loss is found. However, it is very challenging for the numerical modelling to accurately predict the flow and thermal characteristics in this region. The objective of this work is to characterize the turbulent flow and heat transfer in a hydro-generator rotor-stator system. The air gap region is of particular interest. To achieve these goals, the objectives of this thesis are defined as:

- Develop a strategy to predict the fluid flow in the rotor-stator air gap region as accurately as possible. The air gap between the rotor and the stator is important as there is a high concentration of magnetic loss and a high chance of hot spot presence in this area. However, it is difficult to perform measurements with the required instruments given the narrow physical space. On the other hand, the aerodynamic interaction between the rotating and stationary parts of the machine also present a challenge in CFD simulations.
- Perform numerical simulations and validate the numerical results using simplified configuration, excerpted from the rotating full scale model. Since the flow structure in the air gap is

extremely complex and challenging for numerical modelling, a validation procedure should be performed to justify the numerical methodology for this particular application.

- Evaluate the effects of different numerical models on the accuracy of flow and thermal fields predictions, based on which the thesis provides a recommended "best-practice" guide for the CFD simulations of hydro-generators.

Structure of thesis:

This thesis mainly focuses on developing a better understanding of the turbulent convective cooling process in the hydro-generator scale model using numerical simulations, in particular the flow and thermal field in the air gap region. The thermal analysis of hydro-generators is a complex phenomenon and contains a great deal of challenges that cannot be entirely addressed within a thesis, therefore, this work should be considered as a contribution to the "best-practice" of CFD modelling for the convective cooling of hydro-generators. The core part of this dissertation is presented as a series of elaborated journal manuscripts that have been submitted for publication. The entire thesis is composed of five chapters and is organized as follows:

In the Introduction section of the thesis, an overview of the ventilation flow and thermal aspects of the hydroelectric generator is illustrated in a multi physics scenario with the electromagnetic and structural analysis. The experimental rotating scale model is introduced with main parameters, that is used to produce measured data to validate the numerical results. In the next chapter, the mathematical model of the convection phenomenon in the machine is given in the context of conjugate heat transfer methodology. The governing equations of fluid dynamics, with consideration given to the turbulence effect, and the solid heat conduction equations, are presented. In Chapter 2, the literature review on the computational fluid dynamics studies for the air ventilation flow and heat transfer analysis in hydro-generators is reported. In Chapter 3, the methodology and short description of analysis performed in the next chapters are provided. The first study in Chapter 4 presents an assessment of a two-dimensional simplified model of

the hydro-generator rotor-stator configuration with respect to the prediction of the flow and thermal fields. Different multiple frames of reference approaches, both steady state and unsteady models, are tested to evaluate their accuracy in predicting the flow fields in the air gap and stator ducts regions. In addition, the behaviours of various steady state RANS turbulence models (i.e. the standard $k-\varepsilon$, the RNG $k-\varepsilon$, the Wilcox's $k-\omega$, and the SST $k-\omega$) are checked with respect to the prediction of convective heat transfer coefficient distribution on the rotor pole surface. Last but not least, the effect of conjugate heat transfer methodology to the thermal performance prediction is discussed in relation to the local flow features.

Based on the results given in the first article, the second article in Chapter 5 reports an analysis of flow and thermal fields in a simplified model, which is extended in the axial direction to take into account the three-dimensional flows in the air gap region. The rotor-stator coupling is handled with the steady state mixing plane interface model. The mesh sensitivity study is performed and the dimensionless wall distance effect is analyzed. A validation of numerical results is carried out by comparing the convective coefficient values with the experimental data and a detailed error analysis of the CFD modelling is given. Most importantly, based on this comparison, the appropriateness of RANS-based turbulence models for the convective heat transfer prediction in the current configuration is assessed.

As a continuation of the previous study, the sensitivity of the rotor-stator interface location and the influence of thermal boundary conditions on the prediction of the rotor pole face temperature are reported in Chapter 6. The mixing plane model is employed at the rotor-stator interface and the discontinuity of the flow field through this interface is discussed. The dependencies of the convective heat transfer coefficient and windage loss as a function of rotor-stator location are evaluated. Finally, the impact of the counter-rotating vortex in the meridional planes as well as the effect of the inclusion of solid domain to the numerical model on the temperature field calculation in the solid are thoroughly discussed.

Following the results and discussions in the last three chapter, the conclusions and recommen-

dation for future work are given in the next section. Finally, in Appendix I and Appendix II the mathematical formulations of the Reynolds-averaged Navier-Stokes turbulence closures and Reynolds stresses in the cylindrical coordinates are provided, respectively.

CHAPTER 1

MATHEMATICAL AND NUMERICAL MODELS

The partial differential equations governing the turbulent flow in rotating machineries are very complex and cannot be solved analytically, but only numerically. Computational Fluid Dynamics is considered as an interdisciplinary branch of science which employs the numerical methods to solve the fluid dynamics equations by means of computing infrastructure. In this chapter, a brief summary of the CFD concepts is given, beginning with the mathematical model that governs the fluid flow in rotating machines. In this chapter, the details on characteristics of numerical models, including advantages and disadvantages of each model, are also discussed in detail.

1.1 Fluid dynamics governing equations

The governing equations of fluid flow consist of the continuity, momentum, and energy equations. These equations represent the mathematical statements of the conservation laws of physics: the conservation of mass, the conservation of linear momentum, and the conservation of energy, are given for incompressible flows using the Einstein notation as follows:

$$\frac{\partial}{\partial x_j}\left(\rho u_j\right) = 0 \tag{1.1}$$

$$\frac{\partial}{\partial t}(\rho u_i) + \frac{\partial}{\partial x_j}(\rho u_i u_j) = -\frac{\partial p}{\partial x_i} + \frac{\partial \tau_{ij}}{\partial x_j} + S_{M,i} \tag{1.2}$$

$$\frac{\partial}{\partial t}(\rho h_{tot}) - \frac{\partial p}{\partial t} + \frac{\partial}{\partial x_j}\left(\rho u_j h_{tot}\right) = \frac{\partial}{\partial x_j}\left(\lambda_f \frac{\partial T}{\partial x_j}\right) + \frac{\partial}{\partial x_j}\left(\tau_{ij} u_i\right) + S_E \tag{1.3}$$

where ρ is the fluid density, u_j are velocity components, p is the static pressure, τ_{ij} is the shear stress tensor, $S_{M,i}$ is the momentum source term, h_{total} is the specific total enthalpy for ideal gas, and τ_{ij} is the shear viscous stress tensor.

1.2 Numerical models

1.2.1 Turbulence models

Most fluid motions found in engineering applications are turbulent flows, which are characterized by many physical properties (Ferziger & Peric, 2002). Historically, turbulent flows were primarily studied using experimental approaches, in which overall quantities such as time-averaged friction coefficients or heat transfer are quantified. However, there are some parameters that are almost impossible to measure even using cutting-edge instruments, and others cannot be made with sufficiently desired precisions. Consequently, the numerical approach to model turbulent flows is required for engineering applications.

Direct numerical simulation (DNS)

DNS is considered the most accurate approach to characterize turbulence because it solves the Navier-Stokes equations without any approximation other than the numerical discretization. In such simulations, all length and time scales involved in the flow are resolved. In order to assure that all significant structures of the turbulence have been captured, on the one hand the computational domain must be at least as large as the largest turbulent eddy or the integral scale L, on the other hand the mesh size must be no larger than the smallest length scales, the Kolmogorov scale η. Tennekes (1972) proved that the number of computational nodes in each direction must be proportional to at least $L/\eta \approx Re_L^{3/4}$, where Re_L is the Reynolds number based on an integral scale. Since the number of nodes must be used in each three coordinate directions, and the time step is related to the grid size, the cost of simulation scales is Re_L^3. Because the number of grid points used in computation is limited by the processing speed and memory, direct numerical simulation is only possible for flows at a low Reynolds number and for geometrically simple cases. For the case of hydroelectric generators that have an extremely complex geometry, a Reynolds number of 2.6×10^4 is typically found, the DNS are thus not applicable for this application.

Large eddy simulation (LES)

An alternative approach of DNS is the large eddy simulation approach, which was firstly pro-

posed and developed by Smagorinsky (Wilcox, 1988). In LES approach, the large scale motions of the turbulent flow are directly solved meanwhile small scale ones (sub-grid scale) are modelled, which results in a significant reduction in computational cost in comparison with DNS. LES approach is more accurate than the Reynold-averaged Navier-Stokes (RANS) simulations since the large eddies of the turbulent flow are much more energetic and provide most of momentum transport and turbulent mixing. Furthermore, compared to the large eddies the small scale motions are more isotropic and homogeneous, and therefore modelling the sub-grid scale eddies is less computational costly than modelling all scales in a single closure as in the RANS approach. LES is not applicable for the current configuration since it is too computationally expensive.

Reynolds-averaged Navier-Stokes turbulence models (RANS)

The DNS and LES approaches produce very detailed structure of turbulence, which on the one hand is very useful for analysis, but on the other hand, those features have far more information than engineers needs. For industrial applications, RANS simulations have been preferred. RANS equations are derived based on the Reynolds decomposition of the turbulent flow field. In this context, every flow variable ϕ can be expressed as a sum of a time-averaged value Φ and an instantaneous fluctuation $\phi'(x_i,t)$ (Ferziger & Peric, 2002):

$$\phi(x_i,t) = \Phi(x_i,t) + \phi'(x_i,t) \tag{1.4}$$

Applying this decomposing operation to the instantaneous velocity u_i and instantaneous pressure p:

$$u_i(x_i,t) = U_i(x_i,t) + u_i'(x_i,t) \tag{1.5}$$

$$p(x_i,t) = P(x_i,t) + p'(x_i,t) \tag{1.6}$$

Substituting these equations into the Navier-Stokes equations yields the Reynold-averaged Navier-Stokes equations. The averaged continuity, momentum, and energy equations, for in-

compressible flow without body forces, are written in the index notation as follows:

$$\frac{\partial}{\partial x_j}\left(\rho U_j\right) = 0 \tag{1.7}$$

$$\frac{\partial}{\partial t}(\rho U_i) + \frac{\partial}{\partial x_j}(\rho U_i U_j) = -\frac{\partial P}{\partial x_i} + \frac{\partial}{\partial x_j}\left(\tau_{ij} - \rho\overline{u_i' u_j'}\right) + S_{M,i} \tag{1.8}$$

$$\frac{\partial}{\partial t}(\rho h_{tot}) - \frac{\partial p}{\partial t} + \frac{\partial}{\partial x_j}\left(\rho U_j h_{tot}\right) = \frac{\partial}{\partial x_j}\left(\lambda_f \frac{\partial T}{\partial x_j} - \rho\overline{u_j' h}\right) + \frac{\partial}{\partial x_j}\left[U_i\left(\tau_{ij} - \rho\overline{u_i' u_j'}\right)\right] + S_E, \tag{1.9}$$

There are several possibilities to approximate the Reynolds stresses tensor $\tau_{ij}^{Re} = -\rho\overline{u_i' u_j'}$, including deriving equations for the higher-order correlations, e.g. for Reynolds stress tensor, however this approach still contains unknown correlations which require additional approximations. These approaches will not be covered in this thesis and only models based on the Boussinesq's approximation are considered.

Eddy viscosity models (EVM) are based on the Boussinesq's hypothesis that the turbulent stress tensor can be expressed in terms of the mean strain rate in a similar manner as the viscous stress for the Newtonian isotropic fluid, except that the molecular viscosity is replaced by the turbulent eddy viscosity. The turbulent stresses and turbulent heat flux are obtained using the effective viscosity approximation, which relates the velocity gradients and the turbulent eddy viscosity to the the Reynolds stresses, and the enthalpy gradient and turbulent conductivity to the turbulent heat fluxes:

$$-\rho\overline{u_i' u_j'} = \mu_t\left(\frac{\partial U_i}{\partial x_j} + \frac{\partial U_j}{\partial x_i}\right) - \frac{2}{3}k\delta_{ij} \tag{1.10}$$

$$-\rho\overline{u_j' h} = \frac{\mu_t}{Pr_t}\frac{\partial h}{\partial x_j} \tag{1.11}$$

The molecular thermal conductivity is now modified as effective conductivity to account for the effect of turbulence, i.e. $\lambda_{eff} = \lambda_f + c_p\mu_t/Pr_t$, where c_p is the specific heat capacity of air, and Pr_t is the turbulent (0.85) Prandtl number.

The six unknown turbulent stress components are now replaced with only one new unknown, the turbulent viscosity μ_t, which is computed using the turbulence closure models. Because

of convergence problem, only two-equation turbulence models based on the eddy-viscosity approximation are employed in this work. The mathematical formulations of these models are presented in the Appendix.

The standard $k-\varepsilon$ model (Jones & Launder, 1973) is the most popular turbulence closure that has been used and validated for industrial flows. It has obtained great success in the calculation of thin shear layer recirculating flows. However, this model shows only moderate agreement for unconfined flows, where the rate of production of turbulent kinetic energy is much lower than the rate of dissipation. The standard $k-\varepsilon$ model as well as other turbulence models based on Boussinesq's isotropic eddy approximation have demonstrated limitations in modelling the swirling flows and flows with large strain, such as highly curved flows and divergence passages (Wilcox, 1993). Finally, this model was found to be non applicable for the rotating flows since the body forces, appearing in the frame of reference transformation, were neglected (Versteeg & Malalasekera, 2007).

The Re-Normalized Group (RNG) $k-\varepsilon$ model is a modification of the standard $k-\varepsilon$ model, and displays a great deal of improvements and advantages since it takes into account the effects of the small scale eddies by means of a random function in the Navier-Stokes equation. The RNG model systematically removes the small-scale eddies from the governing equation by replacing their effects by larger-scale eddies and modified viscosity. This model was reported to have very good predictions of the flow over a forward facing step (Yakhot *et al.*, 1992). The RNG model has demonstrated an improvement in predicting the recirculation length of separating flows, however fails to predict the accelerating flows. Also, compared to the standard $k-\varepsilon$ model, the RNG modification improves the flow predictions for the duct expansion case, but does not show its enhancement in a duct contraction one.

The Wilcox's $k-\omega$ model is developed by Wilcox (1988) and is considered the most common alternative model of the standard $k-\varepsilon$ model, which employs the turbulence frequency $\omega = \varepsilon/k$ as the second characteristic of the turbulence after the turbulent kinetic energy k. This model provides the ability to integrate to the wall, which eliminates the requirement of wall damping function in low Reynolds number applications. Nevertheless, the results produced by the Wilcox's $k-\omega$ model tend to be dependent on the assumed free stream value of ω (Menter,

1994).

The Shear Stress Transport (SST) $k-\omega$ model was originally developed by Menter (1994), in which the Wilcox's $k-\omega$ equation is solved for the boundary layers region and the standard $k-\varepsilon$ is employed elsewhere. This combination is realized in the SST model to exploit the advantages of each turbulence model for the local region: the $k-\omega$ model does not require the damping function but is found to be sensitive to the free-stream turbulence; whereas the $k-\varepsilon$ model does not possess this deficit, however, the performance of the $k-\varepsilon$ model in the boundary layer zone is relatively limited for the flows with strong adverse pressure gradients. The SST model has gained popularity for the industrial applications due to its performance for the complex flows (Hellsten, 1998).

1.2.2 Boundary layer modelling

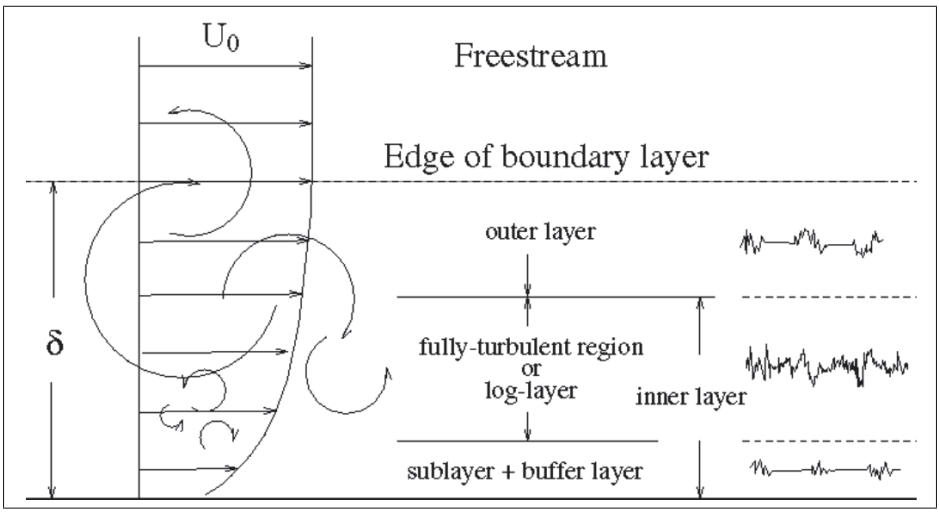

Figure 1.1 Schematic illustration of boundary layer structure (Ferziger & Peric, 2002).

The profiles of the turbulence parameters, such as the turbulence kinetic energy and the turbulence dissipation, normally peak near the wall (Ferziger & Peric, 2002) and are found to be difficult to capture. In CFD simulations, there are two main approaches for modelling flow parameters in the near-wall region: the wall-functions (WF) and the low-Reynolds number models (LRNM). The difference between these models is the way that the boundary layer is

taken into account. The boundary layer consists of an inner layer, including the viscous sub-layer, the buffer layer and the fully-turbulent outer layer (or the log-law layer), as illustrated in Figure 1.1. In the wall-functions model, the semi-empirical formulae are employed to bridge the region between the wall and the logarithmic layer, resulting in much coarser grids being used. Meanwhile, the low-Reynolds number modelling refers to a method that resolves the whole boundary layer by putting computational nodes in each parts of it, which requires a very high mesh resolution close to the wall.

Standard wall-functions

The standard wall-functions in ANSYS CFX are an extension of the method developed by Launder and Spalding, and are used for the ε-based turbulence models. These functions connect the wall condition, e.g. the wall shear stress, to the dependent variables at the near-wall mesh node, which is presumably located in the fully-turbulent region of boundary layer. The wall-functions are based on the universal law of the wall in the logarithmic layer, which is expressed by:

$$u^+ = \frac{U_t}{u_\tau} = \frac{U_t}{(\tau_w/\rho)^{1/2}} = \frac{1}{\kappa} ln(y^+) + C \tag{1.12}$$

where:

$$y^+ = \frac{\rho\,(\tau_w/\rho)^{1/2} y}{\mu} \tag{1.13}$$

u^+ is the near wall velocity, U_t is the known velocity tangent to the wall at the distance y from the wall, τ_w is the wall shear stress, κ is the von Karman constant, C is the constant depending on the wall roughness, and y^+ is the dimensionless wall distance used to characterize the mesh resolution near the wall.

The standard wall functions in Equation 1.12 bares the problem that it becomes singular at the separation point ($\tau_0 = 0$). An alternative velocity scale u^* based on turbulence kinetic energy can be used, instead of u_τ:

$$u^* = C_\mu^{1/4} k^{1/2} \tag{1.14}$$

Based on this definition, the absolute value of the wall shear stress τ_w, is obtained from:

$$\tau_w = \rho u^* u_\tau = \frac{U_t C_\mu^{1/4} k^{1/2}}{\frac{1}{\kappa} ln(y^*) + C} \tag{1.15}$$

where y^* is defined as:

$$y^* = \frac{\rho C_\mu^{1/4} k^{1/2} y}{\mu} \tag{1.16}$$

The major drawbacks of the wall-functions model is that the prediction depends on the location of the point closest to the wall and is sensitive to the near-wall meshing. Thus, ANSYS CFX offers the *scalable wall-functions* model which allows one to perform calculations on arbitrary mesh resolution that is independent from the Reynolds number. The basic idea behind the scalable wall-function is to limit the y^* value used in logarithmic layer by $y^* = max(y^*, 11.06)$, where 11.06 is the value of y^* at the intersection between the logarithmic and the linear near wall profile.

Low-Reynolds number model

The LRNM resolves the details of the boundary layer region using a very high mesh resolution near the wall. This approach is mainly used for ω-based turbulence models, such as the Wilcox's $k-\omega$ model or the Shear Stress Transport $k-\omega$ model. Appropriate grids for low-Re number modelling should have a y^+ value below 4 or 5 to ensure that the first computational node of the wall-adjacent node is situated in the viscous sub-layer. Preferably, $y^+ \approx 1$ to have at least a few nodes inside the viscous sub-layer.

1.2.3 Multiple Frames of Reference models

Although significant progress has been achieved in the field of CFD over the past few decades, the design and analysis of turbomachineries using numerical simulations still remains a challenging task (Hanimann *et al.*, 2014). Apart from traditional issues such as turbulent modelling or numerical schemes, the CFD for these applications has the additional problem; that is handling the rotating and stationary components. In such applications, the relative motion between the rotor and stator components induces various complex phenomena that need to be captured

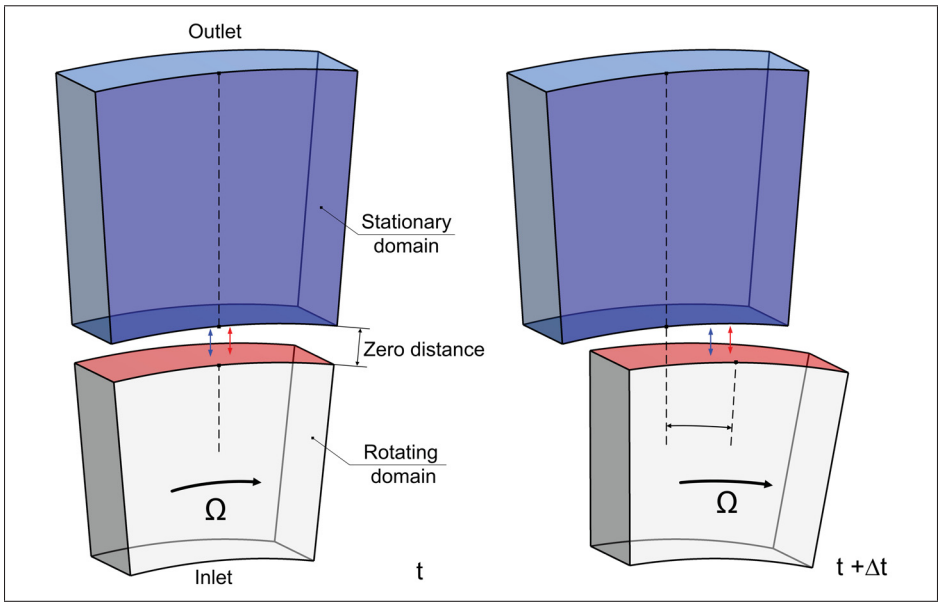

Figure 1.2 Schematic illutration of the transient interface model.

by the numerical model. In the present CFD code, the Multiple Frames of Reference (MFR) approach is used to couple the rotating and stationary domains, where each domain is assigned with the local frame of reference, *i.e.* the fluid near the rotor is solved in a rotating frame of reference and the fluid near the stator is modelled using a stationary frame of reference. Different approaches can be used to deal with the pitch and frame change. These include the steady state approach, such as the *mixing plane* or the *frozen rotor* models, and the unsteady approach, the *transient interface* model.

Transient interface model

Due to the aerodynamic interaction between the moving rotor relatively to the stator, the fluid flow in the rotor-stator system is always unsteady. The most accurate but also the most computationally expensive MFR approach to couple these components is the transient interface model. In the transient interface simulations, the rotating and stationary domains are moved with respect to each other while the flow variables are conservatively transferred between two sides of the interface, whereby the flow field variation in both time and space is fully taken into account. Although the transient interface simulations are intuitive and accurate, they represent a large increase in computational cost compared to the steady analysis, and therefore they are

impractical in many cases.

Mixing plane model

Another successful method to directly couple rotating and stationary components together is the mixing plane model, which has been intensively used as a workhorse for steady state rotor-stator interaction in the turbomachinery industry (Stein *et al.*, 2015). This method gives accurate performance predictions for a wide range of machine types over a wide range of operating conditions and with a great computational efficiency.

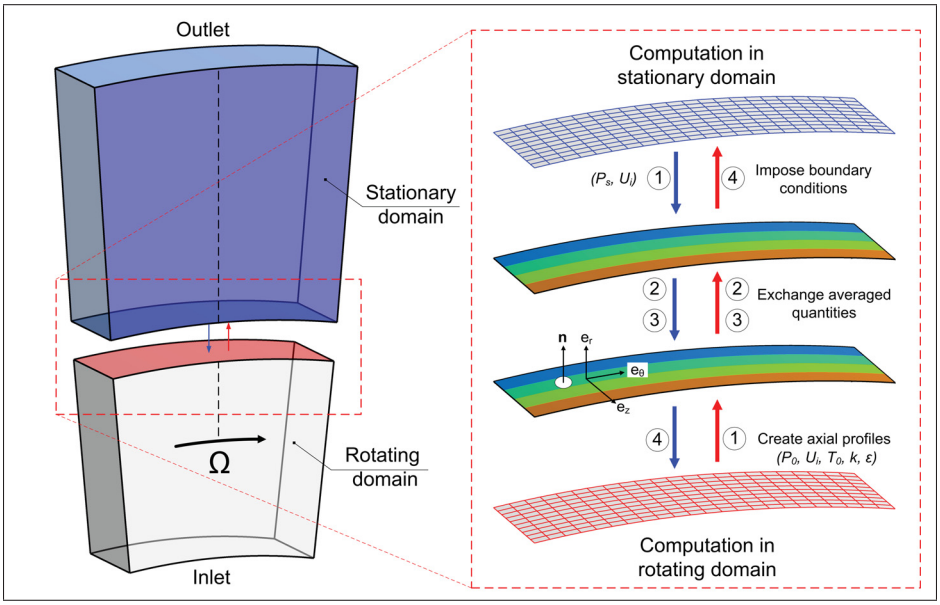

Figure 1.3 Schematic illustration of the mixing plane model.

In this model, the conserved flow variables are first averaged at the outlet of the rotating domain then used to specify as inlet boundary condition for the stationary domain to compute the flow field, and vice versa. This process of exchanging the averaged flow variables between two sides of the interface forms an iterative procedure, as illustrated in Figure 1.3, and is forced to stop when the balance is established at the interface. In the current CFD code, the interface fluxes across the mixing plane are implemented within the solver such that they are fully implicit, and strict conservation is maintained across the interface for the fluxes of mass, linear momentum, total energy and related turbulent quantities. Details on numerical treatment and implementation of the mixing plane interface can be found in Stein *et al.* (2015) and ANSYS

(2015).

Frozen rotor model

The frozen rotor model employs the simplest technique to approximate the rotor-stator unsteady flow using a steady state solution by keeping the position of the rotor fixed relatively to the stator as shown in Figure 1.4. The flow governing equations are solved for each domain in its local frame of reference and the primitive variables are directly transferred across the interface while taking into account the change of frame reference. Therefore, any circumferential flow distribution change due to the variation of the relative position between the two components is not taken into account in this model.

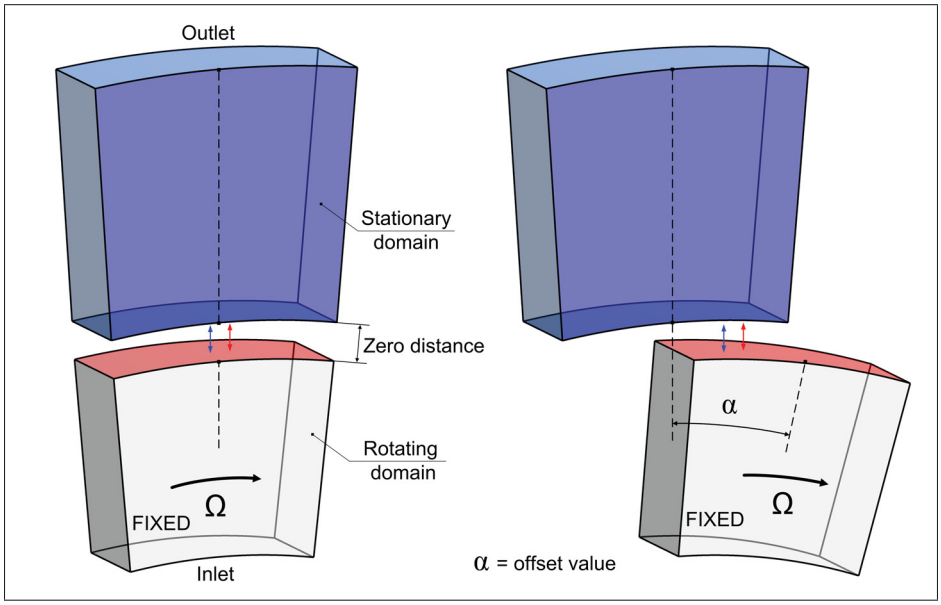

Figure 1.4 Schematic illustration of the frozen rotor model, where α is the offset value.

The frozen rotor analysis is useful when the circumferential flow variation that each passage experiences during a full revolution is large at the rotor-stator interface. Several studies (Hanimann *et al.*, 2014; Stein *et al.*, 2015; Liu & Hill, 2000) showed that solutions obtained with this interface are strongly dependent on the relative position of the rotor to the stator.

1.3 Discretization of governing equations

The CFD code ANSYS-CFX employs the control-volume based finite element method (CVFEM) to discretize the governing equations. The CVFEM was formulated by combining and extending concepts that are native to the finite volume method (FVM) and the finite element method (FEM) (Raithby & Schneider, 1979; Patankar, 1980; Baliga & Patankar, 1980; Schneider & Raw, 1986).

Domain discretization

First, the two-dimensional domain is discretized into four-node quadrilateral elements, the edges and vertices of such elements are also shown in Figure 1.5. The centroid of each element is then joined to the midpoints of its edges to form a *control-volume* around point P using dashed lines in Figure 1.5. In the *co-located* CVFEM, all primitive variables (velocity components, pressure, temperature) are computed and stored at the nodes.

To illustrate the CVFEM discretization procedure, consider the transport equation in a general form of scalar ϕ:

$$\underbrace{\frac{\partial}{\partial t}(\rho\phi)}_{unsteady\ term} + \underbrace{\frac{\partial}{\partial x_j}(\rho U_j \phi)}_{convective\ term} = \underbrace{\frac{\partial}{\partial x_j}\left(\Gamma_{eff}\frac{\partial \phi}{\partial x_j}\right)}_{diffusive\ term} + \underbrace{S_\phi}_{source\ term} \tag{1.17}$$

This equation is then integrated over each control volume (the shaded area in Figure 1.5), and Gauss divergence theorem is applied to convert the volume integral to the surface integral.

$$\frac{d}{dt}\int_V \rho\phi dV + \int_S \rho U_j \phi n_j dS = \int_S \Gamma_{eff}\frac{\partial \phi}{\partial x_j} n_j dS + \int_V S_\phi dV \tag{1.18}$$

where V and S denote the control volume and control surface regions of integration, n_j are components of the outward normal surface vector.

Surface integrals are discretized at the integration points (*ip*) located at the center of each edge

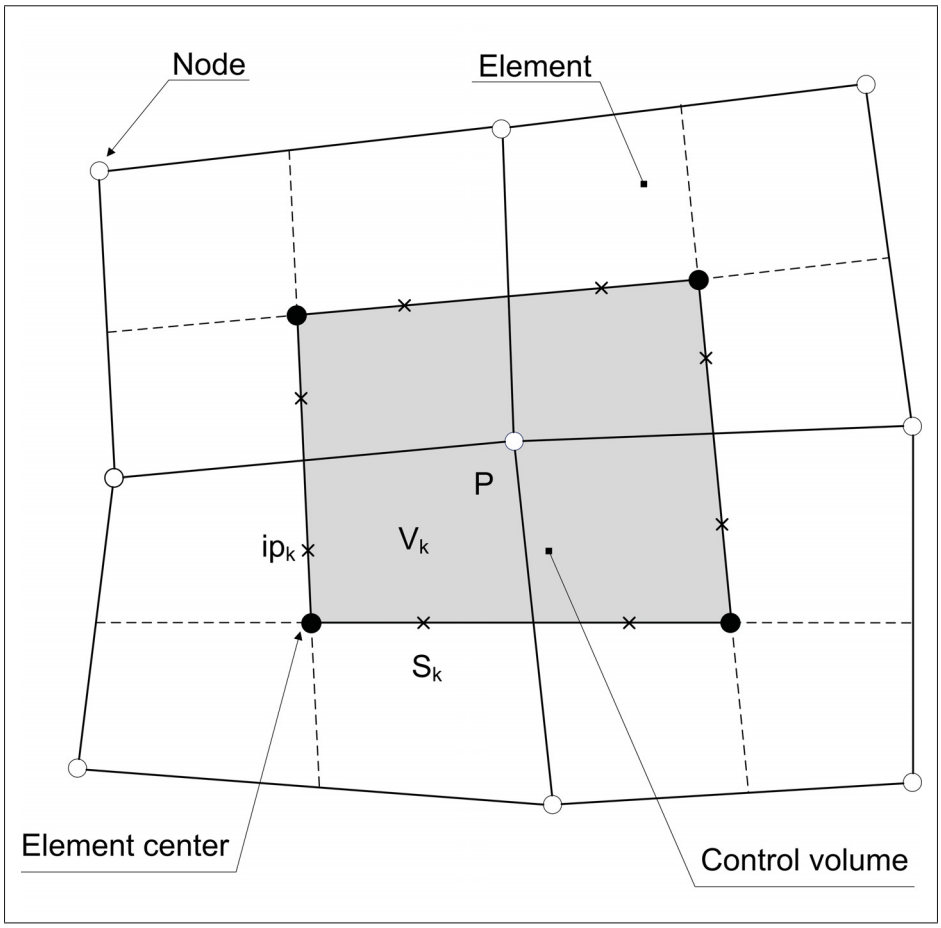

Figure 1.5 Control volume, node, element, and element center definition, where ip_k denotes the integration point, S_k is the length of edge.

as shown in Figure 1.5:

$$V\left(\frac{\rho\phi-\rho^{\circ}\phi^{\circ}}{\Delta t}\right)+\underbrace{\sum_{ip}\dot{m}_{ip}\phi_{ip}}_{convective\ term}=\underbrace{\sum_{ip}\left(\Gamma_{eff}\frac{\partial\phi}{\partial x_j}n_j\right)_{ip}\Delta S}_{diffusive\ term}+\overline{S_{\phi}}V \tag{1.19}$$

where $\dot{m}=\rho U_j n_j \Delta S$ is the mass flow rate through sub control surface ΔS, Δt - the time step, subscript $^{\circ}$ refers to the old time level value.

Diffusive term

The finite element shape functions N_i are used to interpolate variable ϕ anywhere within an

element from the nodal value ϕ_i as follows:

$$\phi = \phi(s,t,u) = \sum_{i=1}^{N_{nodes}} N_i(s,t,u)\phi_i \tag{1.20}$$

where N_i is the shape function of node i, ϕ_i is the value of ϕ at node i, N_{nodes} is the number of nodes in the considered element, and s,t,u are parametric coordinates.

The derivative in the x direction at integration point ip is:

$$\left.\frac{\partial \phi}{\partial x}\right|_{ip} = \sum_{i=1}^{N_{nodes}} \left.\frac{\partial N_i}{\partial x}\right|_{ip} \phi_i \tag{1.21}$$

$$\begin{pmatrix} \frac{\partial N_i}{\partial x} \\ \frac{\partial N_i}{\partial y} \\ \frac{\partial N_i}{\partial z} \end{pmatrix} = \begin{bmatrix} \frac{\partial x}{\partial s} & \frac{\partial y}{\partial s} & \frac{\partial z}{\partial s} \\ \frac{\partial x}{\partial t} & \frac{\partial y}{\partial t} & \frac{\partial z}{\partial t} \\ \frac{\partial x}{\partial u} & \frac{\partial y}{\partial u} & \frac{\partial z}{\partial u} \end{bmatrix}^{-1} \cdot \begin{pmatrix} \frac{\partial N_i}{\partial s} \\ \frac{\partial N_i}{\partial t} \\ \frac{\partial N_i}{\partial u} \end{pmatrix} = [J]^{-1} \cdot \begin{pmatrix} \frac{\partial N_i}{\partial s} \\ \frac{\partial N_i}{\partial t} \\ \frac{\partial N_i}{\partial u} \end{pmatrix} \tag{1.22}$$

where J is the Jacobian matrix.

The outward normal, $\mathbf{n} \cdot \Delta S$ can be expressed in the form:

$$\mathbf{n} \cdot \Delta S = \Delta S_x \cdot \mathbf{i} + \Delta S_y \cdot \mathbf{j} + \Delta S_z \cdot \mathbf{k} \tag{1.23}$$

where **i**, **j**, and **k** are unit vector in x, y, and z direction, respectively.

Substitute the equations 1.21, 1.22, and 1.23 into the diffusive term in Equation 1.19. The latter can be rewritten as:

$$\left(Q_\phi^d\right)_{ip} = \sum_{i=1}^{N_{nodes}} \Gamma_{eff} \begin{bmatrix} \Delta S_x & \Delta S_y & \Delta S_z \end{bmatrix} \cdot [J]_{ip}^{-1} \cdot \begin{pmatrix} \frac{\partial N_i}{\partial s} \\ \frac{\partial N_i}{\partial t} \\ \frac{\partial N_i}{\partial u} \end{pmatrix}_{ip} \cdot \phi_i \tag{1.24}$$

It means that for each integration point ip_k, the diffusive flux can be represented as a linear combination of ϕ nodal values:

$$\left(Q_\phi^d\right)_{ip_k} = \sum_{i=1}^{N_{nodes}} DD_{ki}^{\phi} \cdot \phi_i \tag{1.25}$$

where the coefficient is defined as:

$$DD_{ki}^{\phi} = \Gamma_{eff} \begin{bmatrix} \Delta S_x & \Delta S_y & \Delta S_z \end{bmatrix} \cdot [J]_{ip}^{-1} \cdot \begin{pmatrix} \frac{\partial N_i}{\partial s} \\ \frac{\partial N_i}{\partial t} \\ \frac{\partial N_i}{\partial u} \end{pmatrix}_{ip} \tag{1.26}$$

Convective term

To evaluate the convective term, $\dot{m}_{ip}\phi_{ip}$, in Equation 1.19, one need to approximate the ϕ_{ip} at the integration point in terms of neighbouring vertex values:

$$\phi_{ip} = \phi_{up} + \beta \nabla\phi \cdot (\mathbf{x}_{ip} - \mathbf{x}_{up}) \tag{1.27}$$

where ϕ_{up} is the value at the upwind node, and β is an adjustable parameter, the choice of β and $\nabla\phi$ yields different schemes as follows.

First order Upwind Differencing Scheme

For the case $\beta = 0$, the convective term in Equation 1.27 yields a first-order upwind differencing scheme (UDS).

$$\phi_{ip} = \phi_{up} \tag{1.28}$$

The approximation of skewed upwind value corresponding to ip_1 starts with the evaluation of the mass flow rate through sub-surface-control with integration points ip_1, ip_2, and ip_4:

$$\begin{aligned} \dot{m}_1 &= \int_{S_1} \rho \mathbf{U} \cdot \mathbf{n} dS_1 \\ \dot{m}_2 &= \int_{S_2} \rho \mathbf{U} \cdot \mathbf{n} dS_2 \\ \dot{m}_4 &= \int_{S_4} \rho \mathbf{U} \cdot \mathbf{n} dS_4 \end{aligned} \tag{1.29}$$

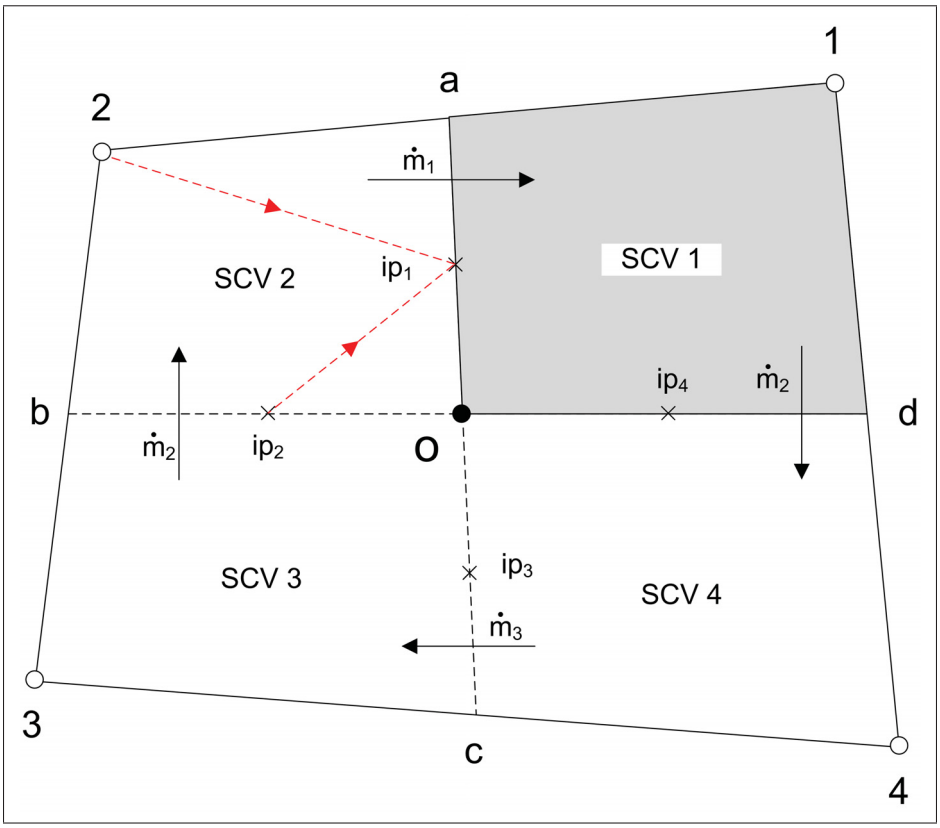

Figure 1.6 Single element with sub control volume.

$$\phi_{up} = \begin{cases} (1-f)\phi_2 + f\phi_{ip_2} & \text{where } f = min\left[max\left(\frac{\dot{m}_2}{\dot{m}_1}, 0\right), 1\right] \text{ if } \dot{m}_1 > 0 \\ (1-f)\phi_1 + f\phi_{ip_4} & \text{where } f = min\left[max\left(\frac{\dot{m}_4}{\dot{m}_1}, 0\right), 1\right] \text{ if } \dot{m}_1 < 0 \end{cases} \tag{1.30}$$

Similar expressions in the same form as Equation 1.30 can be obtained for ϕ at other integration points ϕ_{ip2}, ϕ_{ip3}, and ϕ_{ip4}. Rewrite these equations in the matrix form.

$$\left(\phi^{ip}\right) = \left[C^{ip}\right] \cdot \left(\phi^{ip}\right) + \left[C^{N}\right] \cdot \left(\phi^{N}\right) \tag{1.31}$$

where $\left(\phi^{ip}\right) = \begin{bmatrix} \phi_{ip_1} & \phi_{ip_2} & \phi_{ip_3} & \phi_{ip_4} \end{bmatrix}^T$ is the column of ϕ at integration points and $\left(\phi^{N}\right) = \begin{bmatrix} \phi_1 & \phi_2 & \phi_3 & \phi_4 \end{bmatrix}^T$ is the column of ϕ at computational nodes. Therefore, the local matrix of

the mass weighted upwind scheme can be found as

$$\left(\phi^{ip}\right) = \left[I - C^{ip}\right]^{-1} \cdot \left[C^{N}\right] \cdot \left(\phi^{N}\right) = \left[CC^{\phi}\right] \left(\phi^{N}\right) \tag{1.32}$$

where I is the unit matrix. This expression indicates that for each integration point ip_k, the convective flux can be expressed as a linear combination of ϕ nodal values:

$$\left(Q_{\phi}^{c}\right)_{ip_k} = \dot{m}_{ip_k} \cdot \phi_{ip_k} = \sum_{i=1}^{4} CC_{ki}^{\phi} \phi_i \tag{1.33}$$

The first order upwind is a robust and unconditionally bounded scheme, however it introduces artificial error that has problems with steep spatial gradients. This can be seen by examining the Taylor expansion at the upwind location $\mathbf{x}_{up}$:

$$\phi(\mathbf{x}) = \phi_{up} + (\mathbf{x} - \mathbf{x}_{up}) \cdot (\nabla\phi)_{up} + \sum_{k=2}^{\infty} \frac{1}{k!} (\mathbf{x} - \mathbf{x}_{up})^{k} \underbrace{:: .. ::}_{k-1 \; times} \left(\underbrace{\nabla\nabla ... \nabla\phi}_{k \; times} \right)_{up} \tag{1.34}$$

The truncation error for the approximation of the convective term $\dot{m}_{ip}\phi_{ip}$ can be expressed as:

$$\underbrace{\dot{m}_{ip} \cdot (\mathbf{x}_{ip} - \mathbf{x}_{up})}_{\alpha_{num}} \cdot (\nabla\phi)_{up} \tag{1.35}$$

This truncation error is also called the *false diffusion* since the neglected part can be interpreted as a diffusive flux. For the case of high gradients in the flow direction, the approximation can be quite inaccurate for the large mass flow rate. It can be necessary to employ a very fine mesh, i.e. small $\mathbf{x}_{ip} - \mathbf{x}_{up}$, in order to increase the accuracy of computation.

Specified blend factor

By choosing the blend factor β such that $0 < \beta < 1$, and $\nabla\phi$ equal to the average of the adjacent nodal gradients, the truncation errors associated with UDS are reduced. The term $\beta\nabla\phi \cdot \Delta\vec{r}$ is called the *numerical advection correction*.

For the case $\beta = 1$, the scheme is formally second-order accurate scheme in space, however, it is unbounded and may introduce *dispersive discretization errors* (ANSYS, 2015).

Transient terms

The first-order backward Euler scheme

$$\frac{\partial}{\partial t}\int_V \rho\phi dV \approx V\cdot\frac{(\rho\phi)-(\rho\phi)^0}{\Delta t} \tag{1.36}$$

This scheme is robust, fully implicit, bounded, conservative in time, and does not have a time step size limitation, however, only first-order accurate in time.

The second-order backward Euler scheme

$$\frac{\partial}{\partial t}\int_V \rho\phi dV \approx V\cdot\frac{3(\rho\phi)-4(\rho\phi)^0+(\rho\phi)^{00}}{2\Delta t} \tag{1.37}$$

This scheme is also robust, implicit, conservative in time, and does not have time step size limitations. It is a second-order accurate in time, but is not bounded and may create some non-physical solution oscillations.

The above procedure have demonstrated a method to discretize a generic transport equation

$$V\left(\frac{\rho\phi-\rho^\circ\phi^\circ}{\Delta t}\right)+\sum_{ip}\dot{m}_{ip}\phi_{ip}=\sum_{ip}\left(\Gamma_{eff}\frac{\partial\phi}{\partial x_j}n_j\right)_{ip}\Delta S+\overline{S_\phi}V \tag{1.38}$$

to the linear algebraic form for each internal node P

$$\left(a_P^\phi+\frac{\rho V_P}{\Delta t}\right)\phi_P=\sum_{nb}a_{nb}^\phi\phi_{nb}+b_P^\phi+\left(\frac{\rho V_P}{\Delta t}\right)\phi_P^\circ \tag{1.39}$$

CHAPTER 2

LITERATURE REVIEW

In this chapter, a review of literature relevant to the thermal analysis of large hydro generators is presented. According to Boglietti *et al.* (2009), three common approaches are frequently used to perform thermal analysis in electrical machines: lumped-parameter thermal network (LPTN), finite element analysis (FEA), and computational fluid dynamics (CFD).

2.1 Lumped-parameter thermal network and finite element analysis

The lumped-parameter thermal network is regarded as the thermal counterpart of the electrical circuit that is widely used in electrical engineering. The equivalences between these types of networks are the temperature to the voltage, the heat flux to the current, and the thermal resistance to the electrical resistance. The LPTN attempts to represent the circuit of heat transferred in the machine by lumping together components that have the same temperatures, which is defined as a single node in the network. This approach has been extensively employed and validated on many machine types and operating regimes. The main advantages of the LPTN method is that this approach provides an efficient, fast-to-solve tool for the thermal analysis of electrical machines, which is able to analyze the whole machine as a single system. However, the LPTN only provides the average temperature values of the solid components, and therefore it may only reliably assess some fundamental design concepts at the preliminary stages.

Owing to a strong mathematical formulation, the finite element analysis is currently an effective tool for the thermal analysis, especially the heat conduction analysis. However, FEA has the same drawback as the LPTN approach, which also requires the convective heat transfer coefficients (CHTC) at the convective boundary before performing the calculation. The CHTC were traditionally evaluated by widely-used empirical correlations that were established in heat transfer textbooks. Since the empirical correlations are derived for simple configurations and certain flow regimes, they may not be sufficiently accurate for cases involving complex geometry. In addition, since these correlations evaluate an average CHTC value for a whole surface,

the spatial distribution is not taken into account. In the scope of this thesis, the literature review on the LPTN analysis and FEA studies for the hydro-generator will not be covered.

2.2 Computational Fluid Dynamics applications

The field of computational fluid dynamics (CFD) has progressed enormously over the past few decades with the advent of computing power and the development of numerical methods for fluid dynamics. The main advantage of the CFD approach compared to the traditional methods is that the numerical simulations provide detailed structures of the thermal boundary layer, which is essentially important for the analysis of convective heat transfer phenomenon. CFD simulations have been intensively used in design and optimization of turbomachinery applications, *e.g.* centrifugal pumps, compressors, turbochargers, etc.. However, they were less used for analyzing rotating electrical machines. An analysis of the convective cooling requires an accurate description of the flow field. However, there are very few available studies on the flow of cooling air in electric generators (Moradnia *et al.*, 2014a). Apart from traditional aspects such as the turbulence modeling or the numerical scheme, the CFD for these applications has the additional challenge of handling the rotating and stationary components. Indeed, the relative motion between these components induces an unsteady rotor-stator flow interaction that requires an ad-hoc numerical treatment. In Table 2.1, the published studies that used the CFD approach for the hydro-generator are summarized. The publications are classified based on the multiple frames of reference, turbulence models, the boundary layer modelling, the fluid-solid interface treatment, and the cooling scheme of the ventilation circuit that were used. Abbreviations used in this table include MFR (Multiple Frames of Reference), Turb. (turbulence model), BLM (boundary layer modelling), FSI (fluid-solid treatment), Cool.sch. (cooling scheme), FR (frozen rotor), MP (mixing plane), TR (transient interface), SKE (the standard $k-\varepsilon$), WF (wall functions), EWF (enhanced wall-functions), ATW (Automatic Wall Treatment), OF (OpenFOAM), SST (Shear Stress Transport), CHT (conjugate heat transfer), na (not available). Shanel *et al.* (2000); Pickering *et al.* (2001, 2002) are considered to be the pioneers who first applied CFD to analyze the ventilation flow in the large hydro-generator.

Author	Solver	MFR	Turb.	BLM	CHT	Cool.sch.
Shanel *et al.* (2000)	FLUENT	FR	SKE	WF	na	axial
Pickering *et al.* (2001)	FLUENT	FR	SKE	WF	na	axial
Pickering *et al.* (2002)	FLUENT	FR	SKE	WF	na	axial
Toussaint *et al.* (2011)	CFX	FR/MP	SKE	WF	na	radial
Hettegger *et al.* (2012)	CFX	TR	SST/SAS	ATW	na	na
Connor *et al.* (2013)	FLUENT	FR	SKE	EWF	na	radial
Schrittwieser *et al.* (2014)	CFX	FR/MP	SST	ATW	na	axial
Moradnia *et al.* (2014a)	OF	FR	RKE	EWF	na	axial
Moradnia *et al.* (2014b)	OF	FR	RKE	EWF	na	axial
Jamshidi *et al.* (2015)	OF	FR/MP	RKE	EWF	na	axial
Hosain *et al.* (2017)	FLUENT	TR	RKE	EWF	na	na
Shanel *et al.* (2003)	FLUENT	FR	SKE	WF	Yes	axial
Weili *et al.* (2013)	FLUENT	FR	SKE	WF	Yes	radial
Klomberg *et al.* (2015a)	CFX	MP	SST	ATW	Yes	axial
Klomberg *et al.* (2015b)	CFX	MP	SST	ATW	Yes	axial
Lancial *et al.* (2017)	CFX	TR	SST	ATW	Yes	axial

Table 2.1 Summary of CFD studies on the flow and thermal analysis of hydro-generators.

The numerical simulations and experimental measurements were performed on a scale rotating model representing a 1 MVA synchronous 4-pole generator. The MFR frozen rotor model was used to couple the rotor and stator. For the turbulence modelling, the standard $k-\varepsilon$ model with the standard wall functions was employed due to its excellent convergence and stability. A pure convective heat transfer approach was used, for which a uniform wall heat flux of $q_w = 1000W \cdot m^{-2}$ was locally applied on the rotor surface at the same position of heating elements installed on the surface of a rotor pole. Firstly, the results indicated that the numerically predicted heat transfer coefficient on the pole face follows the same trends of those profiles obtained experimentally. However, the measured heat transfer coefficients on the pole face are much higher than those predicted by CFD calculations. This discrepancy between the numerical and experimental data can be attributed to the limitation of the steady state frozen rotor model. It was stated in Shanel *et al.* (2000) that the frozen rotor model generally underpredicts CHTC in the location of high shear and strong flow interaction between rotor and stator. To improve the accuracy of the CHTC prediction on the pole face, the more realistic unsteady sliding

interface model would be desirable, however, it is much more demanding, typically increasing the computational cost by ten times to reach the stabilized solution. Regarding the flow field prediction, it was demonstrated that the commercial code accurately computed the tendency of flow distribution through radial stator ducts in the downstream direction. It was shown that the commercial CFD package `FLUENT` presented an efficient tool to predict the air flow and heat transfer on the rotor of the salient pole generator.

Toussaint *et al.* (2011) presented an analysis of the flow field in the two- and three-dimensional configurations of a scale rotating model using `ANSYS CFX`. In particular, the effects of rotor-stator interface (RSI) location on the flow prediction were investigated to determine the optimal parameters for this application. The results computed on the two-dimensional configuration, illustrated in Figure 2.1, showed that the steady state MFR solution is highly sensitive to the type and location of the rotor-stator interface. The flow fields calculated by the frozen rotor model vary significantly depending on the relative position between the rotor and the stator. On the contrary, the steady state mixing plane model provided the results that matched with the time-averaged transient reference values in terms of the radial velocity profile at the stator ducts. The numerical results computed on the three-dimensional configuration demonstrated that there is a maximum variation of 20% in both the total ventilation flow rate and total windage loss between the examined rotor-stator interface locations. Nevertheless, the relative flow distribution normalized by the total flow rate was not influenced by the RSI location. It should be noted that this primary analysis was carried out based on a pure numerical setting, which must be validated by experimental data before any conclusions can be made.

Hettegger *et al.* (2012) presented a study that combined the numerical and experimental approaches to characterize the heat transfer coefficients on the end windings of a hydro-generator schematically depicted in Figure 2.2. Due to the numerical instability of the steady state calculations, unsteady simulations were performed using the shear stress transport (SST) $k-\omega$ and the scale-adaptive simulation (SAS) turbulence models. The results showed that the heat transfer coefficient predicted by CFD underestimated the measured values. It was also concluded that CFD is very useful for the calculation of the heat transfer distribution at the stator surface. However, the numerical results could not be validated due to the lack of experimental data.

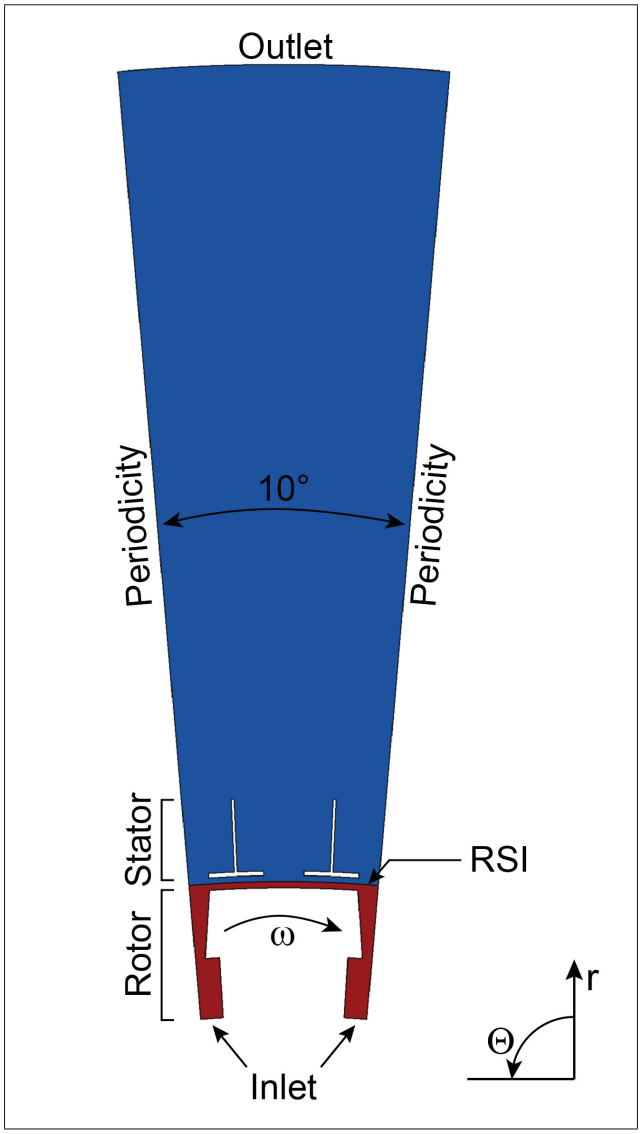

Figure 2.1 Domain and boundary conditions for two-dimensional simulations in Toussaint *et al.* (2011)

Connor *et al.* (2013) focused on the flow and thermal analysis of a hydro-generator prototype with the aim of quantifying the windage losses in the machine. The numerical simulations were performed on a full 360°model of the generator due to the lack of symmetric features in the machine's geometry. The MFR frozen rotor model was employed for the rotor-stator coupling. The standard $k-\varepsilon$ model is used for turbulence modelling since it is more stable and robust for rotating applications. The boundary layer was handled with the `FLUENT` enhanced

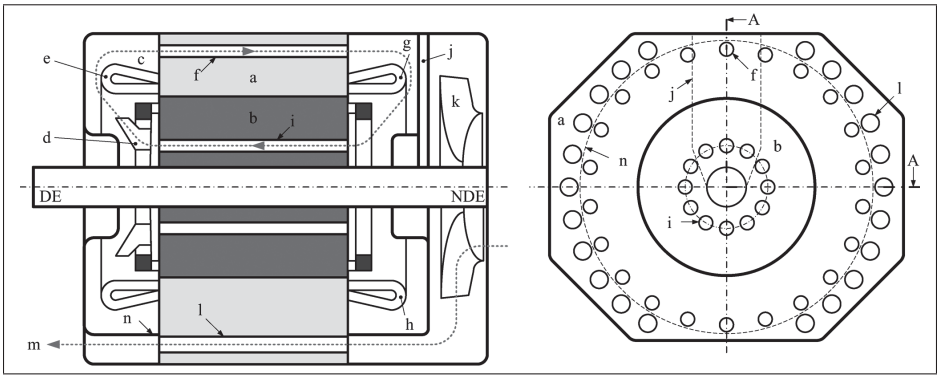

Figure 2.2 Longitudinal section (A-A) and cross section of the investigated DACS motor in Hettegger *et al.* (2012)

wall function approach, where the modelling treatment was automatically assigned based on the near-wall mesh resolution. Validation of the numerical results was obtained through a comparison with the experimental data. It was found that the CFD underpredicted the mass flow rate and windage losses compared to the measured data, by 4% and 7%, respectively.

Schrittwieser *et al.* (2014) presented an analysis of the fluid flow in the stator ducts using CFD simulations to evaluate the performance of a hydro-generator simplified model illustrated in Figure 2.3. It was demonstrated that the relative difference in terms of flow and thermal fields in the stator duct predicted by the mixing plane and the frozen rotor models was less than 10%. The numerical simulations where the mixing plane model was employed required 44% less computational nodes as compared to those computed by the frozen rotor model. Furthermore, the numerical results indicated that the CHTC computed with the $k-\varepsilon$ model is similar to the one provided by the SST model, however, the SST turbulence model with automatic wall treatment was more sensitive to the mesh resolution than the standard $k-\varepsilon$ model.

Moradnia *et al.* (2014a) presented an investigation on the ventilation flow in a half-scale model of an electric generator as shown in Figure 2.4. The PIV measurement at the inlet region and the total pressure rake measurement at the outlet of stator channels were used to experimentally characterize the cooling air flow in the machine. These experimental data were used to validate the numerical simulations performed with the open-source CFD code `OpenFOAM`. The MFR frozen rotor interface model was used at the rotor-stator interface and the turbulence effect was

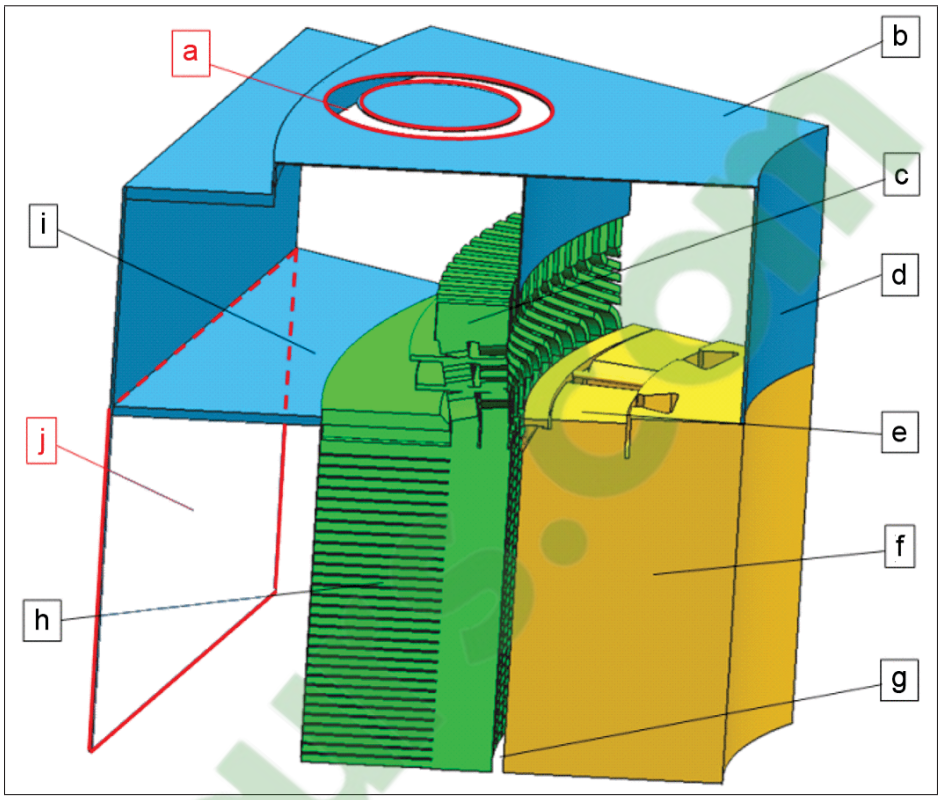

Figure 2.3 Overall pole section model of the investigated hydro-generator showing the (a) inlet, (b) bearing support spider, (c) end winding, (d) shaft, (e) pole with pole winding, (f) rotor, (g) air gap, (h) stator with stator ducts, (i) web plate, and (j) outlet in Schrittwieser *et al.* (2014).

handled by the low-Re Launder-Sharma $k-\varepsilon$ model. Two numerical approaches were considered, as illustrated in Figure 2.4. The first approach was a *fully predictive* model, FP, in which the flow was simulated independently from the experimental results. The second one is the *boundary condition* model, BC, with inlet and outlet boundary conditions obtained from the measured values. It was shown that for both configurations, the flow fields predicted by CFD matched very well with the experimental data. With the fully predictive model, the numerically predicted flow rate differed, by 2 to 7% as compared to the measured values. Moreover, the mesh sensitivity analysis indicated that the FP computations were less sensitive to the mesh resolution than the BC calculations. With respect to the total pressure coefficients at the stator channel outlets, the agreement between the numerical and experimental values for the FP con-

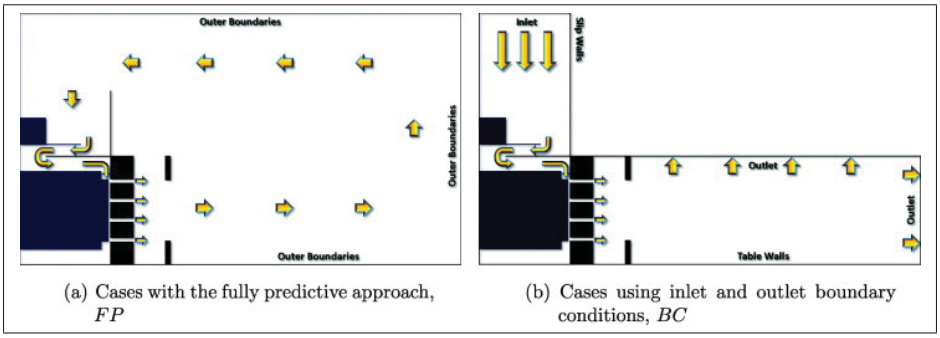

(a) Cases with the fully predictive approach, *FP*

(b) Cases using inlet and outlet boundary conditions, *BC*

Figure 2.4 Geometry of generator used in Moradnia *et al.* (2014a).

figuration was much better than that of the BC model.

Moradnia *et al.* (2014b) presented an assessment of a fully predictive CFD approach for the cooling airflow in an axially cooled electric generator as illustrated in Figure 2.5. In the fully predictive model, the computational domain was extended to a space outside the generator to allow the cooling airflow circulate into and out of the machine. Owing to this setting, the fluid flow prediction is obtained independently from the experimental measurement. A comparison between the numerically predicted flow field and the measured data demonstrated that a very good agreement was obtained. It was also indicated that although the numerically predicted flow rate was lower than the experimental value, the difference was relatively small, given the geometrical complexity of the scale model, numerous uncertainties in both numerical and experimental measurement approaches, and the fact that the numerical and experimental studies were carried out totally independently.

Jamshidi *et al.* (2015) presented a study on the cooling air flow in an electric generator model resembling the one used in the previous works (Moradnia *et al.*, 2014a,b). The modification was made on an existing experimental generator ventilation model, as shown in Figure 2.6 to increase the flow rate and improve the flow distribution in the machine. The numerical results showed that the new fan design doubled the flow rate and provided a more uniformly distributed flow in comparison to the case without the fan blades. Furthermore, it was demonstrated that the frozen rotor and mixing plane models produced similar flow fields for the considered configuration. Finally, the numerically predicted results showed a very good agreement with the

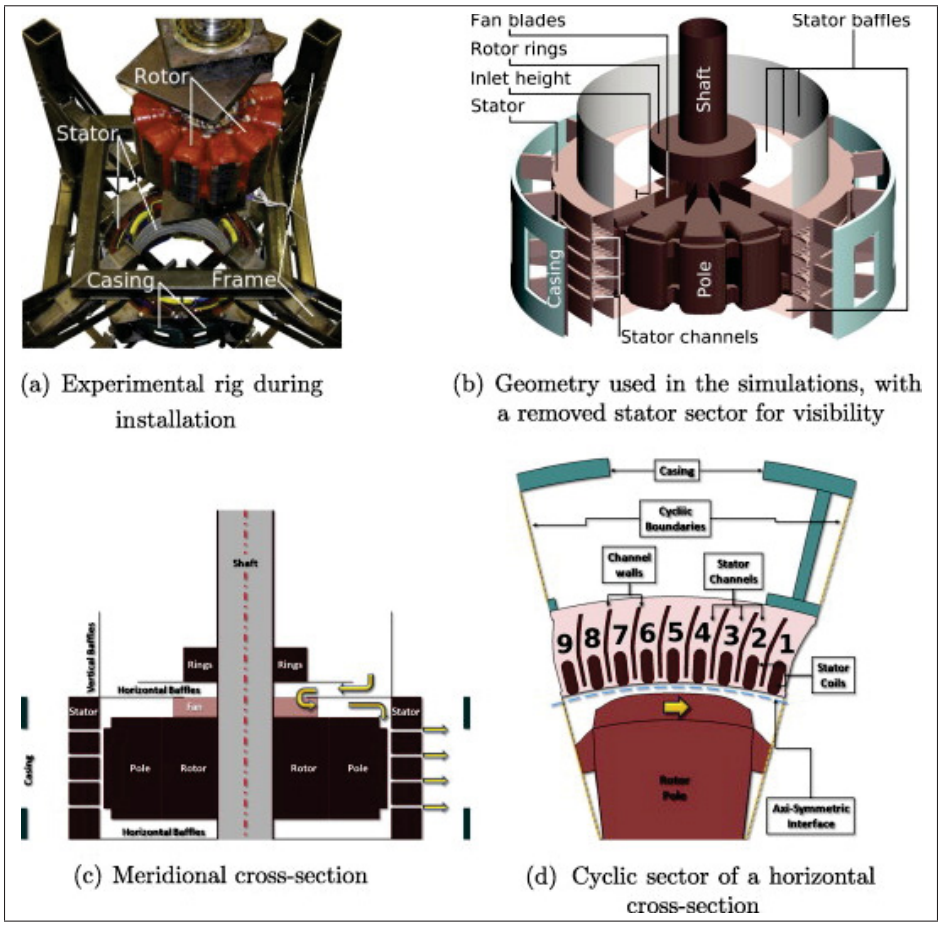

(a) Experimental rig during installation

(b) Geometry used in the simulations, with a removed stator sector for visibility

(c) Meridional cross-section

(d) Cyclic sector of a horizontal cross-section

Figure 2.5 Geometry of generator used in Moradnia *et al.* (2014b).

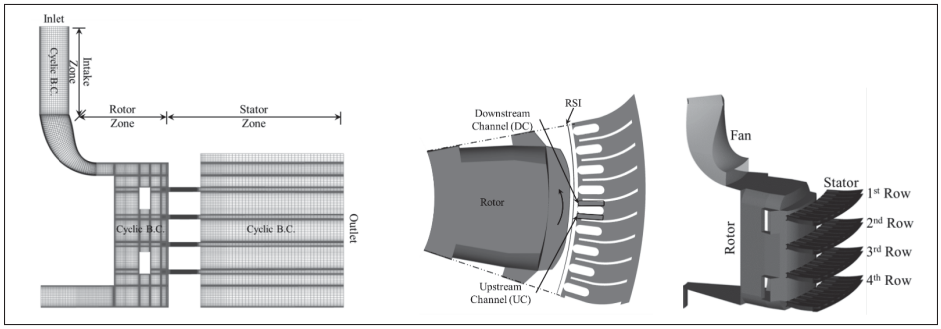

Figure 2.6 Computational domain and MFR zones in Jamshidi *et al.* (2015)

experimental data at all monitoring locations.

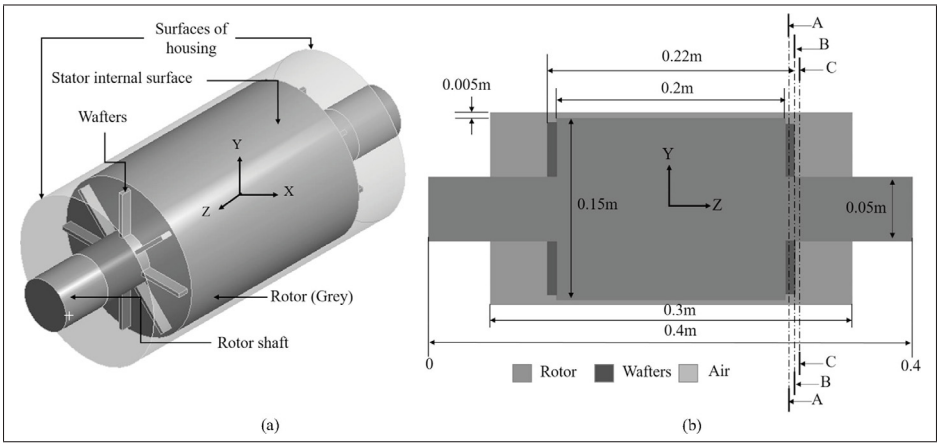

Figure 2.7 Computational domain (a) simplified motor geometry in 3D (b) YZ cross section plane at X = 0 of the numerical domain in Hosain *et al.* (2017).

Hosain *et al.* (2017) investigated the flow field in a rotor-stator air gap using the realizable $k-\varepsilon$ model in combination with the transient sliding mesh interface for the rotor-stator coupling. The numerical results, performed on the computational domain depicted in Figure 2.7, were validated by comparing with the available experimental data, and a very good agreement was obtained.

In the majority of the numerical thermal studies in the literature, the pseudoconvective heat transfer approach was actively used (Coletti *et al.*, 2012). In this approach, a uniform heat flux (Neuman boundary condition) or a uniform temperature (Dirichlet boundary condition) was applied on the fluid-solid interface to solve the thermo-fluid problem in the fluid domain. Since the convective heat transfer coefficient is traditionally considered as an invariant parameter of the convection with respect to the thermal boundary condition (Moffat, 1998), the CHTC is then extracted to prescribe as the boundary condition to solve the solid heat conduction equation. This pure convective approach is equivalent to the procedure intensively employed in industrial applications where the heat transfer coefficients is considered to be *invariant* with respect to the thermal boundary condition and correlations/simulations developed in pure convective are applied (Moffat, 1998; Iaccarino *et al.*, 2002; Coletti *et al.*, 2012; Cukurel & Arts,

2013; Li *et al.*, 2016). This approach, however, neglects the effect of heat conduction, which might lead to an inaccurate prediction of the CHTC. In the conjugate heat transfer (CHT) approach, the fluid dynamics governing equations are simultaneously solved in a coupled manner with the heat conduction equation in a single module, which provides a better representation of the convection phenomenon. Due to a relatively high computational cost associated with the CHT method, this approach was only employed in recent studies for the thermal analysis of hydro-generators. Shanel *et al.* (2003) presented a study that combined conduction-convection heat transfer to predict the temperature distribution on the rotor surface of an air-cooled, 4-pole generator using the CFD code FLUENT. The airflow features of this machine had been investigated in previously published (Shanel *et al.*, 2000; Pickering *et al.*, 2001, 2002). The simulations were performed using the standard $k-\varepsilon$ turbulence model with the wall-functions approach for boundary layer modelling. The MFR frozen rotor was employed to handle the rotor-stator interaction. The numerical results show that the modelling of the winding bars as homogeneous materials with anisotropic thermal conductivity provided sufficient accuracy for the prediction of the coil temperature. Based on the CFD analysis, a modification was made on the experimental model to enhance the heat transfer coefficient. It was shown that CFD analysis can be used effectively to predict temperature field in electrical machines by simultaneously solving conduction heat transfer with the conjugate heat transfer methodology.

Weili *et al.* (2013) performed the conjugate heat transfer calculation to analyze the turbulent flow and heat transfer characteristics in a large 250 MW hydro-generator using ANSYS FLUENT. The simplified model of the actual physical geometry is shown in Figure 2.8. The frozen rotor model was used to couple the rotor and stator, and the $k-\varepsilon$ model with the wall functions approach was employed to handle the effect of turbulence. It was demonstrated that the CHT method could accurately predict the flow and thermal field, which provides a foundation for the design and improvement of the hydro-generator ventilation cooling system. The numerically calculated temperature of the excitation winding showed a very good agreement with the measured value since the error was less than 1%.

Klomberg *et al.* (2015b) performed a CFD analysis of the flow and heat transfer at the end winding region of a hydro-generator, which served to develop correlations between the wall

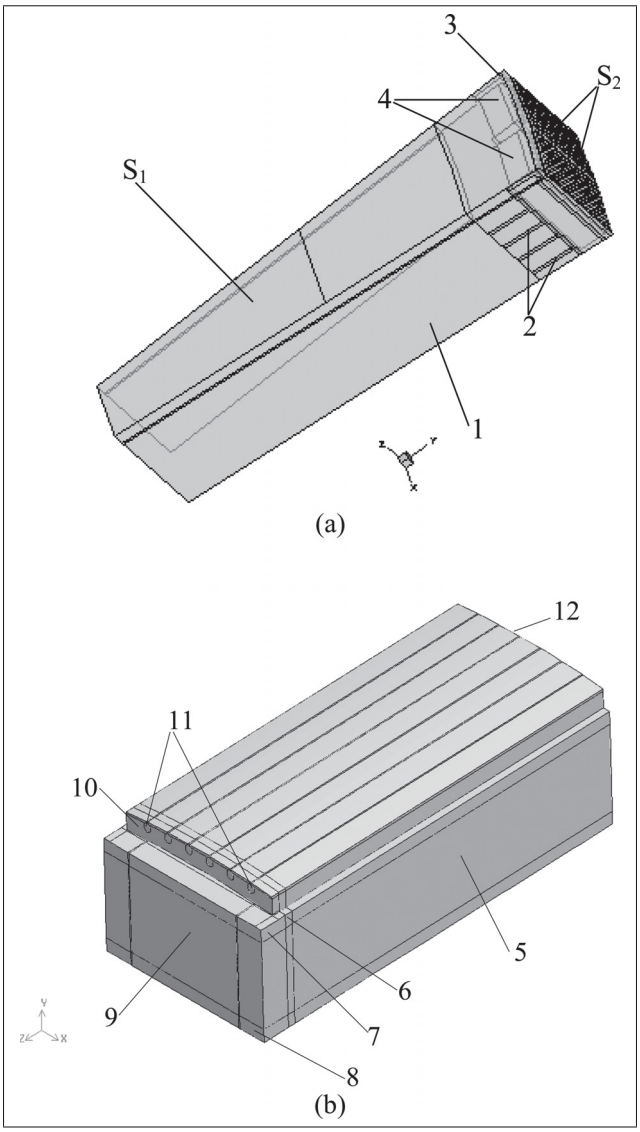

Figure 2.8 Calculation area model of a 3-D coupling field of the rotor in Weili *et al.* (2013).

convective heat transfer and speed, and air flow rate parameters. The steady state simulations with the mixing plane interface model were performed to investigate the influence of the numerical settings on the established correlations. The mesh sensitivity study has confirmed that the requirement on the dimensionless wall distance, $y^+ \approx 1$, is desirable to increase the accuracy of computations, but not obligatory. Also, it was indicated that the rotational speed has no impact on the wall convective heat transfer distribution on the end winding bars of the hydro-

generator.

Klomberg *et al.* (2015a) presented a study that focused on developing new analytical correlations for the calculation of the heat transfer coefficient at the hydro-generator end winding bars corresponding to three different ventilation schemes illustrated in Figure 2.9. The accuracy of these correlations was validated by a comparison with the CFD-based results and a good agreement was found. Further, a comparison between results computed by the conjugate heat transfer and heat conduction showed a very good agreement. The analytical convective heat transfer models were then used in the lumped-parameter thermal model for the design procedure.

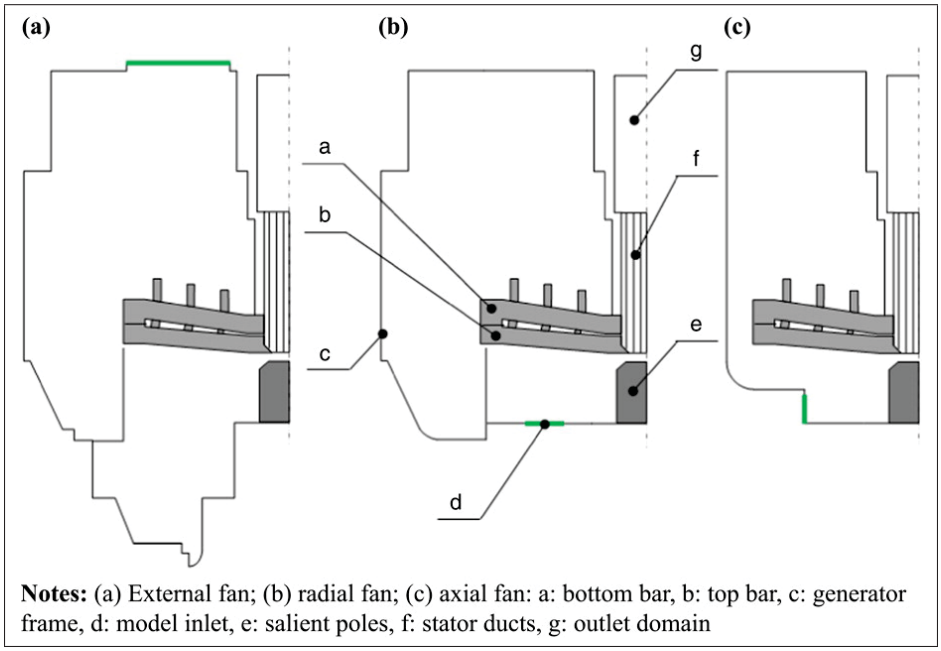

Notes: (a) External fan; (b) radial fan; (c) axial fan: a: bottom bar, b: top bar, c: generator frame, d: model inlet, e: salient poles, f: stator ducts, g: outlet domain

Figure 2.9 Investigated ventilation schemes in Klomberg *et al.* (2015a).

Lancial *et al.* (2017) investigated a Taylor-Couette-Poiseuille flow in an annular channel of a slotted rotating inner cylinder, which is typically found in a salient pole hydro-generator. The CAD geometry and mesh used in that study are illustrated in Figure 2.10. The Shear Stress Transport $k-\omega$ turbulence model with a very fine mesh near the wall, $y^+ \approx 1$, was employed. The temperature distribution on the rotor pole face was experimentally obtained and

then compared with the numerical values calculated with `ANSYS CFX` and `Code Saturne 3.0` coupled with `SYRTHES 4.0`. A very good agreement was found. Afterwards, a parametric analysis was also carried out to study the main flow regimes in the air gap, based on which the correlations in terms of the dimensionless convective coefficient on the rotor pole face were derived. The results showed that the Nusselt number on the pole face and inductive faces trailing side is proportional to $Re^{1/7}$, where Re is the Reynolds number based on rotor tip tangential velocity. This correlation is found to be similar to the one established in the classical flows between two concentric and smooth cylinders.

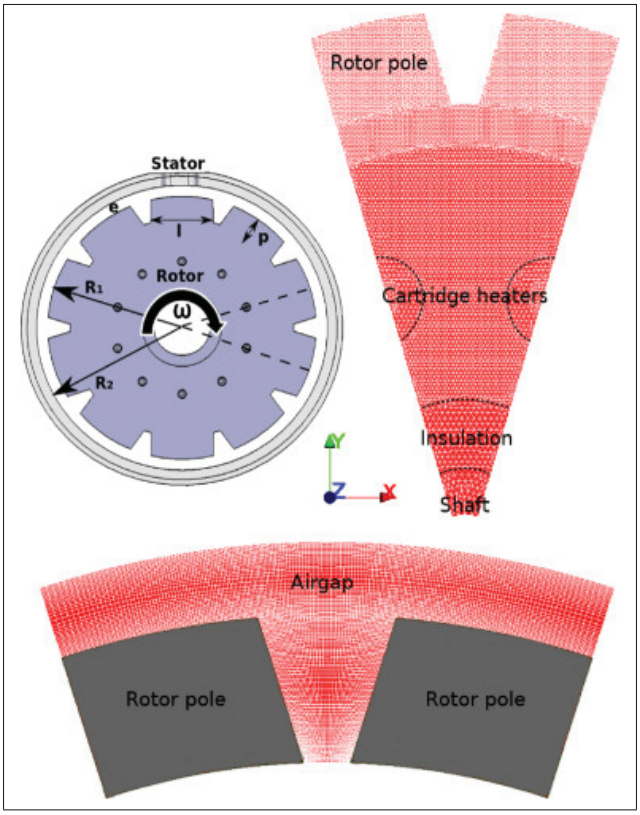

Figure 2.10 CAD geometry and mesh used in Lancial *et al.* (2017).

Li *et al.* (2017) presented a study on the temperature distribution on the exciting windings and fluid flow field between the rotor poles of a 250 MW fully air-cooled hydro-generator. The simplified model of the hydro-generator used in this study is depicted in Figure 2.11.

The conjugate heat transfer methodology was employed with the standard $k-\varepsilon$ turbulence model and the multiple frames of reference frozen rotor approach within the commercial CFD code, ANSYS FLUENT. The numerical results were validated by comparing with the available experimental data. It was demonstrated that the number of rotor ventilation ducts have a significant impact on the fluid flow field in the region between the rotor poles, as well as the temperature distribution on the excitation winding.

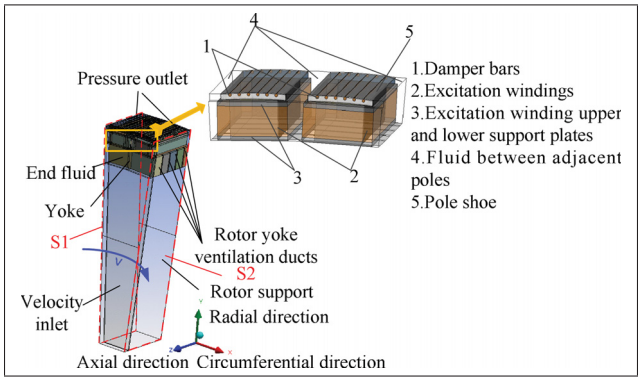

Figure 2.11 CAD geometry and mesh used in Li *et al.* (2017).

For the scale rotating model built at Hydro-Québec, apart from the CFD approach, the experimental measurements have been carried out to characterize the flow and thermal characteristics in the machine. Torriano *et al.* (2014) investigated the effect of rotation on heat transfer characteristics in the full scale rotating model of a hydro-generator using a hybrid method combining the experimental measurement and numerical modelling. Using the measured temperature on the surface of a heated pole, installed on an experimental model, as the boundary condition, the heat transfer coefficients on that surface were obtained through numerical simulations using the ANSYS CFX code. The results showed that the heat transfer coefficient distribution on the pole face is asymmetric since lower h values are observed on the trailing side region. Furthermore, although the rotor fans enhance the heat transfer rate at the top and bottom ends of the salient pole, the highest h values are found in an intermediate region. Lastly, it was found that the average heat transfer coefficients on the pole face at 300 rpm are four times higher than those at 50 rpm. Bach *et al.* (2015); Venne *et al.* (2016) presented the particle image velocimetry

(PIV) measurement of the flow field in several critical regions in the full scale rotating model, previously depicted in Torriano *et al.* (2014). A comparison of the experimentally measured flow field in the space between the cooler exit and the enclosure wall showed a very good agreement. The same statement can be made for the flow field in the covers and the inter-pole region, which confirmed the accuracy of the numerical CFD model.

Conclusions:

- The geometries of the experimental setting considered in each study differ from one to another, unless they are from the same university's laboratory or from the same manufacturer. Therefore, the flow field and the thermal characteristics differ and consequently the results obtained from one study cannot be applied to the other.
- The majority of numerical studies found in the literature employed either the commercial CFD codes, such as `ANSYS CFX` or `ANSYS FLUENT`, or the open source CFD package like `OpenFOAM`. This is due to the challenges of the CFD methodology for the rotating machinery applications, where a technique is required to couple the rotating and stationary parts. Although the rotor-stator coupling has long been examined in the CFD analysis of turbomachinery, neither in-house codes or open-source codes have been well adapted to capture this type of flow interaction.
- For the turbulence modelling, most of the published studies employed the Reynolds-averaged Navier-Stokes (RANS) turbulence closures. Higher fidelity turbulence modelling techniques such as the direct numerical simulation (DNS) or the large eddy simulation (LES) have been applied to the airflow and thermal analysis of hydro-generators.
- The Multiple Frames of Reference frozen rotor model is preferred over the mixing plane model since it exhibits a better numerical stability. Very good agreements between the flow fields predicted by the frozen rotor model and the experimental data were mainly found for the hydro-generator model with the axial cooling scheme (Moradnia *et al.*, 2014a,b). Also, the similar results between the cases computed by the frozen rotor and the mixing plane model only obtained for hydro-generators that have an axially cooled scheme (Schrittwieser *et al.*, 2014; Jamshidi *et al.*, 2015).

CHAPTER 3

METHODOLOGY

Given the fact that the measurement procedure on the full-scale rotating model is very challenging, the numerical CFD approach was used to characterized the flow in the machine. From the literature review it has been confirmed that the CFD results strongly depend on the choice of numerical models used, including the Multiple Frames of Reference models, the turbulence models, and the fluid-solid coupling methods. From the computational perspective, the study on the effects of numerical models on the accuracy of flow and thermal prediction cannot be performed on the full scale model due to the limit of the computing resources. Therefore, a numerical strategy consisting of two steps has been proposed which aims to study the effects of numerical settings on the accuracy of predictions. The methodology used in this thesis is illustrated in Figure 3.1.

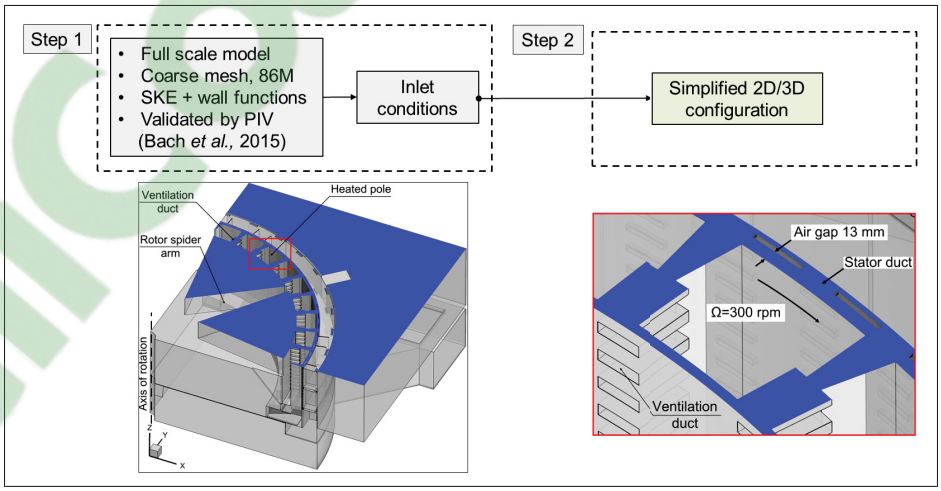

Figure 3.1 Numerical strategy employed to study the effects of numerical models.

In the first step, the CFD simulation is performed on the full scale model using standard $k-\varepsilon$ turbulence model and the wall function approach on a coarse mesh. The mesh for the full scale model consists of 86×10^6 nodes. The CFD simulation result is validated by comparing with the PIV measurement at several critical locations as reported in Bach *et al.* (2015). This CFD

result was then used to generate the boundary condition at the inlet for the simplified configuration in step 2.

In the second step, the numerical simulations were performed on the simplified configurations to study the effects of different numerical models on the accuracy of flow and thermal prediction in the air gap region. In particular, the effects of different multiple frame of refrence approaches, both steady state and unsteady models, are analyzed in terms of predicting the flows field in the air gap and stator ducts region. This analysis is performed on the a two-dimensional simplified models and presented in Chapter 4. The effects of turbulence models and the conjugate heat transfer with respect to the prediction of convective heat transfer coeffient on the pole face are shown in Chapter 5. Lastly, the effects of different turbulence models and thermal boundary conditions regarding the calculation of temperature on the pole face are demonstrated in Chapter 6.

CHAPTER 4

A PARAMETRIC ANALYSIS OF TURBULENT FLOW AND HEAT TRANSFER IN A HYDRO-GENERATOR ROTOR-STATOR SYSTEM

D.-D. Dang [1], X.-T. Pham[1], P. Labbe [2], F. Torriano [2], J.-F Morissette [2], C. Hudon [2]

[1] Department of Mechanical Engineering, École de Technologie Supérieure,
1100 Notre-Dame Ouest, Montréal, Québec, Canada H3C 1K3

[2] Institut de recherche d'Hydro-Québec,
1800 Boulevard Lionel-Boulet, Varennes, QC J3X 1S1

Article submitted to «Journal of Heat and Mass Transfer»,
in July, 2018.

Abstract

The present study is dedicated to a computational fluid dynamics investigation of convective heat transfer of a rotor-stator configuration that is commonly found in rotating electrical machines. The rotor-stator flow interaction is handled with different multiple frames of reference models, including the frozen rotor, the mixing plane, and the transient interface. The numerical results show that the flow field obtained with the mixing plane approach is similar to the one calculated by the transient model; whereas the frozen rotor model produces the flow field that significantly deviates from the reference transient solution. Moreover, computed results reveal that the convective heat transfer prediction on the rotor pole face is greatly affected by the choice of the turbulence models. The average values of heat transfer coefficients on the rotor surface numerically predicted by four turbulence modeling approaches are compared with the available experimental data, and a reasonable agreement is found for the case with the Shear Stress Transport $k-\omega$ model. Also in this work, effects of the solid heat conduction on the thermal performance prediction on the salient pole surfaces are analyzed in detail.

Keywords: hydro-generator, thermal analysis, rotor-stator interaction, mixing plane, conjugate heat transfer.

Nomenclature

Latin symbols

E	Total energy (J)
c_p	Specific heat capacity ($\mathrm{J{\cdot}kg^{-1}{\cdot}K^{-1}}$)
h	Heat transfer coefficient ($\mathrm{W{\cdot}m^{-2}{\cdot}K^{-1}}$)
λ	Thermal conductivity ($\mathrm{W{\cdot}m^{-1}{\cdot}K^{-1}}$)
P	Time-averaged pressure (Pa)
Pr_t	Turbulent Prandtl number
q_w	Wall heat flux ($\mathrm{W{\cdot}m^{-2}}$)
r	Radius (m)
T	Temperature (K)
U_i	Time-averaged velocity component ($\mathrm{m \cdot s^{-1}}$)
x_i	Cartesian coordinates (m)
X_i	Position vector component (m)
y^+	Dimensionless wall distance

Greek symbols

ε	Turbulent kinetic energy dissipation rate ($\mathrm{m^2{\cdot}s^{-3}}$)
ε_{ijk}	third-order alternating tensor
θ	Angular coordinate ($^\circ$)
ρ	Density ($\mathrm{kg{\cdot}m^{-3}}$)
ω	Specific dissipation rate (s^{-1})
Ω_i	Rotational speed components ($\mathrm{rad{\cdot}s^{-1}}$)
μ	Molecular dynamic viscosity ($\mathrm{kg{\cdot}m^{-1}{\cdot}s^{-1}}$)
μ_t	Turbulent dynamic viscosity ($\mathrm{kg{\cdot}m^{-1}{\cdot}s^{-1}}$)
τ_w	Wall shear stress ($\mathrm{kg{\cdot}m^{-1}{\cdot}s^{-2}}$)

Subscript

$conj$	conjugate heat transfer
$conv$	convective heat transfer
f	fluid
max	maximum
min	minimum
ref	reference
s	solid
t	turbulent
w	wall

4.1 Introduction

Although the conversion of the mechanical energy into electricity by large hydro-generators has a high efficiency ($\eta \approx 98\%$), this process consistently produces some losses. In the steady-state operation of a hydro-generator, these losses, introduced under the form of volume heat sources cause a temperature rise in the solid components of the machine. In order to keep the internal temperature of the machine within a safety limit, the heat is generally evacuated through the circulation of cooling air. Therefore, a detailed knowledge of the flow dynamics and the thermal performance in the hydro-generator is very important in the design of the machine.

With the advent of increasing computing power, Computational Fluid Dynamics (CFD) became a promising technique for the thermal analysis of electrical machines. Nonetheless, due to the extremely complex geometries, flows in these machines exhibit many complex phenomena which are challenging for CFD simulations, such as rotation, turbulence, and separation. One of the first studies that employed CFD simulations to perform the thermal analysis in the electric generator was published by Pickering *et al.* (2001). The numerical results showed that the local convective heat transfer coefficient (CHTC) on salient poles predicted by CFD differed from experimental data up to 30%. Schrittwieser *et al.* (2014) presented a comparison of the flow and thermal features at the stator duct of a hydro-generator predicted by the frozen rotor and the mixing plane models. The numerical results pointed out that the two models had similar predictions for the flow and thermal field since a difference of only 10% was obtained. Moradnia *et al.* (2014b) performed a study on the flow in an axially cooled generator using the frozen rotor model within the OpenFOAM code. The experimental data measured by Particle Image Velocimetry (PIV) technique was used to validate the numerical results and a very good agreement was observed.

Since the heat transfer coefficient was always regarded as an invariant descriptor of the convection with respect to the thermal boundary condition, a convective heat transfer approach was often used to calculate the CHTC distribution in many studies found in the literature. In fact, a simplified thermal boundary condition (a uniform heat flux or a uniform temperature)

was imposed on the fluid-solid boundary to close the thermo-fluid problem in the fluid domain. This approach, however, neglects the effect of solid heat conduction, which might result in inaccurate prediction of thermal performance. In the alternative *conjugate heat transfer* (CHT) formulation, the fluid dynamics equations are coupled with the solid heat conduction, which offers a better physical representation. Weili *et al.* (2013) employed CHT computations to analyze the cooling airflow and temperature distribution in a large hydro-generator. The numerically predicted average temperature values of the excitation winding was compared with the available experimental data, and a good agreement was obtained. Klomberg *et al.* (2015b) conducted a numerical study to characterize the convective heat transfer at the end winding region of a hydro-generator prototype. The computed results indicated that the CHTC value in this region were similar for the cases computed on meshes with different near-wall resolutions y^+ in the range of 1 to 8. Recently, Li *et al.* (2017) performed a CHT study to predict the temperature field on the exciting windings of a fully air-cooled hydro-generator. The numerical results pointed out that the number of rotor ventilation ducts have a significant impact on the flow field in the region between the rotor poles, as well as the temperature distribution on the excitation winding.

Although a number of studies have been carried out on the thermal analysis of electrical machine in recent years, there are relatively few works on the convective heat transfer features in the air gap region. Due to the challenges and the high cost of performing measurements under severe conditions, CFD modelling has became a popular tool to characterize the flow and thermal features in this critical region. Nevertheless, the accuracy of CFD prediction strongly depends on the numerical models applied and the current study aims to investigate the effects of numerical models on the convective heat transfer prediction in the rotor-stator system. More specifically, the effects of (1) Multiple Frames of Reference models, (2) turbulence modelling closures, and (3) thermal boundary conditions, are investigated. The thorough understanding on the behaviour of multiple frames of references models provided in this study is the foundation for the choice of rotor-stator interface model made in the recent work by Dang *et al.* (2018).

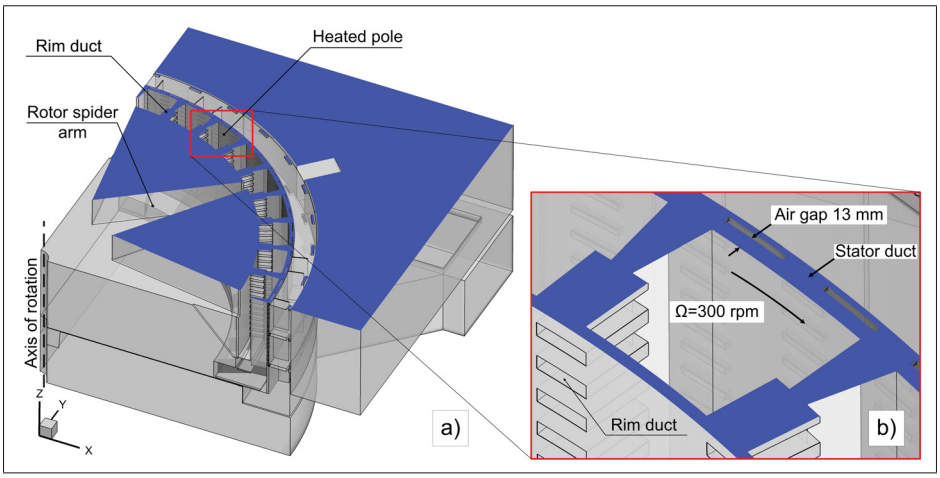

Figure 4.1 Computational domain of full scale model with XY cut plane.

4.2 Numerical model

4.2.1 Computational domain and grids

In order to gain a better understanding on the ventilation in hydro-generators, a rotating scale model was built at the Institut de recherche d'Hydro-Québec (IREQ) Torriano *et al.* (2014). Particle image velocimetry (PIV) measurements have been recently carried out to characterize the ventilation airflow in the full scale model, and they are presented in papers by Bach *et al.* (2015) and Venne *et al.* (2016). CFD simulations were performed on a 90° sector domain exploiting the periodicity feature of the geometry to predict the air flow in the rotating scale model, as illustrated in Figure 4.1a. The geometry of the full scale model presents a particular challenge in mesh generation due to the wide range of dimensions, which vary from a rotor-stator air gap of $1.3 \times 10^{-2}\ m$ to an inner rotor radius having a length scale two orders magnitude higher. Furthermore, numerical results can be affected by a wide range of parameters that cannot be evaluated through simulations on the full scale model due to the high computational cost. Therefore, in order to investigate the fluid flow and heat transfer within the whole domain of full scale model, the numerical analysis only focuses on the region shown in Figure 4.1b. The area represents a simplified version of the rotor-stator system found in the full

scale model. In order to specify the boundary conditions at the inlet of the simplified model, the mean flow and turbulent profiles were extracted from the CFD results performed on the full scale model.

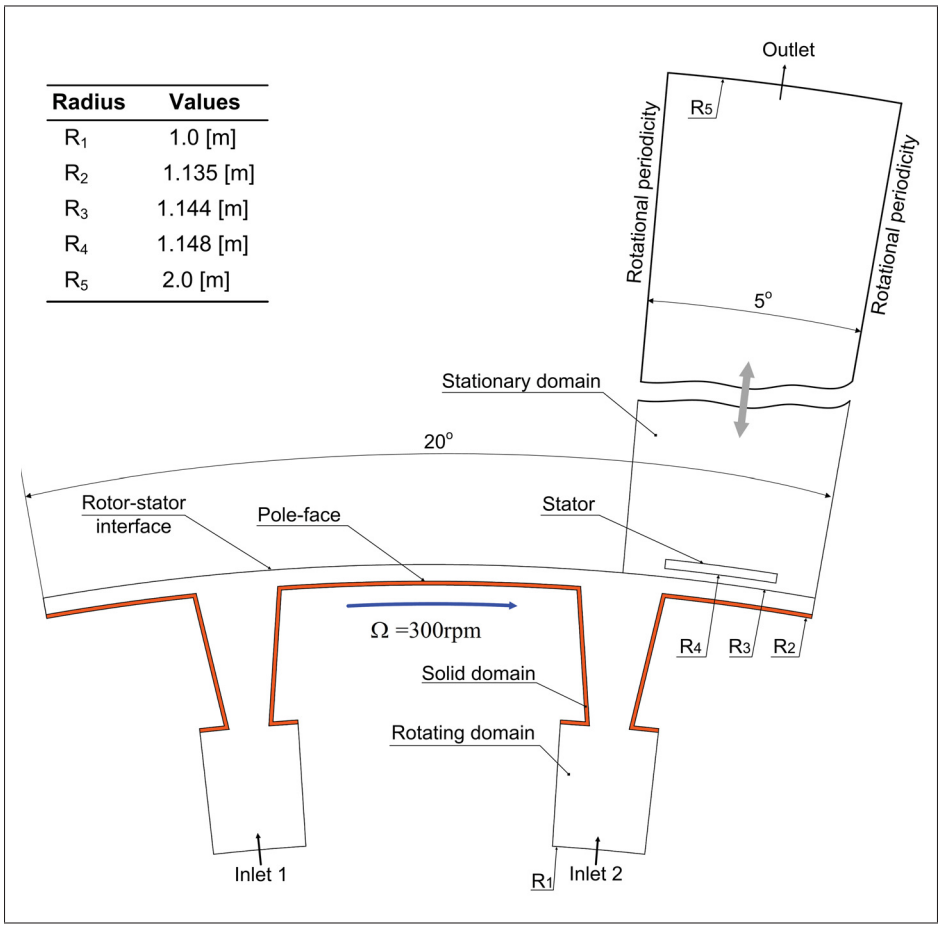

Figure 4.2 Geometry of two-dimensional simplified model.

The two-dimensional simplified model is schematically illustrated in Figure 4.2, which is composed of 20° sectors in the rotating fluid domain and the solid domain, and a 5° sector in the stationary fluid domain. In this simplified model, two inlet boundaries are included to represent the corresponding rim ducts in the full scale model. In order to eliminate the influence of conditions at the outlet to the prediction in the air gap region, this boundary is located at a distance 2 *m* from the stator wall.

The rotating fluid, the stationary fluid, and the rotor solid domains were meshed separately us-

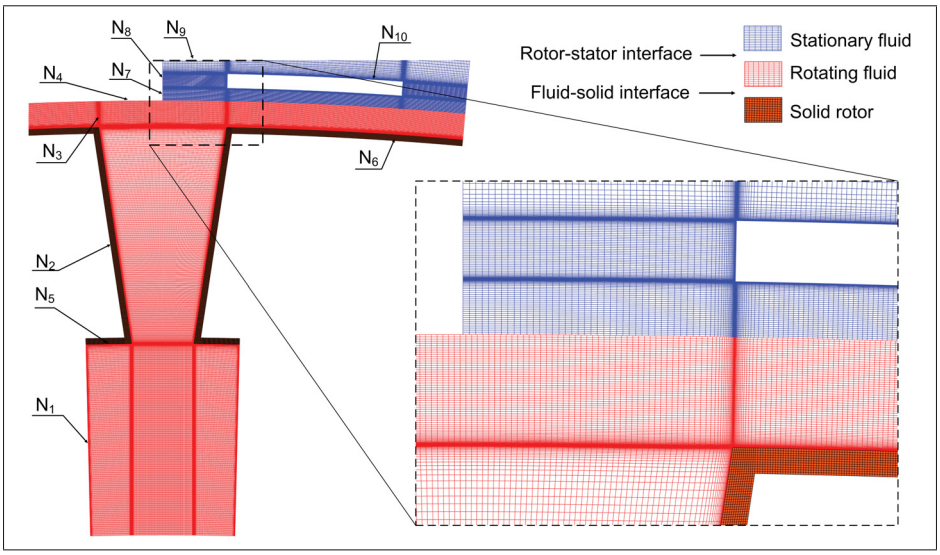

Figure 4.3 Meshes for rotating, stationary fluid and solid domains.

ing the meshing tool ANSYS ICEM. These unstructured meshes were merged in the numerical model using interfaces, as illustrated in Figure 4.3. The mesh used in this study was chosen based on a mesh independence analysis, and it has a total of 4×10^5 nodes, including 1.8×10^5 nodes in the rotating fluid domain, 2.1×10^5 nodes in the stationary fluid domain, and 1×10^4 nodes in the solid domain. The mesh characteristics are summarized in Table 4.1, for which the average dimensionless wall distance y^+ values was kept lower than 1 on all wall surfaces.

Pole face		**Leading-trailing**		**Stator wall**	
Δy	y^+	Δy	y^+	Δy	y^+
0.012	0.25	0.020	0.53-0.84	0.01	0.61

Table 4.1 Near-wall distance and averaged y^+ values

4.2.2 RANS equations and turbulence models

All simulations in this work are carried out with CFD code `ANSYS-CFX 16.0`, in which the governing equations are discretized by the control-volume based finite element formu-

lation (Schneider & Raw, 1987). The Reynold-averaged Navier-Stokes (RANS) equations, including the continuity (Equation 4.1), the momentum (Equation 4.2), and the energy (Equation 4.3) equations, are given for the incompressible, unsteady flow as follows:

$$\frac{\partial}{\partial x_j}\left(\rho U_j\right) = 0 \tag{4.1}$$

$$\begin{aligned}\frac{\partial}{\partial t}(\rho U_i) + \frac{\partial}{\partial x_j}(\rho U_i U_j) = \quad & -\tfrac{\partial P}{\partial x_i} + \tfrac{\partial \tau_{ij}}{\partial x_j} - \underbrace{2\rho\varepsilon_{ijk}\Omega_k U_j}_{Coriolis\ force} \\ & - \underbrace{\rho\left[\Omega_j X_j \Omega_i - \Omega_j X_i \Omega_j\right]}_{centrifugal\ force}\end{aligned} \tag{4.2}$$

$$\frac{\partial}{\partial x_j}\left[U_j\left(\rho E + p\right)\right] = \frac{\partial}{\partial x_j}\left[\left(\lambda_f + \frac{c_p \mu_t}{Pr_t}\right)\frac{\partial T}{\partial x_j}\right] + \frac{\partial}{\partial x_j}\left(U_i \tau_{ij}\right) \tag{4.3}$$

In the momentum equation, Ω_i and X_i are the rotational speed component and the position vector component, respectively; and the two last terms are included to take into account the Coriolis and centrifugal forces. In the energy equation, λ_f and c_p are the thermal conductivity and the specific heat capacity of fluid, respectively. The effective viscous stresses are related to the fluid motion by a constitutive equation of the form:

$$\tau_{ij} = \mu_{eff}\left(\frac{\partial U_i}{\partial x_j} + \frac{\partial U_j}{\partial x_i}\right) \tag{4.4}$$

where μ_{eff} is the effective viscosity, defined as the sum of the molecular μ and the turbulent eddy viscosity μ_t, $\mu_{eff} = \mu + \mu_t$.

To compute the turbulent viscosity μ_t, several two-equation turbulence closure models based on the eddy-viscosity approximation (Ferziger & Peric, 2002) were used. These turbulence models are the standard $k-\varepsilon$ (SKE) (Jones & Launder, 1973), the Re-Normalisation Group $k-\varepsilon$ (RNG) (Yakhot *et al.*, 1992), the standard $k-\omega$ (SKO) (Wilcox, 1988), and Shear Stress Transport $k-\omega$ (SST) Menter (1994). For the boundary layer modelling, the the ε-based turbulence models, i.e. the standard $k-\varepsilon$ and the RNG $k-\varepsilon$, use the CFX scalable wall-

function model, whereas the automatic wall treatment formulation is employed for the ω-based turbulence models, such as the standard $k-\omega$ or SST $k-\omega$ (ANSYS, 2015).

4.2.3 Rotor-Stator Interaction

It is well known that flows in rotor-stator systems are inherently unsteady due to the interaction between the rotor and stator components. The most accurate method to model a such system is thus found in transient simulations. However, in many industrial applications, such time-consuming calculations are not practicable. For this reason, different Multiple Frame of Reference (MFR) models were developed, including the mixing plane, the frozen rotor, and the transient interface models. In the MFR approach, the fluid near the rotor is solved in a rotating frame of reference, while the stator is modelled in a stationary frame of reference.

In the mixing plane model, the conserved flow variables are first circumferentially averaged at the exit of rotating fluid domain and then utilized to specify at the entry of the stationary fluid domain, and vice versa. This process of exchanging averaged variables forms an iterative procedure and is forced to stop when a flux balance is established on two sides of the rotor-stator interface. The details on the formulation and implementation of this interface model are thoroughly discussed in (Galpin *et al.*, 1995; Stein *et al.*, 2015).

Unlike the mixing plane approach, in the frozen rotor model, the circumferential averaging is not performed at the rotor-stator interface, and a local frame transformation is applied instead. For the frozen rotor model, the flow structure in the circumferential direction is maintained through the interface; nevertheless, the position of rotor is fixed relatively to the stator. In comparison with the mixing plane model, the frozen rotor demonstrated a better numerical stability since there is no exchange of averaged variables at the rotor-stator interface. Therefore, this model has been intensively used in many studies in the past (Shanel *et al.*, 2000, 2003; Weili *et al.*, 2013; Moradnia *et al.*, 2014b) and a good agreement with experimental data was found for the cases of axial flows with weak rotor-stator interaction (Moradnia *et al.*, 2014b).

To predict the unsteady effects resulted from the rotor-stator interaction, the transient interface model is also available. In the transient simulations, the rotating domain moves relatively to

the stationary one at for each time step according to the rotational speed and the time step size. The flow field variation in both time and space due to the interaction between the rotating and stationary components is fully taken account. In the current study, a comparison of the computed results using the frozen rotor, mixing plane, and transient interface models is presented in Sec. 4.3.2.

4.2.4 Boundary conditions and convergence settings

At the two inlets, the mean flow and turbulence profiles obtained from the numerical results of the experimental model are applied as discussed above. The inlet temperature was set at $T_{inlet} = 318\ K$. The no-slip boundary conditions were specified on all surfaces of the stator walls, the pole face, and the rim ducts. The rotational periodic interfaces were specified in the circumferential direction of the rotating fluid, stationary fluid and the solid domains. At the outlet boundary, an averaged zero static pressure was specified using a blending factor of 5%. Since the `ANSYS CFX` code used in this study only supports three-dimensional simulations (ANSYS, 2015), the two-dimensional cases are thus performed using the pseudo-3D setup. Thus, the computational domain is extended in the span-wise direction and symmetry boundary condition are specified at both ends.

In the solid domain, the volumetric heat source was defined in order to have the rotor surface temperatures similar to the values measured in Torriano *et al.* (2014), which are in the range of 80°-90°C. The rotor part of this system has a rotational speed of 300 rpm, for which the corresponding Reynolds number is of 2.95×10^4. The main properties of fluid, including the the specific heat capacity, the dynamic viscosity, and the thermal conductivity, are used as temperature dependent properties (Klomberg *et al.*, 2015b). For calculations carried out with the constant fluid properties, the values are given in Table 4.2.

A time step $\Delta t = 5.55 \times 10^{-5}$ s was chosen, for which 200 iterations are required for the rotating domain of 20° to pass over the stationary components at the rotational speed of 300 rpm. To study the sensitivity of the time step size, transient simulations were also performed with the time step sizes $2 \cdot \Delta t$ and $\Delta t/2$ and the results are presented in Sec. 4.3.2.

Physical properties	Air	Solid
Density ($kg.m^{-3}$)	1.15	7.85×10^3
Thermal conductivity ($W.m^{-1}.K^{-1}$)	2.61×10^{-2}	6.05×10^1
Specific heat capacity ($J.kg^{-1}.K^{-1}$)	1.0044×10^3	4.34×10^2
Dynamic viscosity ($kg.m^{-1}.s^{-1}$)	1.831×10^{-5}	-

Table 4.2 Physical properties of air and solid.

The convergence was assessed by examining residuals of flow variables as well as by monitoring the variation of relevant quantities at specific locations in the flow field. The convergence criteria were that the maximum residuals should be less than 10^{-4} for all flow variables excluding the energy equation, for which the criteria was 10^{-6}. In addition to monitoring residuals and variation of flow quantities, the global conservation in each domain was also checked, by allowing a maximum imbalance of 1% for flow and thermal variables.

4.3 Results and discussion

4.3.1 Mesh independent analysis

In order to determine the optimal number of nodes that results in a mesh independent solution, a mesh sensitivity study was conducted. The Grid Convergence Index (GCI) (gci, 2008) was used to evaluate the mesh independence through estimation of the numerical discretization error.

To calculate GCI, three meshes of different resolutions were generated, the fine mesh with cell size s_1, the medium one with size s_2, and the coarse one with size s_3. The meshes were systematically refined by changing the number of nodes N_i, $i = 1-10$ at the locations illustrated in Figure 4.3. The mesh parameters are summarized in Table 4.3, where the mesh M_2 was refined from mesh M_3 with a refinement factor $r_{32} = s_3/s_2 = 1.37$, and mesh M_1 from M_2 with a factor $r_{21} = s_2/s_1 = 1.40$. In this analysis, all simulations were conducted using the SST $k-\omega$ model in combination with the mixing plane model.

Since the convective heat transfer prediction is strongly related to the accuracy of the wall shear stress calculation (Moradnia *et al.*, 2014b), this parameter is selected to quantify the quality of

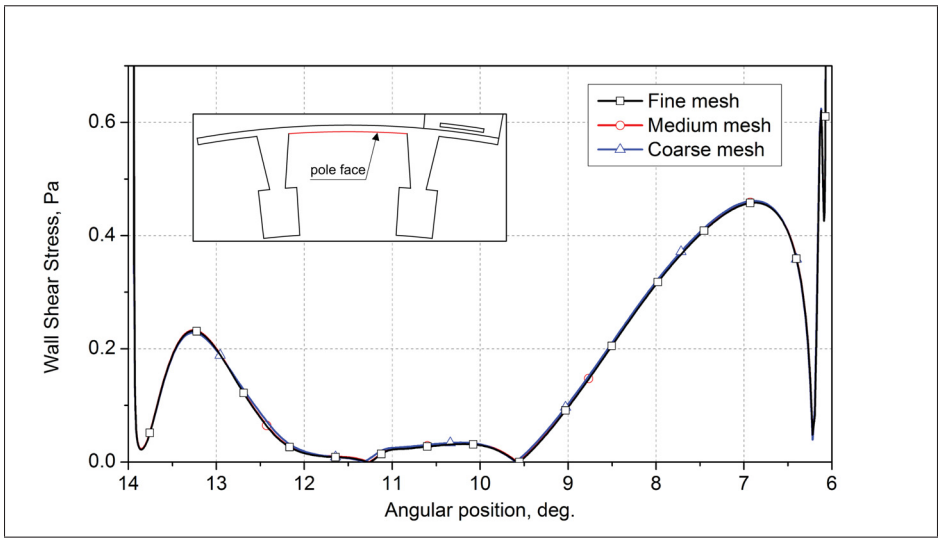

Figure 4.4 Wall shear stress on pole face.

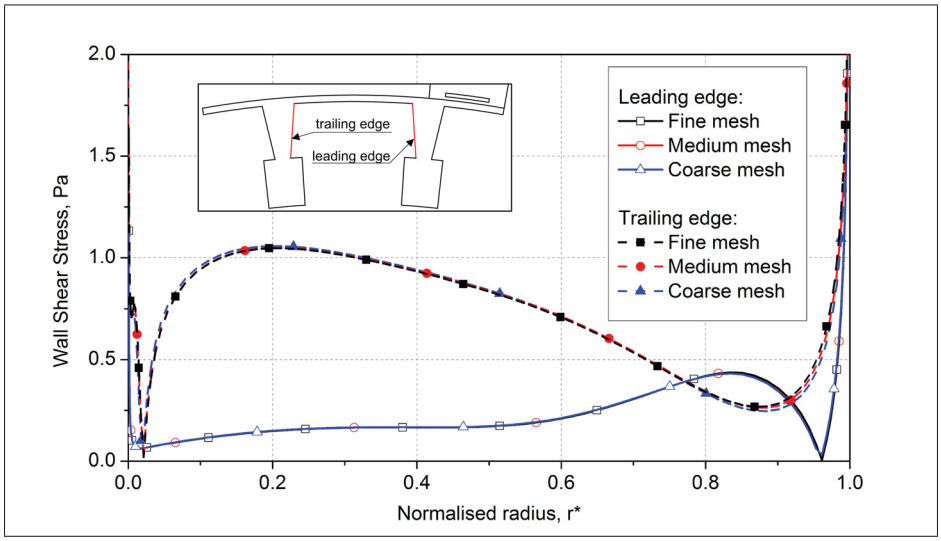

Figure 4.5 Wall shear stress on the leading and trailing edges.

mesh. The results are shown in Figure 4.4 and Figure 4.5 for the wall shear stress profiles on the pole face, the leading and trailing edges, respectively.

Moreover, averaged values of the wall shear stress, $\overline{\tau_w}$, over the pole face, the leading and trailing edges were chosen to calculate the GCI.

The GCI calculation starts with the determination of the apparent order p, obtained by solving

	N_1	N_2	N_3	N_4	N_5	N_6	N_7	N_8	N_9	N_{10}
M_1(fine)	120	150	70	120	80	120	60	80	80	200
M_2(medium)	80	100	50	80	60	100	40	60	60	160
M_3(coarse)	50	70	35	60	50	60	25	45	40	110

Table 4.3 Mesh refinement in the rotating and stationary domains.

the following equation:

$$p = \frac{1}{ln(r_{21})}\left| ln\left|\frac{\phi_3 - \phi_2}{\phi_2 - \phi_1}\right| + ln\left(\frac{r_{21}^p - s}{r_{32}^p - s}\right)\right| \tag{4.5}$$

where ϕ_k denotes the solution on the mesh M_k (in this case, $\phi = \overline{\tau_w}$), $k = 1,2,3$ and $s = 1$ or -1 depending on the sign of $(\phi_3 - \phi_2)/(\phi_2 - \phi_1)$.

The extrapolated values are calculated from:

$$\phi_{ext}^{21} = (r_{21}^p \phi_1 - \phi_2)/(r_{21}^p - 1) \tag{4.6}$$

The approximate relative error e_a^{21}, and the extrapolated error e_{ext}^{21} are calculated by:

$$e_a^{21} = \left|\frac{\phi_1 - \phi_2}{\phi_1}\right| \tag{4.7}$$

$$e_{ext}^{21} = \left|\frac{\phi_{ext}^{21} - \phi_1}{\phi_{ext}^{21}}\right| \tag{4.8}$$

The fine-mesh convergence index is estimated as:

$$GCI_{fine}^{21} = \frac{1.25 e_a^{21}}{r_{21}^p - 1} \tag{4.9}$$

The results of the GCI calculation on the different meshes are reported in Table 4.4, according to which the GCI values for the fine and the medium meshes are less than 1% and 1.5%, respectively. The decrease of GCI values for the considered variable at critical locations (i.e. $GCI_{21} < GCI_{23}$) indicates that the dependency of the numerical results on the mesh size is reduced with systematic mesh refinement and the solution tends toward a mesh independent

one.

	$\phi = \overline{\tau_w} - poleface$	$\phi = \overline{\tau_w} - leading$	$\phi = \overline{\tau_w} - trailing$
$N_{M_1}, N_{M_2}, N_{M_3}$	776310, 394520, 210350	-	-
r_{21}	1.4028	-	-
r_{32}	1.3695	-	-
ϕ_1	0.162092	0.271706	0.651462
ϕ_2	0.161552	0.272759	0.647375
ϕ_3	0.160625	0.274219	0.639374
p	1.6460	1.2294	2.2935
$e^{21}_{ext}(\%)$	0.4692	0.2697	0.5347
$e^{21}_{a}(\%)$	0.3498	0.3876	0.6274
$GCI^{21}_{fine}(\%)$	0.5865	0.9388	0.6684
$GCI^{32}_{med}(\%)$	1.0273	0.4178	1.4618

Table 4.4 Grid Convergence Index calculation result.

As the refinement from mesh M_2 to M_1 only reduced the discretization error by 1%, while increased the computational cost by a factor of two ($N_{M_1} \approx 2 \times N_{M_2}$), the mesh M_2 was chosen to perform further simulations.

4.3.2 Effect of Multiple Frame of Reference models

For the purpose of understanding the behavior of multiple frames of reference models, numerical simulations were performed using different approaches at the interface, including (1) the frozen rotor model, (2) the mixing plane model, and (3) the transient interface model. The result computed by the transient interface model is considered as the reference solution to evaluate the capability of steady state models. To speed up the convergence, a result computed by the mixing plane model was used to initialize transient simulations, for which 40 hours of the CPU time is typically required to reach a periodic solution.

Figure 4.6 shows the comparison of the radial velocity at the stator duct for different rotor-stator coupling models. At first, one can notice that the time-averaged transient results obtained with different time step sizes are almost identical, which means that the chosen time step is adequate for this configuration. Secondly, the data indicate that the mixing plane model predicts a

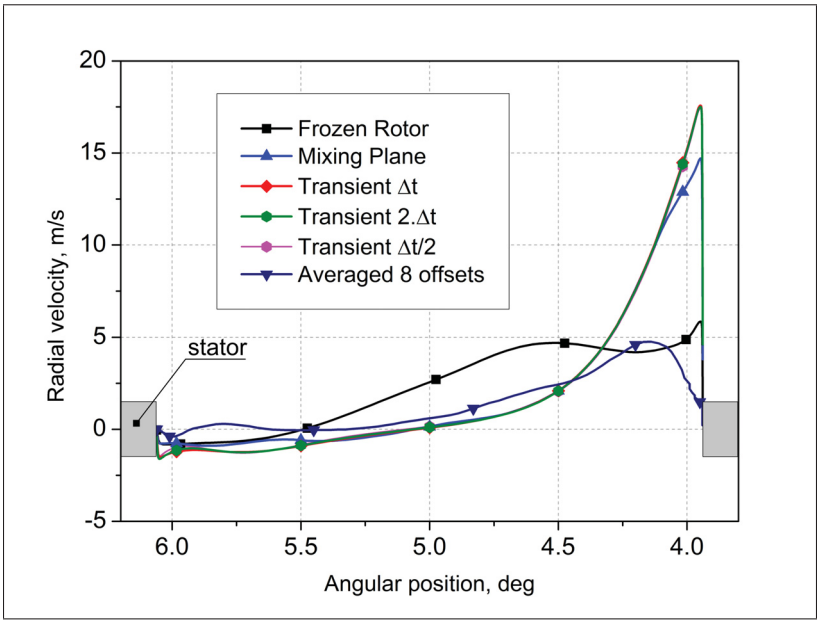

Figure 4.6 Radial velocity through the stator duct using different MFR models.

radial velocity profiles that is close to the one computed by the transient interface model. On the opposite, the flow fields calculated with the frozen rotor model are sensitive to the relative position between the rotor and stator and they considerably deviate from the reference solution. For the case of the real large hydro-generators with the radial cooling scheme, numerical simulations with mixing plane model frequently experienced instability issues, and thus the frozen rotor model has been used to predict the flow field. In this study, additional computations were carried out for the frozen rotor model with 8 different offset values (0°,2.5°,5°,...,17.5°). The average result of these offset positions was then taken to compare with the reference one to verify if it could represent the flow field in a manner similar to the one obtained form a mixing plane model. The profile of the averaged 8 offset positions plotted in Figure 4.6 points out that the average profile is better than the one predicted by a single frozen rotor simulation, but it still substantially differs from the transient reference solution.

In Figure 4.7, the circumferential velocity profiles at the rotor-stator interface calculated by different MFR models are plotted. The data show that the same conclusion as above can be drawn since the results provided by the mixing plane model well agree with the reference tran-

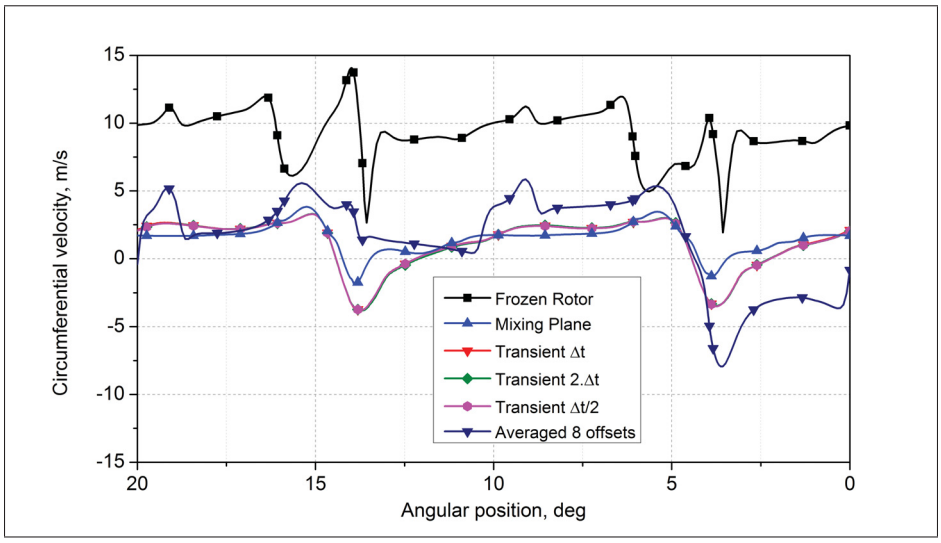

Figure 4.7 Comparison of circumferential velocity profile at the rotor-stator interface for different MFR models.

sient simulation, whereas certain deviations are found for the frozen rotor model.

Also, it should be noted that the mesh topology in the rotating and stationary fluid domains are identical for all simulations, however the number of mesh nodes in the simulations using the frozen rotor model is significantly higher (1×10^6 nodes). Since this model requires that the stationary and rotating domains must have the same pitch of 20°.

In summary, from a pure numerical perspective, the mixing plane model provides results with a reasonable accuracy compared to the much more computationally expensive transient simulation. On the opposite, the results computed with the frozen rotor model are strongly sensitive to the relative position between the rotor and the stator, and deviate from the transient reference solution. Furthermore, compared to the mixing plane, simulations using the frozen rotor model require 2.6 times more mesh nodes.

4.3.3 Effect of turbulence models

In complex flow modelling, the prediction of convective heat transfer phenomena is greatly affected by the choice of turbulence modelling approach (Howey *et al.*, 2012; Bourgeois *et al.*, 2011). In order to determine the most suitable turbulence model for this rotor-stator system,

four turbulence models, including the standard $k-\varepsilon$ model, the RNG $k-\varepsilon$ model, the standard $k-\omega$ model, and the SST $k-\omega$ model, were tested.

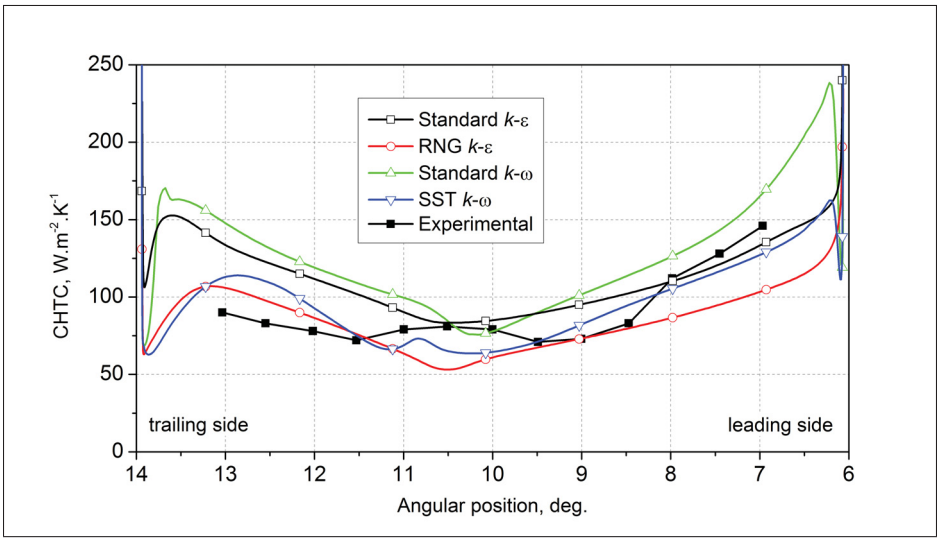

Figure 4.8 CHTC distribution on the pole surface predicted by different turbulence models.

Figure 4.8 shows the comparison between the CHTC distribution numerically computed on the pole face and the one obtained from the experimental data (Torriano *et al.*, 2014). The CHTC is defined as:

$$h = \frac{q_w}{T_w - T_{ref}} \tag{4.10}$$

where the q_w is the wall heat flux, T_w is the wall temperature, and T_{ref} is the reference temperature. The results show that the choice of turbulence model has a significant influence on the heat transfer prediction on the pole face. The standard $k-\varepsilon$ model and the standard $k-\omega$ models tend to overpredict the CHTC, while the RNG $k-\varepsilon$ and SST $k-\omega$ models produce results that better match with the measured values. This finding is in agreement with previous studies in the literature (Menter, 1994) which showed that the standard $k-\varepsilon$ model consistently overpredicts the turbulence kinetic energy level and thus the CHTC values.

In Figure 4.9, the average values of CHTC on the pole face calculated by four turbulence modelling approaches are presented. On average the relative errors in comparison with the experimental value for the computed CHTCs are 24.1% for the standard $k-\varepsilon$, 13.2% for the

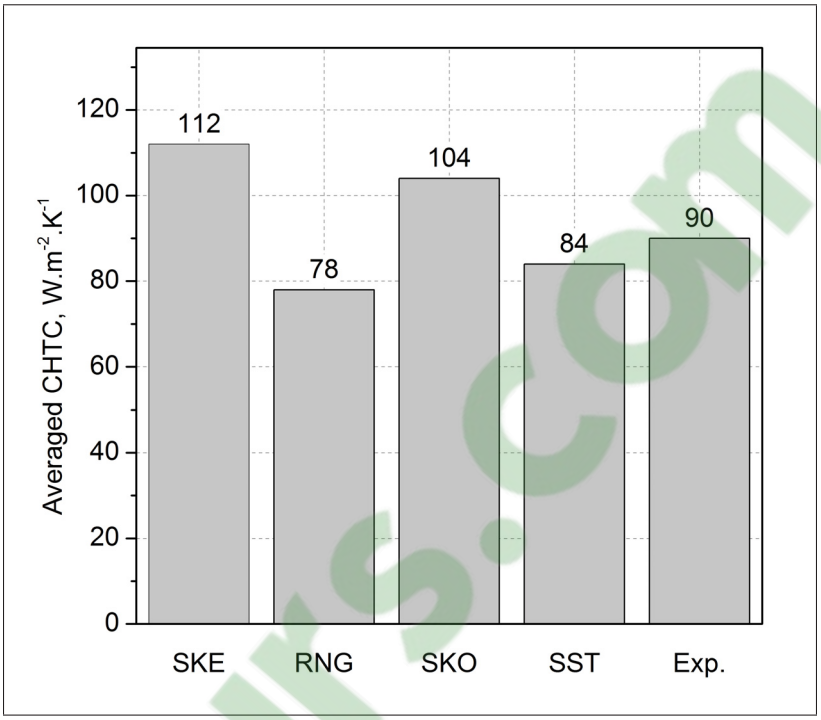

Figure 4.9 Average CHTC on pole face obtained from turbulence models.

RNG $k-\varepsilon$, 14.5% for the standard $k-\omega$, and 7.4% for the SST $k-\omega$. Although a certain deviation from the experimental result was observed in the CHTC distribution computed by SST, the difference for the average CHTC is relatively small.

4.3.4 Effect of thermal boundary conditions

Cases	Thermal boundary condition
1	Uniform heat flux $q_w = 2.0\ kW.m^{-2}$
2	Uniform heat flux $q_w = 20\ kW.m^{-2}$
3	Conjugate heat transfer

Table 4.5 Thermal boundary condition effects

In order investigate the influence of the solid heat conduction on the CHTC prediction on the surfaces of the salient pole, numerical simulations using different thermal boundary conditions were performed, as summarized in Table 4.5. For all cases in Table 4.5, the SST $k-\omega$ turbu-

lence model and temperature-dependent fluid properties were employed. In cases 1 and 2, the solid domains are removed from the model and uniform heat fluxes with different magnitudes were applied on convective boundaries. Two heat flux magnitudes were chosen, the first value ($2.0\ kW.m^{-2}$) corresponds to the average wall heat flux on the pole surfaces calculated by conjugate heat transfer computations in case 3, the second on was chosen as 10 times larger than the average value to study the sensitivity.

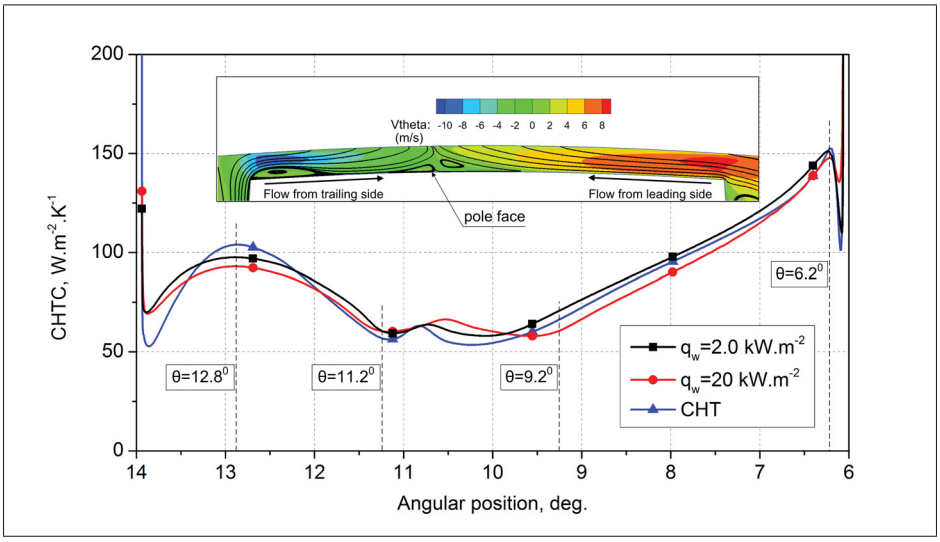

Figure 4.10 CHTC prediction using various thermal boundary conditions.

Figure 4.10 shows the CHTC distribution on the pole face obtained for the cases described in Table 4.5. For the conjugate heat transfer case, on a portion of the leading ($6.2^0 < \theta < 9.2^0$) and trailing side ($12.8^0 > \theta > 11.2^0$) the CHTC distribution gradually decreases as the flow boundary layers develop on the pole face, as shown in the zoomed view of Figure 4.10. The local maximum values are observed near the ends of the pole face where flow reattaches to the wall ($\theta = 6.2^0$ and $\theta = 12.2^0$). In the central region, a lower CHTC values are obtained since a complex flow structure with recirculation bubbles is observed.

A direct comparison between the purely convective cases (Case 1 and Case 2) and conjugate configuration (Case 3) is presented in Figure 4.11, where the relative difference is defined as $\Delta h = (h_{conv} - h_{conj})/h_{conj}$. The data show that in the upstream region of the pole face,

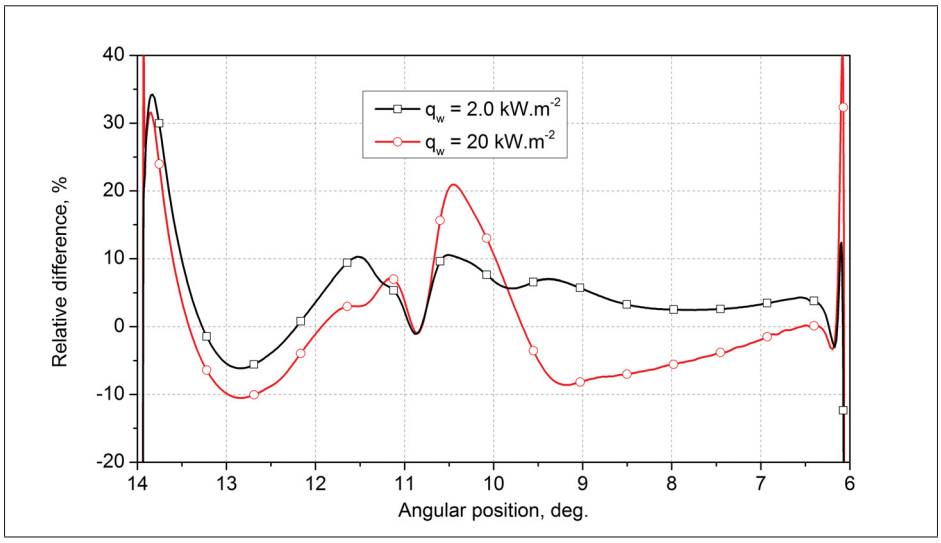

Figure 4.11 Relative error between the uniform heat flux computations and conjugate heat transfer computation.

$6.2^0 < \theta < 9.2^0$, the relative difference between the CHTCs distribution predicted Case 1 & 2 and Case 3 is within 10% as the heat is extracted from the solid dominantly by convection mode. On the contrary, the CHTC calculated by Case 1 & 2 are overestimated by up to 34% compared to that calculated by Case 3 in the downstream of the pole face. It should be noted that the overestimation of the minimum values of CHTC is related to the underestimation of the local maximum temperature (Coletti *et al.*, 2012).

In Figure 4.12, the CHTC profiles on the leading and trailing edges are plotted. The data show that the CHTC on the trailing is higher than that on the leading edge, which can be explained as an effect of the inlet boundary conditions. In fact, the cooling airflow penetrates the rotor rim ducts with a large angle of incidence impinging on the leading edge of the rim duct. Afterwards, the fluid is accelerated and deflected toward the trailing edge over the step. Thus, in the downstream zone following the step, a wall-attached flow develops on the trailing side whereas a large separation bubble is formed on the leading side. These flow features are illustrated in the zoomed view of the same figure.

The relative difference between CHTC on the leading and trailing edges predicted by Case 1 & 2 and Case 3 are reported in Figure 4.13. On the trailing side, the CHTC computed with

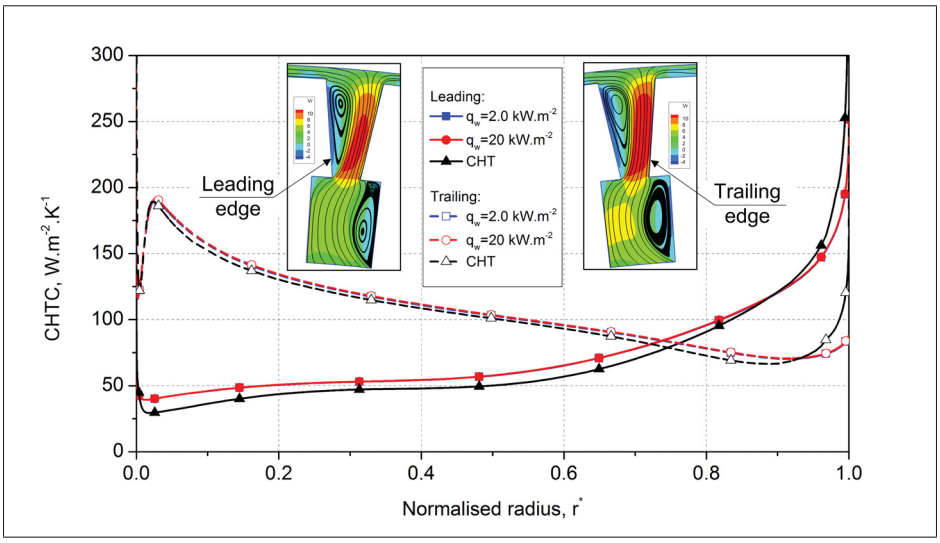

Figure 4.12 CHTC prediction on the leading and trailing edges using various thermal boundary conditions.

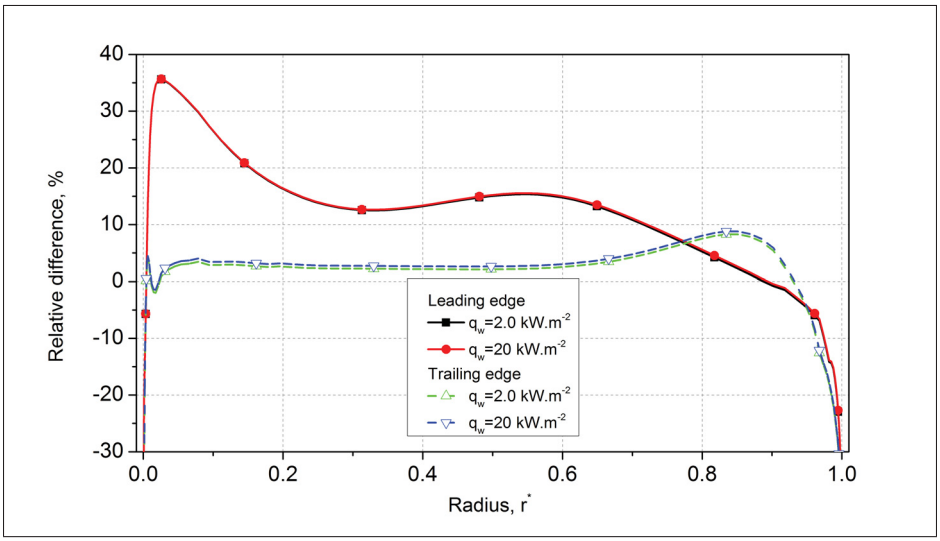

Figure 4.13 Relative difference to CHT of CHTCs predicted using different thermal boundary conditions.

the pure convective and the conjugate cases are nearly identical since the relative difference is lower than 10%. However, on the leading side, the CHTC distribution is greatly affected by the solid heat conduction, as the use of pure convective model overestimated the CHTC up to 35%.

In summary, the solid heat conduction has different effects on the thermal prediction in the air gap region depending on the local flow characteristics. The maximum value of Δh is observed near the flow recirculation region. This location corresponds to the local minimum value of CHTC where heat conduction is the dominant heat transfer mode. The pure convective heat transfer simulations are still reliable for simple flows but for complex ones with the recirculation or separation, the CHT method shows a better accuracy.

4.4 Conclusions and limitations

The current work presented the computational fluid dynamics simulations in order to predict the flow and thermal features in a two-dimensional rotor-stator configuration. It mainly focused on the effects of different rotor-stator coupling techniques, of RANS turbulence models, and of thermal boundary conditions. Experimental data of the convective heat transfer coefficients on the pole face (Torriano *et al.*, 2014) were used to validate the numerical results, which demonstrated that:

- The mixing plane model produced results more similar to those obtained by time-averaged transient interface model, whereas, the frozen rotor model showed a strong dependency on the position of the rotor with respect to the stator. Additionally, simulations using the frozen rotor model required more computational resource compared to the mixing plane model since the same pitch angle must be specified for the stationary and rotating domains.
- The prediction of convective heat transfer in the air gap region were strongly affected by the choice of turbulence models applied. The SST $k-\omega$ model was found to be the most appropriate for the calculation of convective heat transfer coefficients on the pole face since it produced the results that better matched with the experimental data.
- The thermal boundary conditions had different effects on the CHTC prediction depending on the local flow characteristics. The solid heat conduction has a strong influence in the recirculation region, where the cooling air extracts the heat mainly by conduction mode. The maximum overestimation of the convective heat transfer coefficient was found to be 35%. On the contrary, in the regions where the flows remains attached to the walls, the

CHTC values computed by the conjugate and pure convective heat transfer model were quite similar with a maximum relative difference smaller than 10%.

The future work will aim at simulating a more realistic geometry to improve the predictions, and the use of more enhanced turbulence modelling techniques such as the LES or hybrid LES/RANS models will be considered.

CHAPTER 5

COMPUTATIONAL FLUID DYNAMICS ANALYSIS OF TURBULENT CONVECTIVE HEAT TRANSFER IN A HYDRO-GENERATOR ROTOR-STATOR SYSTEM

D.-D. Dang [1], X.-T. Pham[1], P. Labbe [2], F. Torriano [2], J.-F Morissette [2], C. Hudon [2]

[1] Department of Mechanical Engineering, École de Technologie Supérieure,
1100 Notre-Dame Ouest, Montréal, Québec, Canada H3C 1K3

[2] Institut de recherche d'Hydro-Québec,
1800 Boulevard Lionel-Boulet, Varennes, QC J3X 1S1

Article published in «Applied Thermal Engineering»,
Volume 130, 5 February 2018, Pages 17-28.

Abstract

This paper presents a numerical analysis of turbulent flow and heat transfer in the rotor-stator system of a hydro-generator scale model. The study is carried out through Computational Fluid Dynamics simulations using Reynolds-Averaged Navier-Stokes turbulence models based on the eddy-viscosity approximation. To reduce the computational cost, the steady state Multiple Frames of Reference mixing plane model is employed to handle the inherently unsteady flow in the rotor-stator system. Results point out that the mean flow, the turbulence field and the heat transfer in the rotor-stator air-gap are particularly sensitive to the turbulence model used. The comparison between the numerical results and the experimental data shows that the Shear Stress Transport $k-\omega$ model provides with reasonable accuracy the convective heat transfer values on the rotor pole face. Also in this work, the effects of thermal boundary conditions and fluid properties on the computed heat transfer coefficient are analysed in detail. It is found that the use of conjugate heat transfer method and temperature-dependent air properties improves the accuracy of the numerical predictions.

Keywords: hydro-generator, rotor-stator system, thermal analysis, conjugate heat transfer, Computational Fluid Dynamics.

Nomenclature

Latin symbols

E	Total energy (J)
c_p	Specific heat capacity ($\mathrm{J{\cdot}kg^{-1}{\cdot}K^{-1}}$)
h	Heat transfer coefficient ($\mathrm{W{\cdot}m^{-2}{\cdot}K^{-1}}$)
λ	Thermal conductivity ($\mathrm{W{\cdot}m^{-1}{\cdot}K^{-1}}$)
P	Time-averaged pressure (Pa)
Pr_t	Turbulent Prandtl number
q_w	Wall heat flux ($\mathrm{W{\cdot}m^{-2}}$)
r	Radius (m)
r^*	Dimensionless radius $= (r - r_{min})/(r_{max} - r_{min})$
T	Temperature (K)
T^*	Dimensionless temperature $= (T - T_{min})/(T_{max} - T_{min})$
U_i	Time-averaged velocity component ($\mathrm{m \cdot s^{-1}}$)
U_R	Rotor tip velocity ($\mathrm{m \cdot s^{-1}}$)
x_i	Cartesian coordinates (m)
X_i	Position vector component (m)
y^+	Dimensionless wall distance

Greek symbols

ε	Turbulent kinetic energy dissipation rate ($\mathrm{m^2{\cdot}s^{-3}}$)
ε_{ijk}	third-order alternating tensor
θ	Angular coordinate ($^\circ$)
ν	Kinematic viscosity ($\mathrm{m^2{\cdot}s^{-1}}$)
ρ	Density ($\mathrm{kg{\cdot}m^{-3}}$)
ω	Specific dissipation rate (s^{-1})
Ω_i	Rotational speed components ($\mathrm{rad{\cdot}s^{-1}}$)
μ	Molecular dynamic viscosity ($\mathrm{kg{\cdot}m^{-1}{\cdot}s^{-1}}$)

μ_t	Turbulent dynamic viscosity ($kg \cdot m^{-1} \cdot s^{-1}$)
τ_w	Wall shear stress ($kg \cdot m^{-1} \cdot s^{-2}$)

Subscript

$conj$	conjugate heat transfer
$conv$	convective heat transfer
f	fluid
max	maximum
min	minimum
ref	reference
s	solid
t	turbulent
w	wall

Abbreviation

CFD	Computational Fluid Dynamics
CHT	Conjugate Heat Transfer
CHTC	Convective Heat Transfer Coefficient
GGI	General Grid Interface
IREQ	Institut de Recherche d'Hydro-Quebec
LPTN	Lumped-Parameters Thermal Network
LRNM	Low-Reynolds Number Model
MFR	Multiple Frames of References
PIV	Particle Image Velocimetry
RANS	Reynolds-Averaged Navier-Stokes
RNG	ReNormalization Group
SST	Shear Stress Transport
WF	Wall Function

5.1 Introduction

Experimental observations have confirmed that when hydro-generators operate beyond a certain power level, their components tend to overheat. The temperature rise in the solid is caused by electromagnetic and electrical losses under the form of volume heat sources. It is well known that the excessively high temperatures might shorten the lifetime of the electrical machine and even cause a severe failure. According to the statistics reported in (CIGRE, 2003), the most common failure in hydro-generators is the damage of insulation in the rotor and stator copper windings, which are made of thermally-limited materials. Consequently, understanding the thermal performance is very important in the design or in the power upgrade of hydro-generators.

In general, to maintain the components temperature within an acceptable margin, the heat must be extracted through the circulation of air, which is then cooled by water-cooled radiators. Therefore, the key factor determining the thermal performance of a hydro-generator is the convective heat transfer at solid surfaces, which is a complex function of the geometry and of the fluid dynamics (Howey *et al.*, 2012).

According to Boglietti *et al.* (2009), Lumped-Parameter Thermal Network (LPTN), Finite Element Analysis (FEA) and Computational Fluid Dynamics (CFD) are the three most common methods employed for thermal analysis of electrical machines. Owing to either a relative low computational cost (LPTN) or a strong mathematical formulation (FEA), these two methods have been actively used for the thermal and electromagnetic analysis of electrical machines. Although LPTN and FEA have demonstrated to be effective tools for thermal analysis, these methods require empirical data for convective heat transfer coefficients (CHTC) at the fluid-solid interfaces (Traxler-Samek *et al.*, 2010b). Traditionally, CHTC were evaluated by correlations which are widely available in heat transfer textbooks. However, since the empirical correlations were established for simple configurations and a certain flow regime, they may not be sufficiently accurate for cases with very complex geometries. Moreover, the empirical correlations evaluate an average CHTC for a whole surface, which means that the spatial distribution is not taken into account.

Due to the drawbacks of the empirical correlations approach, an enhanced modelling technique would be preferred, in which the detailed information on fluid flow and on heat transfer is taken into account. Nevertheless, the numerical modelling of the air flow and heat transfer for rotating electrical machines is not a trivial task due to numerous challenges, such as the geometrical complexity, rotational effects and turbulence. One of the main advantages of using CFD is that the numerical simulations provide the detailed structure of the thermal boundary layers, which is valuable for the convective heat transfer analysis. The application of CFD for the air flow and heat transfer analysis in electrical machines was firstly reported by Pickering *et al.* (2001). The simulations were performed on an air-cooled 4-poles generator using the $k-\varepsilon$ model with the standard wall function approach for the boundary layer modelling. The results showed that, in comparison with the experimental data, the air flow rate through stator ducts and local heat transfer coefficients predicted by CFD differed up to 20% and 30%, respectively. Schrittwieser *et al.* (2014) also numerically investigated the air flow and heat transfer in the stator duct of a hydro-generator using CFD simulations. The results pointed out that the flow and thermal fields, computed using two steady-state models, frozen rotor and mixing plane, were quite similar since a discrepancy of only 10% in average was observed. Moradnia *et al.* (2014b) studied the flow of cooling air in a scale laboratory model of an electrical machine using the open-source CFD code OpenFOAM. The comparison between the numerical results obtained using the frozen rotor model and the Particle Image Velocimetry (PIV) measurements showed a good agreement. Hettegger *et al.* (2012) carried out a numerical and experimental investigation on the air flow and heat transfer in the end winding region of a rotating electrical machine. The comparison between numerical and experimental results pointed out that the numerical prediction by Scale-Adaptive Simulation turbulence model were in good agreement with the experimental data only when temperature-dependent fluid properties were used. Recently, Rasekh *et al.* (2015, 2017) presented new correlations to evaluate the convective heat transfer in an axial flux permanent magnet synchronous machine with the aid of CFD simulations. The comparison between the computed results and the available data in literature showed that the proposed correlations accurately predict the heat transfer rates on all surfaces of the machine.

In the majority of CFD studies and heat transfer analysis available in the literature, the fixed temperature or the uniform heat flux boundary conditions were prescribed at the fluid-solid interface to obtain the CHTC distribution. This approach neglected the influence of the heat conduction in the solid on the convective heat transfer, which might reduce the accuracy of the CHTC calculation. An alternative approach is to use the conjugate heat transfer (CHT) method, which refers to a technique that simultaneously solves the fluid flow equations, as well as the energy equations in both solid and fluid domains. The CHT method applied to the thermal analysis of hydro-generator was firstly reported by Shanel *et al.* (2003), which was an extension of a previous CFD study Pickering *et al.* (2001) on the air flow conducted on the same machine. The numerical results performed on a simplified model showed that the CHT method can be used effectively to predict the temperature of the rotor salient poles. However, due to the limited computing resources at the time, the simulations in both studies were performed on coarse meshes and the wall-function model was the unique approach for the boundary layer modelling. Klomberg *et al.* (2015a) numerically investigated the heat transfer in the end winding region of a hydro-generator prototype by using the mixing plane model and the shear stress turbulence model SST. The mesh sensitivity analysis showed that the calculated heat transfer coefficients were the same for the simulations using meshes with a dimensionless near-wall distance $y^+ \approx 1$ or $y^+ \approx 8$. Weili *et al.* (2013) performed a numerical analysis of turbulent fluid flow and heat transfer in the rotor of a 250 MW hydro-generator using the CHT method. The comparison of average temperature of excitation winding between numerical and measured values showed a very good agreement with the error smaller than 1%. Recently, Lancial *et al.* (2017) carried out an investigation on the Taylor-Couette-Poiseuille flow and heat transfer in an annular channel of a slotted rotating inner cylinder found in a salient pole hydro-generator. The comparison of the temperature distribution on the rotor pole face between the numerical values with the CHT method and the experimental values showed a very good agreement.

In recent years, numerous investigations have been undertaken on thermal aspects of hydro-generators. However, there are only few works focusing on the rotor-stator air gap region, where the flow dynamics and heat transfer characteristics significantly contribute to the overall machine performance. Moreover, most of these studies employed the wall-function model

for the near-wall region modelling and the steady state frozen rotor model to avoid numerical instability. For these reasons, a thorough investigation is now carried out to improve the understanding of the fluid flow and heat transfer in this region. The objective of this current work is to study the turbulent convective heat transfer on the salient pole face of a hydro-generator scale model through high resolution CFD computations. In particular, the flow structures in the rotor-stator gap, the effects of different turbulence models, thermal boundary conditions and the physical fluid properties are investigated.

5.2 Experimental setup

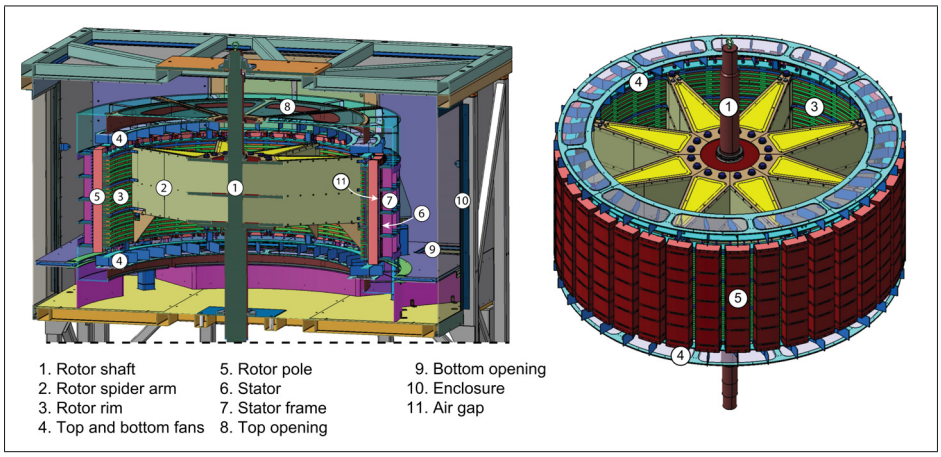

Figure 5.1 Generator scale model.

Because of limited access to actual generators in the power plants, a small-scale rotating model was designed and built at Institut de Recherche d'Hydro-Québec (IREQ) in order to perform flow and thermal measurements. The dimensions are based on the prototype of a hydro-generator currently operating at Hydro-Québec.

As illustrated in Figure 5.1, the scale model is installed inside an enclosure to obtain a closed-loop ventilation circuit. The fluid motion in this model is driven solely by the rotation of the rotor. Indeed, the rotor spider arms act as a centrifugal pump that directs the cooling air through the rotor ventilation ducts and fan blades, then through the air-gap, the stator ducts, and finally the stator frame. To facilitate the visualization of the flow and the PIV measurements, several

components of the scale model are made of transparent material. In order to maintain the fluid dynamics similarity with the prototype of the hydro-generator, the key components such as the air-gap, the rim ducts, and the stator duct are kept the same sizes as the prototype. The global dimensions of the model are scaled down 1:4 in the radial direction and 1:2 in the axial direction and the main parameters are shown in Table 5.1.

In order to study heat transfer phenomena, one of the salient poles was heated using 18 heating elements that were installed inside it. The pole surface temperature was measured by thermistors and a high-frequency pyrometer probe installed in the stator ducts. Afterwards, the temperature distribution in the solid components and the resulting heat flux at the pole surface were calculated with the `ANSYS-CFX` code, using the measured temperature as boundary condition for the outer surface of the heated pole. More information on the experimental setup and the procedure to determine the CHTC can be found in Torriano *et al.* (2014). In the current study, the CHTC data obtained by the experiments were used to validate the values computed by the numerical model.

Parameter	**Dimension**
Rotor diameter	2.270 m
Rotor height	1.040 m
Number of rotor ducts	36×23
Dimension of rotor ducts	23×12.7 mm
Number of poles	36
Stator inner diameter	2.296 m
Stator thickness	4.76 mm
Stator height	0.73 m
Number of stator ducts	72×29
Dimension of stator ducts	43×6 mm
Number of radiator openings	4
Enclosure dimensions	$3.2 \times 3.2 \times 1.8$ m

Table 5.1 Scale model parameters.

5.3 Mathematical and numerical models

5.3.1 Geometry and mesh

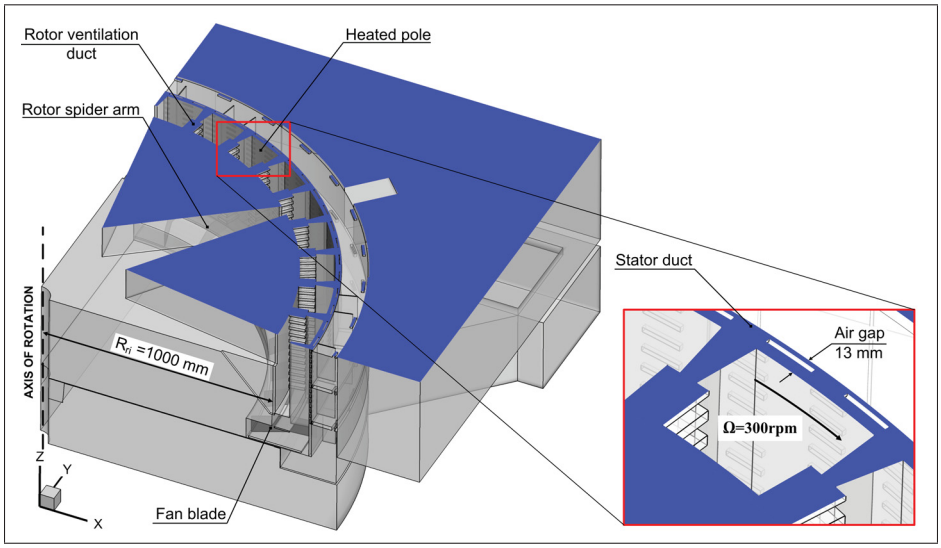

Figure 5.2 Computational domain of scale model with a XY cut plane.

The computational domain of the scale model consists of one sector of 90° exploiting the periodic feature of the setup, and it is illustrated in Figure 5.2 with a XY cut plane to show the internal geometrical features. From a computational perspective, it is not practicable to perform simulations of the full three-dimensional scale model with a very fine mesh, and for this reason, a two steps strategy was used. First, a simulation of the full three-dimensional scale model was performed with a mesh of 86×10^6 hexadral cells using the standard $k-\varepsilon$ turbulence model. This CFD simulation was validated by comparison with the PIV measurement as reported in detail in Bach *et al.* (2015). The numerical results obtained from the first computation were then used to generate the inlet boundary conditions for a second configuration, which was simplified to two inter-pole ducts, as shown in Figure 5.3.

This simplified model comprises a 20° sector for the rotating domain and 5° sector for the stationary domain. Since the rotating and stationary fluid domains are coupled using the mixing plane model, it is possible to use different pitches for these two regions. The rotating domain

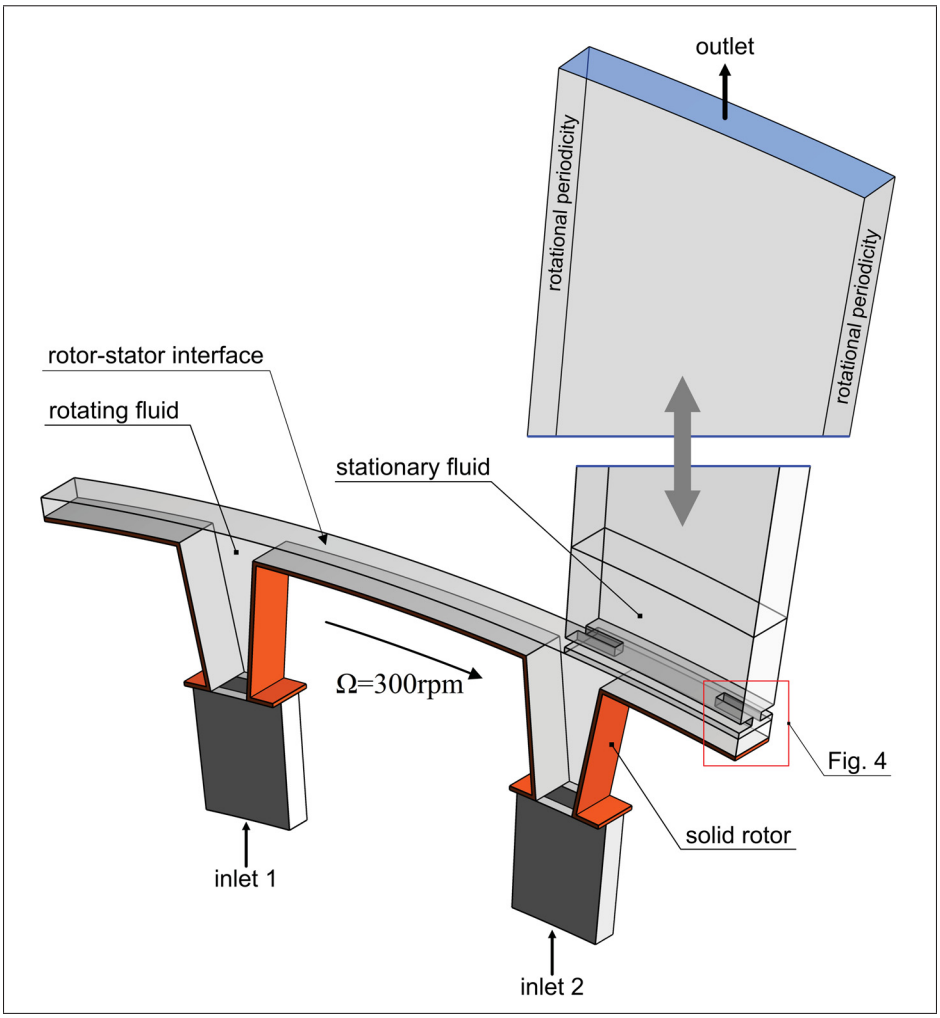

Figure 5.3 Geometry of simplified model.

consists of two inlet boundaries corresponding to the rotor ventilation ducts in the full scale model (zoomed view in Figure 5.2). In the simplified model, the outlet region was extended by 2 m from the rotor-stator interface to reduce the impact of outlet conditions on the flow dynamics in the air-gap.

Hexahedral cells were used to generate the meshes in this study since they are known to introduce smaller truncation errors and to have a better iterative convergence (Blocken *et al.*, 2012). Meshes for rotating, stationary and solid domains were generated separately with the aid of ICEM-CFD and assembled through interfaces within the numerical model. The meshes for each domain are illustrated in Figure 5.4. Appropriate meshes corresponding to the low-Re

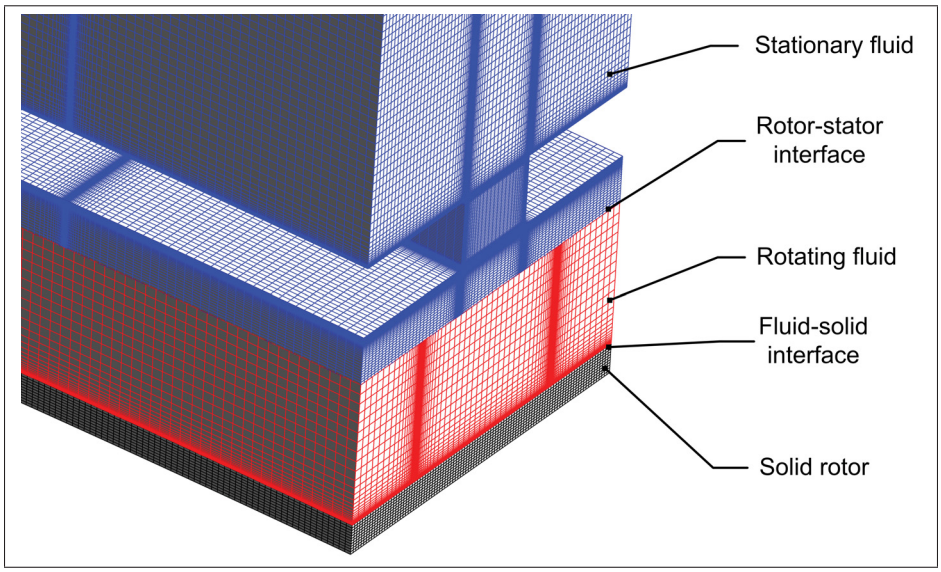

Figure 5.4 Meshes for fluid and solid domains.

model are generated based on a mesh sensitivity study, where the reference mesh has a total of 12×10^6 cells including 9.5×10^6 cells in rotating fluid domain, 0.7×10^6 cells in stationary fluid domain and 1.8×10^6 cells in solid domain. For all meshes, the expansion ratio between two consecutive cells was in range of 1.1-1.2. The wall adjacent cell size is y_P=2.0×10^{-5} m , corresponding to a dimensionless wall distance y^+ below 1 except on the leading side of the pole face, where $y^+ \approx 3$.

5.3.2 Mathematical model

The governing equations for the incompressible, steady-state flow (Ferziger & Peric, 2002) are expressed in the index notation for the rotating frame of reference as follows:

Continuity equation:

$$\frac{\partial}{\partial x_j}\left(\rho U_j\right) = 0 \tag{5.1}$$

Momentum equation:

$$\frac{\partial}{\partial x_j}(\rho U_i U_j) = -\frac{\partial P}{\partial x_i} + \frac{\partial}{\partial x_j}\left[\mu\left(\frac{\partial U_i}{\partial x_j} + \frac{\partial U_j}{\partial x_i}\right) - \rho\overline{u_i u_j}\right] \underbrace{-2\rho\varepsilon_{ijk}\Omega_k U_j}_{Coriolis\ force} \underbrace{-\rho\left[\Omega_j X_j \Omega_i - \Omega_j X_i \Omega_j\right]}_{centrifugal\ force} \tag{5.2}$$

In the rotating frame of reference, the Coriolis and centrifugal forces are taken into account by adding two last terms in the momentum equation. The Boussinnesq eddy-viscosity hypothesis is used to relate the Reynolds stresses to the mean velocity gradients:

$$-\rho\overline{u_i u_j} = \mu_t\left(\frac{\partial U_i}{\partial x_j} + \frac{\partial U_j}{\partial x_i}\right) - \frac{2}{3}\rho k\delta_{ij}, \tag{5.3}$$

where k is turbulence kinetic energy and μ_t is the turbulent viscosity obtained from the turbulence model.

Energy equation:

$$\frac{\partial}{\partial x_j}\left[U_j(\rho E + p)\right] = \frac{\partial}{\partial x_j}\left[\left(\lambda_f + \frac{c_p\mu_t}{Pr_t}\right)\frac{\partial T}{\partial x_j}\right] + \frac{\partial}{\partial x_j}\left(U_i\tau_{ij}^{eff}\right), \tag{5.4}$$

where λ_f is the thermal conductivity of fluid and c_p is the specific heat capacity. The deviatoric stress tensor is given by:

$$\tau_{ij}^{eff} = (\mu + \mu_t)\left(\frac{\partial U_i}{\partial x_j} + \frac{\partial U_j}{\partial x_i}\right) \tag{5.5}$$

The solid heat conduction equation has the same form as the fluid energy equation, i.e. Equation 5.4, except that the velocity components are set to be zero and the solid thermal conductivity λ_s substitutes the equivalent fluid value.

The simulations presented in this study are performed with the CFD software `ANSYS-CFX 16.0`, which uses the control-volume based finite element method (Schneider & Raw, 1987) to discretize the steady RANS governing equations. Several turbulence closure models based on the eddy-viscosity approximation were employed (Equation 5.3), including the standard $k-\varepsilon$ (Jones & Launder, 1973), the Re-Normalisation Group $k-\varepsilon$ (Yakhot *et al.*, 1992), and the SST $k-\omega$ (Menter, 1994) models. These turbulence models belong to the group of two-

equations models: one for the turbulence kinetic energy k and the other for eddy dissipation ε (or frequency ω) (ANSYS, 2015).

5.3.3 Near-wall modelling

Accurate modelling of boundary layer is crucially important for the cases where the prediction of the quantities near the wall, such as friction coefficients or heat transfer coefficients, are needed. A high near-wall resolution is particularly essential for the $\omega-$based turbulence model, i.e. the SST $k-\omega$, since the low-Re number formulation is employed to model the boundary layer. This low-Re number model requires that the dimensionless wall distance, y^+, is close to unity and that the cell growth ratio is around 1.1-1.2. The simulations using $\varepsilon-$based turbulence models employs the wall-function approach to model the boundary layer, which require meshes with $y^+ \approx [30, 300]$, to ensure that the first computational node is located in the logarithmic layer. In the present CFD code, the scalable wall-function enforces that y^+ is not smaller than 11.06, and therefore allows high-resolution meshes to be used for the $\varepsilon-$based models.

5.3.4 Rotor-Stator Interaction

To reduce the computational cost of performing unsteady simulations in a rotor-stator system, two steady-state Multiple Frame of Reference techniques are widely used: the frozen rotor and mixing plane models. A previous study Toussaint *et al.* (2011) showed that the flow field predicted by the frozen rotor model significantly depends on the relative position between rotor and stator, whilst the mixing plane model demonstrates a good agreement with the time-averaged transient model solution. For this reason, all simulations in this current study are performed using the mixing plane model. In this approach, a General Grid Interface (GGI) is defined between the rotor and stator components to couple rotating and stationary domains so that a steady-state solution is calculated (Galpin *et al.*, 1995). The principle of the numerical technique of mixing plane model is that the field variables are calculated in a rotating frame for the rotor and in a stationary frame for the stator domain. The flux-weighted circumferential av-

erages of the conserved variables obtained at the outlet plane of the rotating domain (upstream region) are used to specify boundary condition at the inlet of the stationary domain (downstream region), and vice versa. The interface fluxes across the mixing plane are implemented within the solver such that they are fully implicit, and conservation is maintained across the interface for the fluxes of mass, momentum, total enthalpy, and turbulent quantities. The detail of theory and implementation of the mixing plane model can be found in ANSYS (2015).

5.3.5 Boundary conditions

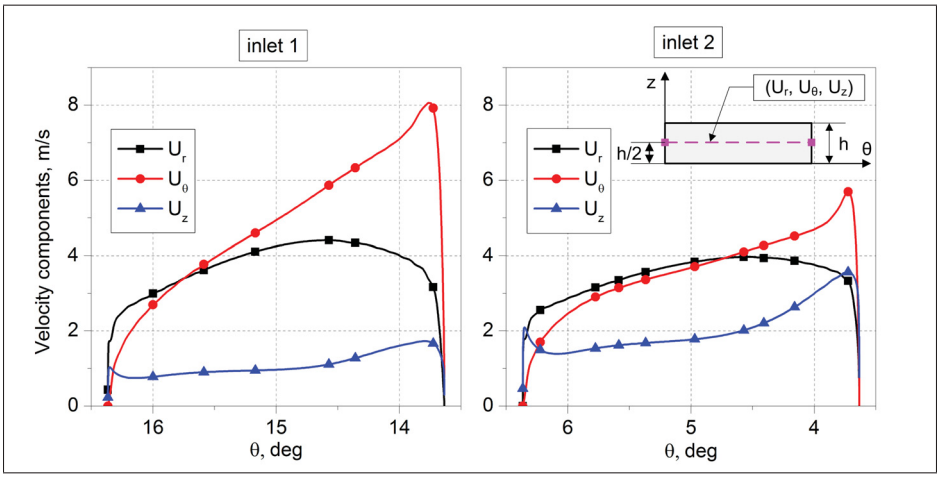

Figure 5.5 Velocity components at the rim ducts inlet boundaries on the mid axial line, i.e., $z = h/2$.

Physical properties	Air	Solid
Density (kg.m^{-3})	1.15	7.85×10^3
Thermal conductivity (W.m^{-1}.K^{-1})	2.61×10^{-2}	6.05×10^1
Specific heat capacity (J.kg^{-1}.K^{-1})	1.0044×10^3	4.34×10^2
Dynamic viscosity (kg.m^{-1}.s^{-1})	1.831×10^{-5}	-

Table 5.2 Physical properties of air and solid.

The inlet boundary condition is specified with the mean velocity, turbulent kinetic energy, and turbulent dissipation profiles extracted from the CFD simulation of three-dimensional full scale model. Typical profiles of the mean velocity components at the inlets are plotted in Figure 5.5.

All the surfaces of the duct, pole, and stator walls are modelled as no-slip boundaries. For the upper and lower XY planes in axial direction, symmetry condition are specified. For each fluid and solid domain, a rotational periodicity is imposed in the circumferential direction. At the outlet, a zero static pressure with blend factor 0.5% is specified (ANSYS, 2015).

In the experimental model, the closed space inside the salient pole is occupied by the stagnant air and each heating element are equipped with an insulating foam on the interior side. Therefore, the heat transfer in the inner surface of the pole is very limited and it can be assumed as an adiabatic boundary. The imposed heat source in the solid is chosen so that the wall temperature at the pole face is close to the experimental model values, i.e., 80°C-90°C. The rotational speed of the rotor is set at a constant value of 300 rpm, corresponding to a local Reynolds number (based on the air gap dimension and the rotor tip velocity) of 2.95×10^4. The dynamic viscosity, the thermal conductivity, and the specific heat capacity are modelled as the temperature-dependent properties using Sutherland's formula (ANSYS, 2015). For the simulations performed with constant physical properties, these parameters are summarized in Table 5.2.

In consideration of the recommendation of ASME guideline on numerical accuracy (ASME, 2009), all governing equations were discretized using second-order accurate schemes in space. The convergence was assessed by monitoring the residual values of flow variables as well as by examining relevant quantities at critical locations. The convergence criteria requires that the maximum residual for all flow variables were below 10^{-4} except for energy and pressure equations, for which the criteria is 10^{-6}. Moreover, the global imbalance of each computational domain are set to be below 1%.

5.4 Results and discussion

5.4.1 Mesh independence study

A mesh sensitivity study was carried out to determine the number of nodes which would result in a mesh independent solution. Here, all simulations were performed using SST $k-\omega$ turbu-

Case	Mesh	Dimensionless wall distance y^+	Number of elements
1	Coarse	1	6.5×10^6
2	Fine	1	12×10^6
3	Fine	5	12×10^6
4	Fine	9	12×10^6
5	Very Fine	1	22.5×10^6

Table 5.3 Computed cases for mesh independence analysis.

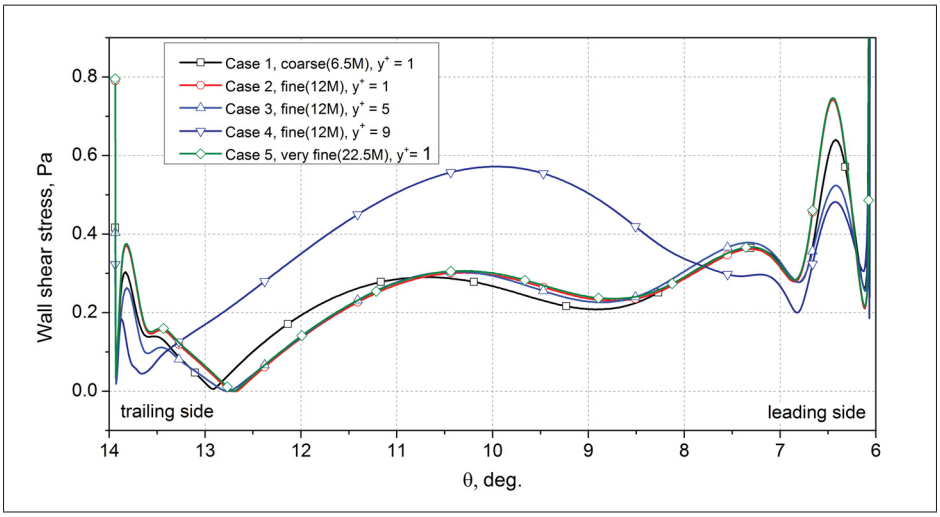

Figure 5.6 Wall shear stress along the pole face for different mesh discretizations.

lence closure and the mixing plane model at the rotor-stator interface. The test cases designed for the mesh independence analysis are shown in Table 5.3, where three levels of mesh density, namely coarse, fine and very fine, were considered. The mesh refinement was taken with respect to the recommendation by ASME V&V 20 guideline (ASME, 2009), which suggests that the average size ratio between consecutive meshes was kept at least 1.3. To evaluate the impact of the mesh resolution on the predictions of quantities near the walls, three levels of the dimensionless wall-distance, y^+, were also taken into account: $y^+ = 1$, 5 and 9. Since the calculation of heat transfer coefficient is strongly dependent on the wall shear stress (Moradnia *et al.*, 2014a,b), this quantity, τ_w, is chosen as an indicator of the mesh quality.

In Figure 5.6, the wall shear stress distribution on the pole face along a line centered in the

axial direction is plotted for each case. It is possible to notice that the results are quite similar for all meshes, except for Case 4. However, the results computed with mesh of Case 1 and Case 3 slightly miss the location of flow separation (i.e., where $\tau_w = 0$) in the downstream region of the pole face. For the mesh of Case 4, the large deviation in the wall shear stress distribution can be explained by the fact that, for a mesh with high dimensionless wall-distance y^+ value, the blending model between the wall-function and low-Re number models was used to solve the boundary layer. Finally, the mesh of Case 2 shows results that are nearly identical to those obtained with the finest mesh (i.e., maximum relative error less than 2%). Thus, a mesh independent solution is obtained with the mesh of 12×10^6 cells having a dimensionless wall distance value $y^+ < 1$. For this reason, the mesh of Case 2 was chosen for all further simulations.

5.4.2 Turbulence model effects

In the modelling of complex flows, the turbulence model is known to have a strong impact on the flow and heat transfer prediction (Howey *et al.*, 2012). In order to select the most appropriate model for the studied configuration, the simulations were performed with several RANS turbulence models, including the standard $k-\varepsilon$ (SKE), the Re-Normalised Group $k-\varepsilon$ (RNG), and Shear Stress Tranport $k-\omega$ (SST).

Figure 5.7 shows the flow pattern on the mid axial plane computed using different turbulence models. As illustrated, all turbulence models produce nearly identical flow patterns in the inter-pole and in the rotor-stator gap regions, except for some minor flow features.

More specifically, in the upstream region of the rim duct, the mean flow is affected by the conditions at the duct entrance. The cooling air enters into the ducts with a high incidence angle, and impinges on the leading side of the duct, as the rotor rotates in the clockwise direction. A low pressure zone with a recirculation bubble is thus formed on the trailing side of the duct. Further downstream, the air flow crosses a forward facing step, accelerates in the duct constriction region and reattaches on the trailing side. On the leading side, a low pressure zone with a large recirculating zone is created. A relatively small recirculation is also predicted by the SST

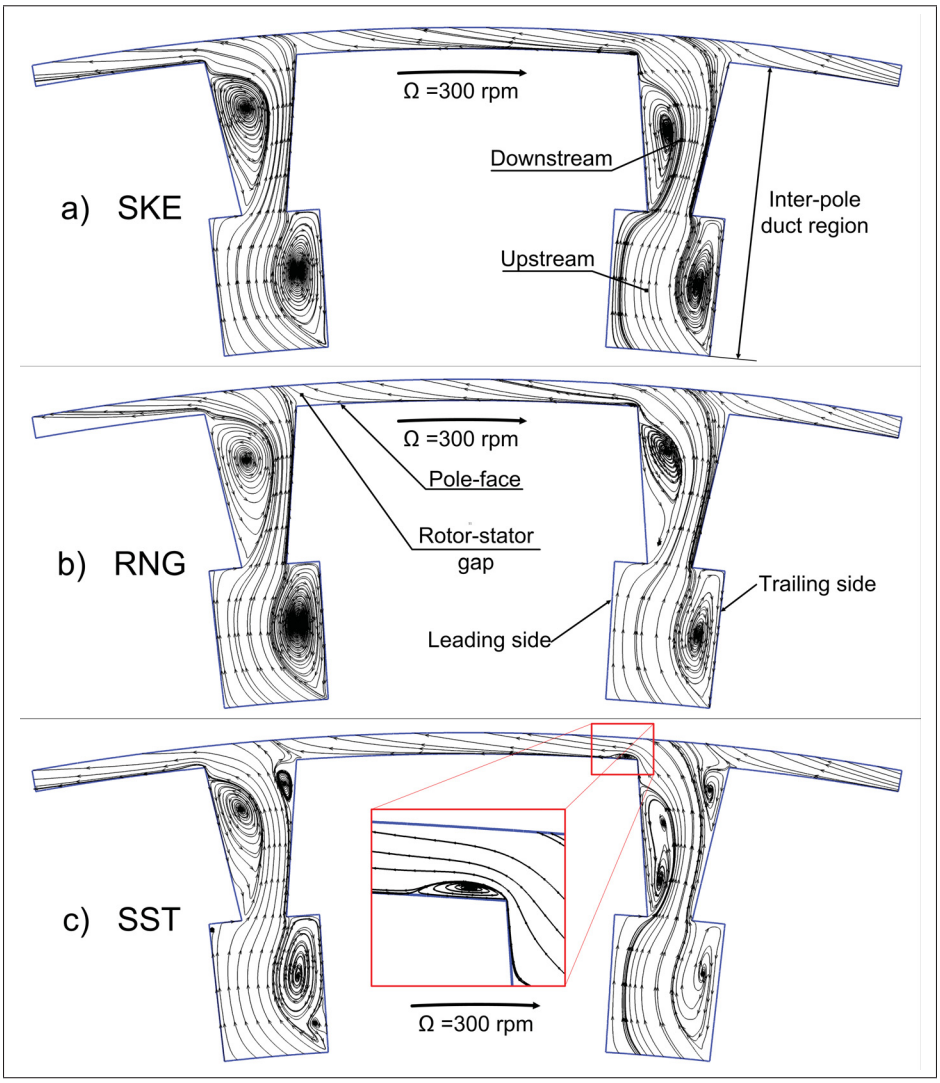

Figure 5.7 Flow structures in the middle (r, θ) plane computed by different turbulence models.

model near the end of the pole trailing edge, but this flow feature is not found in the results computed using the ε-based turbulence models.

At the downstream end of the inter-pole, the flow enters into the rotor-stator gap region under the effect of Coriolis force, and a small recirculation zone is formed near the leading side of rotor tip, as shown in Figure 5.7c.

Furthermore, a complex flow structure consisting of counter-rotating vortex pairs is formed in the air gap, as shown by the streamlines in Figure 5.8. The formation of these vortexes is simi-

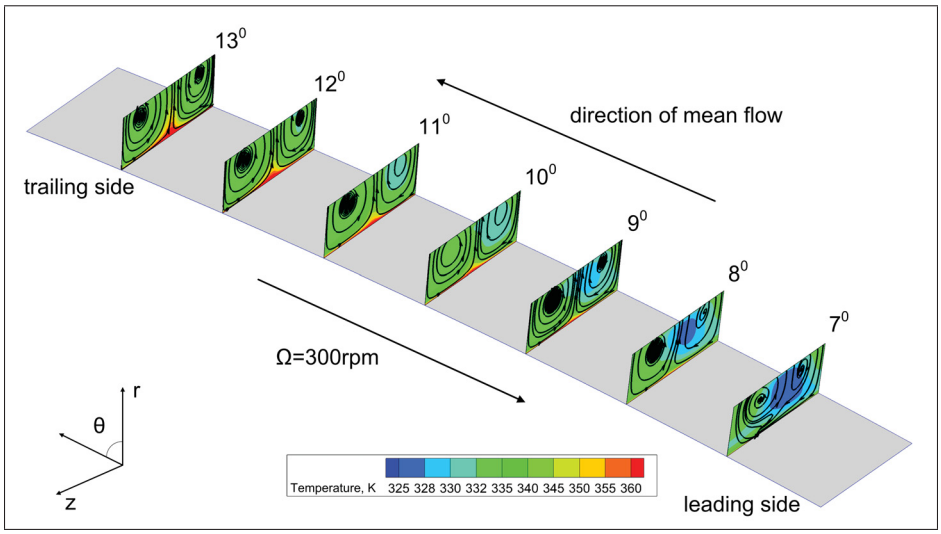

Figure 5.8 Flow structures on $r-z$ planes perpendicular to the pole face predicted by SST $k-\omega$ model.

lar to the one observed with a jet in a cross flow (Lim *et al.*, 2001; Wegner *et al.*, 2004), where the flow exiting from a hole or duct interacts with a cross flow in a the gap region. However, the exact mechanism governing the formation of these counter-rotating vortexes is still a subject of debate, according to Lim *et al.* (2001).

5.4.3 CHTC on pole face

The convective heat transfer on a surface is characterized by convective heat transfer coefficient (CHTC), which is generally defined as:

$$h = \frac{q_w}{T_w - T_{ref}} \tag{5.6}$$

where q_w is the wall heat flux, T_w is the wall temperature, and T_{ref} is the fluid reference temperature. In the present study, CHTC on the pole face is calculated using the reference temperature of the fluid at a distance of 5 mm from the pole surface, in order to be consistent with the experimental study.

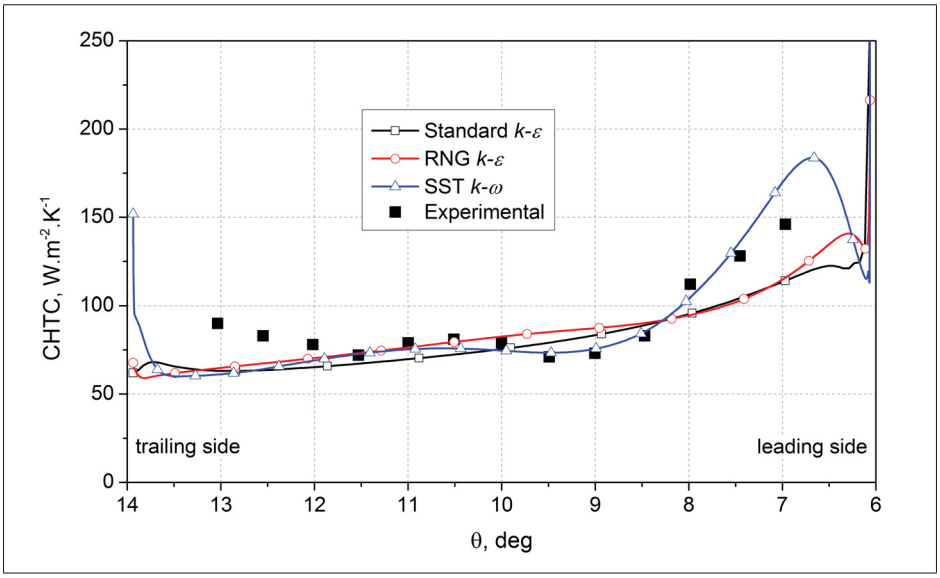

Figure 5.9 CHTC on the pole face predicted by different turbulence models vs. experimental data.

5.4.3.1 Turbulence model effect

Figure 5.9 shows the distribution of CHTC on the pole face computed using different turbulence models as well as the experimental distribution. The experimental data is obtained from Torriano *et al.* (2014), in which the details on the experimental setup and the approach to extract the heat transfer coefficients at the pole face can be found. All turbulence models are able to predict the general trend of CHTC distribution on the pole face and, as expected, higher heat transfer coefficients are found on the leading side of the pole face. However, the results show a discrepancy between the numerical prediction and experimental data, especially in the regions near the leading and trailing sides of the pole face. The maximum relative error of 32% is found in the trailing region of the rotor-stator gap, where a complex flow structure is observed. This feature is partly captured by the SST model, and highlighted by the dashed lines in Figure 5.10c, where the streamlines on a $z-\theta$ plane at a distance of 1 mm from the pole face are plotted. The analysis of the CHTC distribution and of the flow features on the pole face shows that the local minimum of CHTC is found near the core of the recirculation vortex at the leading tip and the local maximum of the CHTC is observed where the flow attachment occurs

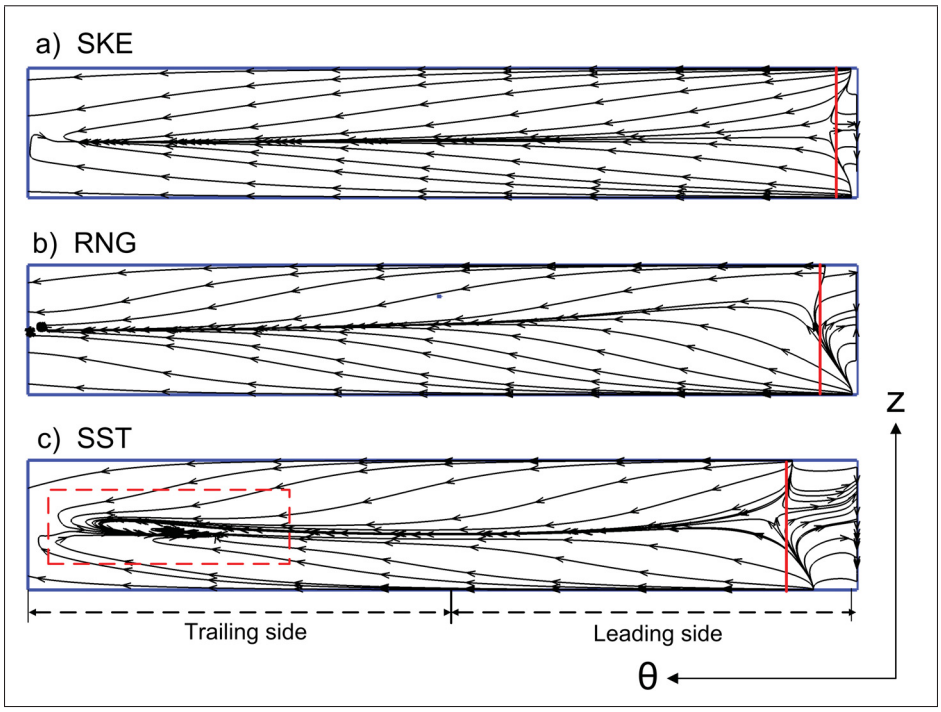

Figure 5.10 Streamlines near the pole face predicted by different turbulence models.

(the positions of flow reattachment are marked with the solid vertical lines in Figure 5.10).

In summary, of the three turbulence models used in this study, the results computed using the SST model show a better agreement with experimental data. This finding is consistent with previously published studies that have shown that the wall-function concept is not sufficiently accurate for modelling the complex flow with separation and reattachment since it was formulated for the wall-attached boundary layer, under local equilibrium conditions.

The discrepancy between numerical and experimental results could be partly explained by the limitation of the numerical models, with respect to the steady-state mixing plane model in combination with the RANS turbulence closures. These models might not be able to capture the unsteady effect in the trailing region of the pole face. It is acknowledged that the accuracy of the convective heat transfer prediction on the pole surface can be improved by using finer modelling techniques, such as URANS (Unsteady RANS) or Large Eddy Simulation turbu-

lence model accompanied with the transient rotor-stator interface. However, these approaches require high computational resources, and are out of the scope of this study.

5.4.3.2 Near-wall model effect

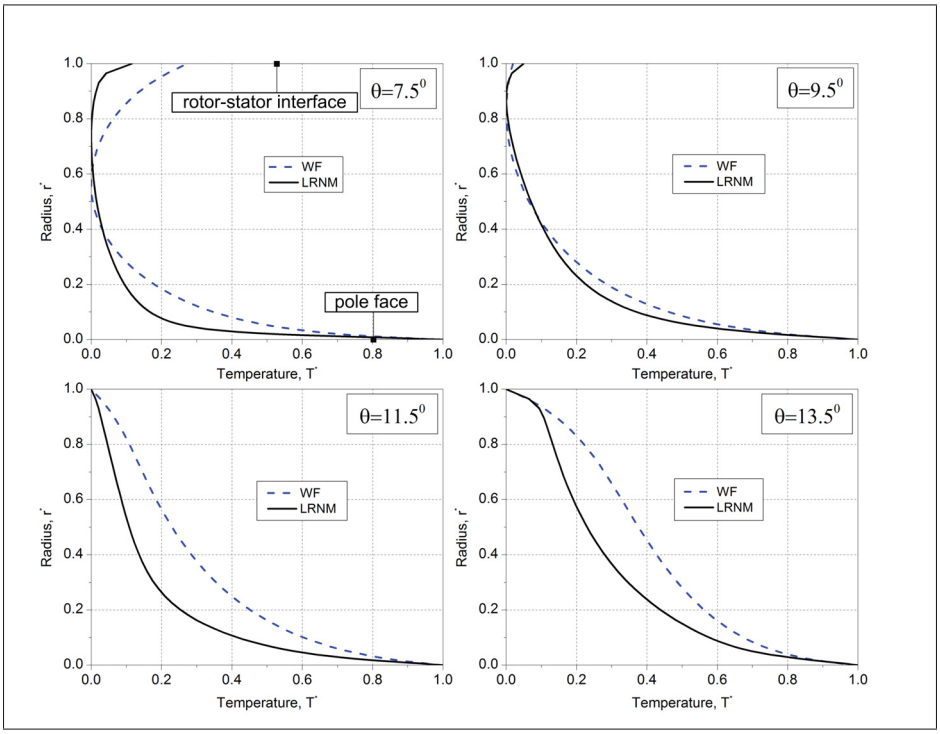

Figure 5.11 Temperature profiles along the lines normal to the pole face predicted by WF and LRNM.

In Figure 5.11, temperature profiles T^* along the radial lines computed using the wall-function (WF) and low-Re number model (LRNM) are presented. The data show that the LRNM predicts a higher temperature gradient near the wall than the WF model. However, as shown in Figure 5.12 the turbulent kinetic energy values calculated by the WF model are higher than those obtained from the LRNM model. The resulting effect of these two opposite trends is a similar prediction of CHTC on the pole face by both models, as it was shown in Figure 5.9. In fact, the wall heat flux used to calculate the heat transfer coefficient is proportional to the effective thermal conductivity ($\lambda_{eff} = \lambda_f + c_p \mu_t / Pr_t$), and the temperature gradient evaluated

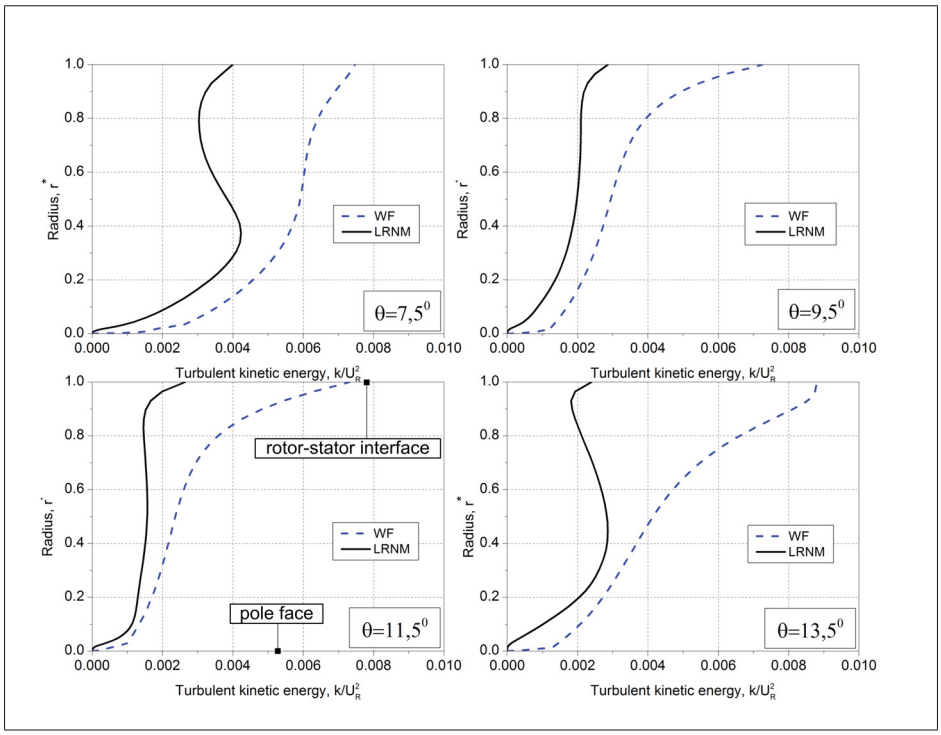

Figure 5.12 Turbulent kinetic energy profiles along the lines normal to the pole face predicted by WF and LRNM.

at the solid surface:

$$q_w \approx \lambda_{eff} \left. \frac{\partial T}{\partial r} \right|_{r=r_{surface}} \tag{5.7}$$

In summary, although the wall-function model is not recommended for cases involving convective heat transfer, it performed quite well for the current configuration, since it was able to capture the general trend of CHTC on the pole face and in average showed a relatively good agreement with experimental data.

5.4.3.3 Thermal boundary conditions and fluid properties effects

In addition to the turbulence model effects, another factor that significantly influences the accuracy of the convective heat transfer predictions is the thermal boundary condition at the fluid-solid interface. In the previous studies in the literature, to obtain the thermal field for the convective heat transfer analysis, either a fixed temperature, a uniform heat flux, or a con-

Case	Thermal boundary condition	Fluid properties
1	Uniform heat flux	Constant
2	Conjugate heat transfer	Constant
3	Conjugate heat transfer	Temperature-dependent

Table 5.4 Thermal boundary conditions.

vective heat transfer coefficient was specified at the fluid-solid interface. However, in reality none of these boundary conditions accurately represents the coupled nature of the conductive-convective heat transfer phenomenon. At this interface, the continuity of temperature and the balance of heat flux must be satisfied, which refers to the conjugate conduction-convection method.

In this section, the comparison between the results obtained by the pure convective heat transfer using the uniform heat flux (Case 2 in Table 5.4) and by the conjugate heat transfer models (Case 3) is presented.

The plot of Figure 5.13 shows the heat transfer coefficient distribution obtained along a line in the mid-plane of the pole face using the two approaches for the fluid-solid interface. The CHTC computed by the pure convective model (Case 1) is slightly lower in the trailing side region but significantly deviates from the conjugate model values (Case 2) in the leading side region. A direct comparison between these two cases under the form of relative error (i.e., $|h_{conv} - h_{conj}|/h_{conj}$) shows that the maximum difference of 14% is found in the leading region of the pole face.

In the CFD simulations presented so far, the fluid properties were kept constant. However, in reality, the fluid properties generally vary depending on the operating conditions of the machine. To verify this effect, the CHTC distributions along the pole face computed using the conjugate heat transfer method with constant (Case 2) and with temperature-dependent air properties (Case 3) are also presented in Figure 5.13. The results shows that the CHTC computed using constant fluid properties are slightly over-estimated in the leading side and under-estimated in the trailing side region of the pole face. In general, the use of air properties that are temperature dependent improves the results in terms of profile trend. Quantitatively,

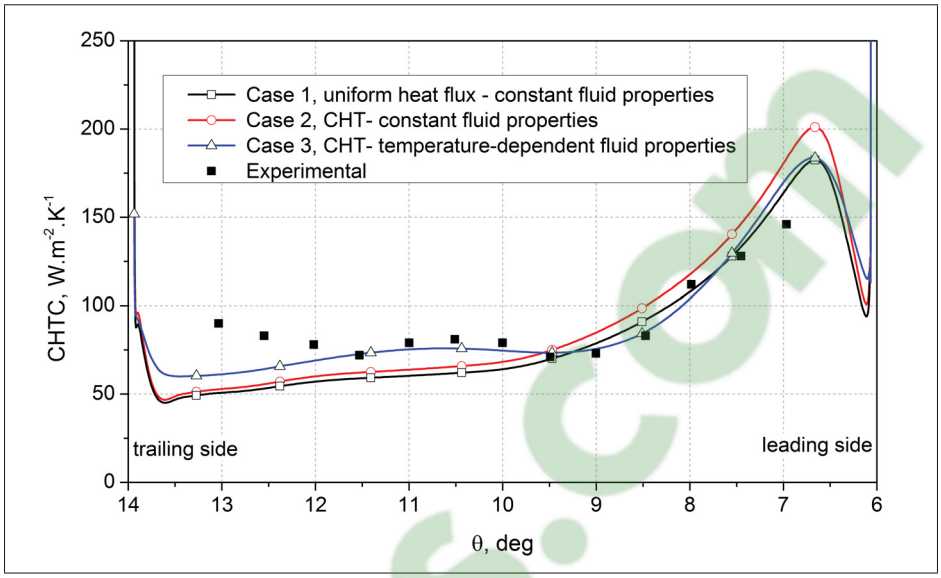

Figure 5.13 CHTC on the pole face predicted by different thermal boundary conditions and air properties types.

the relative difference between the two cases was found to be approximately 25%.

In summary, even with a CHT model with varying fluid properties, a certain discrepancy with the experimental data is observed, especially near the trailing side of the pole face. This discrepancy is related to the limitations of the numerical models used, such as turbulence modelling and the mixing plane model, as well as the limitation of the simplified geometry, i.e., the axial section of a 20° circumferential sector of the scale model, used to perform the simulations.

5.5 Conclusions

This paper has focused on CFD analysis of the turbulent convective heat transfer in the air-gap of a rotor-stator system normally found in a hydro-generator prototype. The numerical simulations were performed using the RANS turbulence closures combined with the steady-state Multiple Frames of Reference mixing plane model at the rotor-stator interface. In order to better represent the coupled nature of the heat transfer at the fluid-solid interface, the conjugate heat transfer was employed. From the results and discussions, the following conclusions can be drawn for the configuration studied here:

- Regarding the mesh sensitivity analysis, to obtain a mesh independent solution, the mesh for the low-Re model should have at least 12M cells with a requirement on the dimensionless near-wall distance, $y^+ < 1$. However, a mesh with $y^+ \approx 5$ can be used for quantitative prediction of the CHTC as it generally captured the trend of the CHTC and showed a relatively good agreement with the reference case.
- The calculations of CHTC on the pole face using different RANS turbulence models show that the best agreement with experimental data was obtained with the SST $k-\omega$ model. However, there still was a certain discrepancy between the numerical results and experimental data, especially in the trailing side region of the pole face. Although the wall-function concept was not expected to perform well for the convective heat transfer calculations, the results computed in this study pointed out that it can be used for predicting the CHTC.
- The thermal boundary conditions at the fluid-solid interface and the use of temperature-dependent fluid properties have an impact on the accuracy of the convective heat transfer calculation. The use of the conjugate heat transfer method with the temperature-dependent fluid properties shows a better agreement with the experimental data.

In the present study, the numerical simulations were performed on a configuration with only one section of the pole in the axial direction and a sector of 20° in the circumferential direction. The effects of imposing the symmetry boundary conditions in the axial directions are apparent. In the future, to improve the CHTC predictions at the pole face, the simulations will be carried out on the full three-dimensional geometry of the pole and the computed temperature on the pole surface will be compared with the measured values (Torriano *et al.*, 2014).

CHAPTER 6

FLUID FLOW AND HEAT TRANSFER PREDICTION IN THE AIR-GAP OF A ROTOR-STATOR SYSTEM: EFFECTS OF NUMERICAL MODELS

D.-D. Dang [1], X.-T. Pham[1], C.-C. Nguyen [1]

[1] Department of Mechanical Engineering, École de Technologie Supérieure,
1100 Notre-Dame Ouest, Montréal, Québec, Canada H3C 1K3

Article submitted to «Journal of Thermal Science»,
in July, 2018.

Abstract

This study is dedicated to a numerical investigation of convective heat transfer on the rotor surfaces of a rotor-stator configuration that is typically found in large hydro-generators. The computational fluid dynamics calculations with two turbulence modeling approaches are used to predict the flow structure and heat transfer in the air gap of the rotor-stator configuration. The steady state mixing plane approach is employed at the interface to couple the rotor and stator components. Results show that the location of mixing plane interface in the air gap plays an important role in the prediction of heat transfer on the pole face. Also, it is indicated that the prediction of temperature distribution on the pole face is greatly affected by the turbulence models used. Furthermore, through a comparison between the pure convective and conjugate heat transfer methodologies, it is shown that the inclusion of solid domain into the numerical model significantly improves the thermal prediction of the solid components of the machine.
Keywords: hydro-generator, rotor-stator system, thermal analysis, conjugate heat transfer, Computational Fluid Dynamics.

Nomenclature

Latin symbols

Bi	Biot number
c_p	Specific heat capacity ($\mathrm{J{\cdot}kg^{-1}{\cdot}K^{-1}}$)
E	Total energy (J)
h	Width of computational domain in the axial direction (m)
P	Time-averaged pressure ($\mathrm{kg{\cdot}m^{-1}{\cdot}s^{-2}}$)
Pr_t	Turbulent Prandtl number
q_w	Wall heat flux ($\mathrm{W{\cdot}m^{-2}}$)
Re	Dimensionless Reynolds number
r	Radius (m)
r^*	Normalized radius $= (r - r_{min})/(r_{max} - r_{min})$
T	Temperature (K)
$\mathbf{U}$	Mean velocity vector ($\mathrm{m \cdot s^{-1}}$)
$\mathbf{r}$	Position vector (m)
y^+	Dimensionless wall distance

Greek symbols

ε	Turbulent kinetic energy dissipation rate ($\mathrm{m^2{\cdot}s^{-3}}$)
θ	Angular coordinate ($^\circ$)
ρ	Density ($\mathrm{kg{\cdot}m^{-3}}$)
ω	Specific dissipation rate (s^{-1})
Ω	Rotational speed ($\mathrm{rad{\cdot}s^{-1}}$)
λ	Thermal conductivity ($\mathrm{W{\cdot}m^{-1}{\cdot}K^{-1}}$)
μ	Molecular dynamic viscosity ($\mathrm{kg{\cdot}m^{-1}{\cdot}s^{-1}}$)
μ_t	Turbulent dynamic viscosity ($\mathrm{kg{\cdot}m^{-1}{\cdot}s^{-1}}$)
τ_w	Wall shear stress ($\mathrm{kg{\cdot}m^{-1}{\cdot}s^{-2}}$)

Subscript

f	fluid
max	maximum
min	minimum
ref	reference
s	solid
t	turbulent
w	wall

Abbreviation

CFD	Computational Fluid Dynamics
CHT	Conjugate Heat Transfer
CHTC	Convective Heat Transfer Coefficient
IREQ	Institut de Recherche d'Hydro-Quebec
MFR	Multiple Frames of References
PIV	Particle Image Velocimetry
RANS	Reynolds-Averaged Navier-Stokes
RNG	ReNormalization Group
RSI	Rotor-Stator Interface
SST	Shear Stress Transport

6.1 Introduction

In the energy conversion process, hydro-generators produce the power losses that cause a temperature rise in the solid components of the machine. The extremely high temperatures in the solid parts might lead to a reduction of the lifetime of the hydro-generator or cause severe failures due to the breakdown of the thermally-limited winding insulation (Traxler-Samek *et al.*, 2010a). In order to prevent any overheating and maintain the internal temperature within a safety margin, hydro-generators are equipped with a cooling system, which provides a flow to evacuate the heat via forced convection. Thus, detailed knowledge of convective heat transfer is of great importance for the design and power upgrade of hydro-generators (Howey *et al.*, 2011).

Although the field of computational fluid dynamics (CFD) has progressed over the past few decades and has been intensively used in the turbomachinery applications, it has been applied less for the design of rotating electrical machines. Apart from traditional issues such as turbulence modelling or numerical scheme, the use of CFD for these applications has the additional challenge of handling the rotating and stationary components. Indeed, the relative motion between these components induces an unsteady rotor-stator flow interaction that is difficult to capture with the numerical model. However, an investigation on a rotor-stator configuration of radial flow carried out by Toussaint *et al.* (2011) revealed that the velocity profiles predicted by the frozen rotor model were extremely sensitive to the position of the rotor relatively to the stator, whereas the mixing plane produced results that match with the time-averaged transient reference solution. In the mixing plane model, a circumferential averaging is performed at the rotor-stator interface, which results in a discontinuity of flow field through the interface (Stein *et al.*, 2015). Due to this characteristic of the mixing plane model, the location of the rotor-stator interface has a significant impact on the flow field prediction. Nevertheless, this effect has not been thoroughly addressed in the literature.

The effects of solid heat conduction on the thermal performance prediction also need to be taken into account. In the majority of studies in the literature, the heat transfer coefficient was always considered as an invariant descriptor of convection phenomenon with respect to the

thermal boundary conditions (Moffat, 1998). In order to obtain the convective heat transfer coefficient (CHTC) distribution, a pure convective heat transfer approach was thus often used, in which either a uniform temperature or heat flux was often specified on the boundary between the fluid and solid domains (Pickering *et al.*, 2002, 2001; Hettegger *et al.*, 2012; Moradnia *et al.*, 2014b,a; Schrittwieser *et al.*, 2014; Jamshidi *et al.*, 2015). This approach, however, neglects the effect of solid heat conduction, which might lead to inaccurate solid temperature calculation. In the alternative *conjugate heat transfer* (CHT) formulation, the fluid dynamics governing equations are coupled with the solid heat conduction in a single module, which offers a better representation of physics insight. The CHT methodology has been actively adopted in recent studies to predict the solid temperatures of hydro-generators (Shanel *et al.*, 2003; Weili *et al.*, 2013; Klomberg *et al.*, 2015a,b; Lancial *et al.*, 2017). In these studies, it was emphasized that the solid heat conduction must be included in the numerical model to produce a more realistic thermal model.

Although the salient pole face of the hydro-generator is a critical location that must be effectively cooled during operation, there are relatively few papers published on the airflow and heat transfer of the air-gap region in the literature. The main reason is that is quite challenging to perform measurements on a rotating machinery within geometrically complex environment in order to obtain a full description of the mean flow and turbulent fields in the air gap region. As a consequence, the numerical approach, where CFD simulations are employed, became a valuable alternative to predict the flow structure and thermal features in the rotor-stator system, as reported in Dang *et al.* (2018). In this study, the effects of the rotor-stator interface location on the thermal prediction on the pole surface are investigated. In addition, through a comparison of solid temperature calculated with the conjugate and pure convective heat transfer methodologies, the impact of the thermal boundary conditions on the solid temperature prediction is analyzed.

6.2 Numerical models

6.2.1 Research context

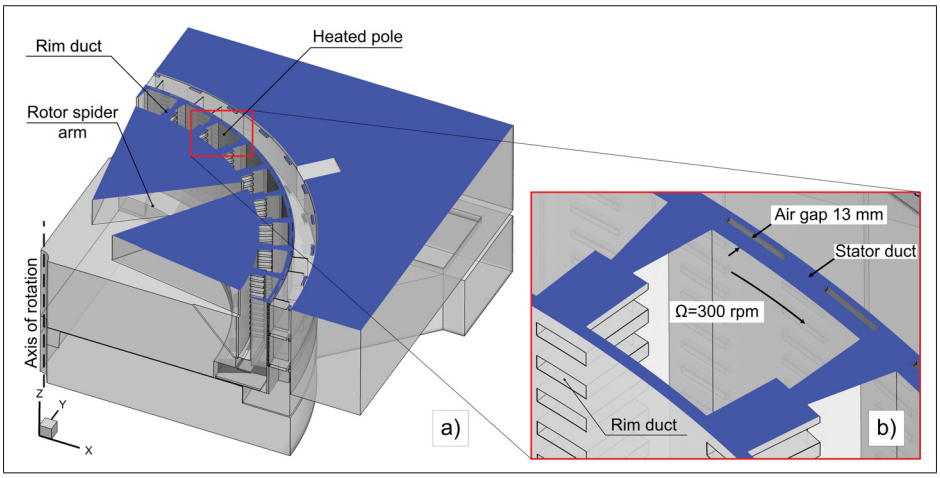

Figure 6.1 Schematic illustration of (a) the computational domain of the experimental model with an axially cutting plane and (b) local region investigated by simplified model (Dang *et al.*, 2018).

In order to gain a better understanding on the ventilation in hydro-generators, a rotating scale model was built at the Institut de recherche d'Hydro-Québec (Torriano *et al.*, 2014). Particle image velocimetry (PIV) measurements have been recently carried out to characterize the ventilation airflow in the full scale model, and they are presented in papers by Bach *et al.* (2015) and Venne *et al.* (2016). CFD simulations were also performed to predict the air flow in the rotating scale model, and they were performed on a 90° sector domain exploiting the periodicity feature of the geometry, as illustrated in Figure 6.1a. Since the geometry of the rotating scale model is characterized by a large variation of characteristic length from the rotor diameter to the narrow air gap, the fluid flow analysis in this model presents a particular challenge for CFD calculations. In addition, numerical results can be affected by a wide range of parameters that cannot be evaluated through simulations on the full scale model due to the high computational cost. Therefore, in order to investigate the fluid flow and heat transfer within the whole domain of full scale model, the numerical analysis only focuses on the region shown in Figure 6.1b.

The area represents a simplified version of the rotor-stator system found in the full scale model. In order to specify the boundary conditions at the inlet of the simplified model, the mean flow and turbulent profiles were then extracted from the CFD results performed on the full scale model in Toussaint *et al.* (2011). For the details of this simplification, it is recommended to read Dang *et al.* (2018). In the context of this study, the same methodology is used and the main features of the simplified model are also described in the next paragraphs.

6.2.2 Simplified geometry and grids

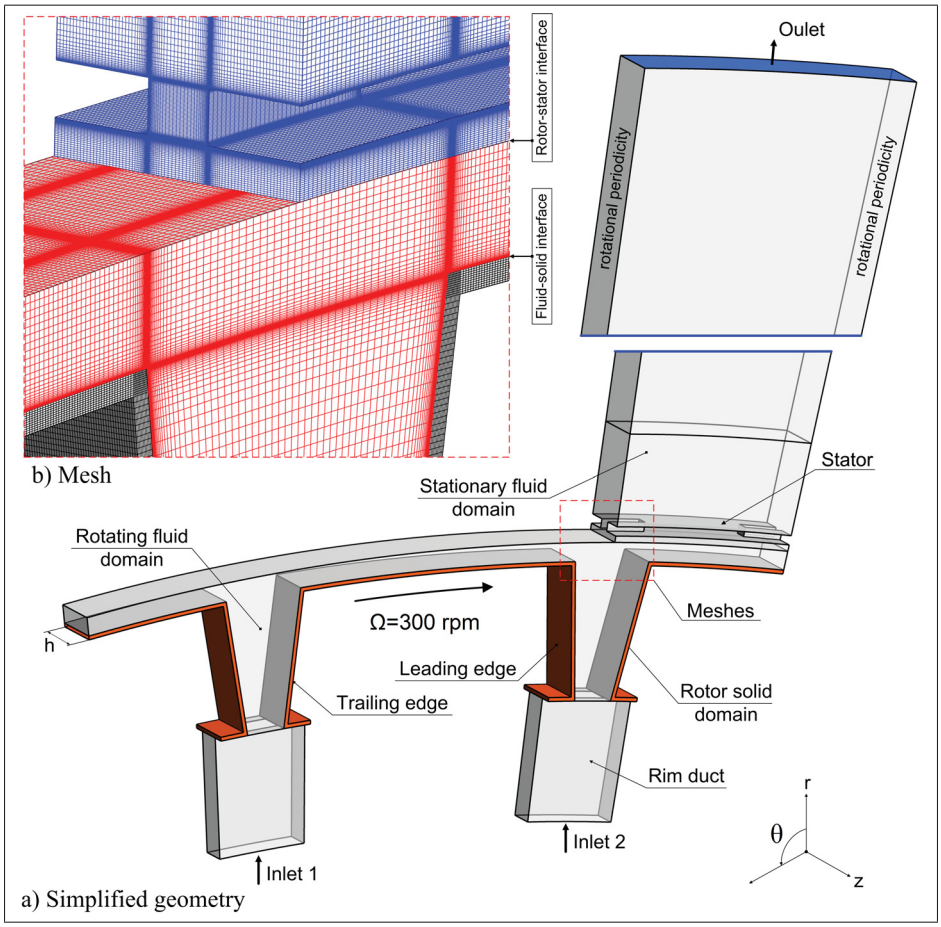

Figure 6.2 Numerical model (a) computational domain of simplified model and (b) mesh.

In Figure 6.2a, the simplified rotor-stator configuration is schematically illustrated. It is composed of 20° sectors in the rotating fluid domain and the solid domain, and a 5° sector in the stationary fluid domain. In this simplified model, two inlet boundaries are included to represent the corresponding rim ducts in the experimental model, as illustrated locally in Figure 6.1b. In order to eliminate the influence of conditions at the outlet to the prediction in the air-gap region, this boundary is located at a distance of 2 *m* from the stator wall.

The rotating fluid, the stationary fluid, and the rotor solid domains were meshed separately using the meshing tool ANSYS ICEM, as shown in Figure 2b. These unstructured meshes were connected within the solver using relevant interfaces, i.e. the rotor-stator interface and the fluid-solid interface. Hexahedral elements were used to generate the mesh in order to reduce the truncation error and obtain a better convergence. Based on a grid independence analysis, the optimal mesh includes a total of 12 $\times 10^6$ nodes, with approximately 9.5×10^6 nodes in the rotating domain, 0.7×10^6 nodes in the stationary domain, and 1.8×10^6 nodes in the rotor solid domain. In order to accurately predict the flow field in the near wall region, the average dimensionless wall distance y^+ values were kept lower than 1 for the pole face, and lower than 3 for the leading and trailing edges.

6.2.3 Governing equations

All simulations in this work are carried out using the commercial CFD code `ANSYS CFX 17.0`, in which the governing equations are discretized by the control-volume based finite element method (Schneider & Raw, 1987). The Reynolds-averaged Navier-Stokes (RANS) equations, including the continuity (Equation 6.1), the momentum (Equation 6.2) and the energy (Equation 6.3) equations, are given for the incompressible, steady flows (Ferziger & Peric, 2002) in the rotating frame as follows:

$$\nabla \cdot \mathbf{U} = 0 \tag{6.1}$$

$$\rho \nabla \cdot (\mathbf{U} \otimes \mathbf{U}) = -\nabla p + \nabla \cdot \tau - 2\rho\Omega \times \mathbf{U} - \rho\Omega \times \Omega \times \mathbf{r} \tag{6.2}$$

$$\nabla \cdot [\mathbf{U}(\rho E + p)] = \nabla \cdot \left[\left(\lambda_f + \frac{c_{pf}\mu_t}{Pr_t} \right) \nabla T \right] + \nabla \cdot (\mathbf{U}.\tau) \tag{6.3}$$

where $\mathbf{U}$ is the mean velocity vector, p is the pressure, λ_f is the thermal conductivity, c_{pf} is the specific heat capacity, and Pr_t is the turbulent Prandtl number. The two last terms in the momentum equation are included to account for the Coriolis and centrifugal forces, in which Ω and $\mathbf{r}$ are rotational speed and the position vector, respectively. The effective shear stress tensor, τ, is given as:

$$\tau = \mu_{eff}\left(\nabla\mathbf{U} + \nabla^T\mathbf{U}\right) \tag{6.4}$$

where μ_{eff} is the effective viscosity, defined as sum of the molecular and turbulent eddy viscosity, $\mu_{eff} = \mu + \mu_t$.

For the conjugate heat transfer cases, the fluid dynamics equations are simultaneously solved with the heat conduction in solid domain (Equation 6.5) with additional constraints on the continuity of temperature (Equation 6.6) and the equilibrium of heat flux (Equation 6.7) at the fluid-solid interface Γ:

$$\nabla\cdot(\lambda_s\nabla T) + Q = 0 \tag{6.5}$$

$$T_f\big|_\Gamma = T_s\big|_\Gamma \tag{6.6}$$

$$(\lambda_s\nabla T_s.\mathbf{n})\big|_\Gamma = \left(\lambda_f\nabla T_f.\mathbf{n}\right)\big|_\Gamma \tag{6.7}$$

where λ_s is the solid thermal conductivity and Q is the volumetric heat source.

The turbulent eddy viscosity μ_t was calculated using two turbulence closure models based on the Boussinesq assumption: the standard $k-\varepsilon$ (Jones & Launder, 1973) and Shear Stress Transport (SST) $k-\omega$ (Menter, 1994). In order to model the boundary layer, the standard $k-\varepsilon$ uses the `CFX` scalable wall functions model, while the SST $k-\omega$ employs the automatic wall treatment formulation (ANSYS, 2015).

6.2.4 Boundary conditions and convergence criteria

At the inlet boundaries, the profiles of mean and turbulent fields generated from the numerical results on the full scale model are imposed. As an example, the radial velocity and turbulent kinetic energy contours at these two boundaries are given in Figure 6.3. The no-slip bound-

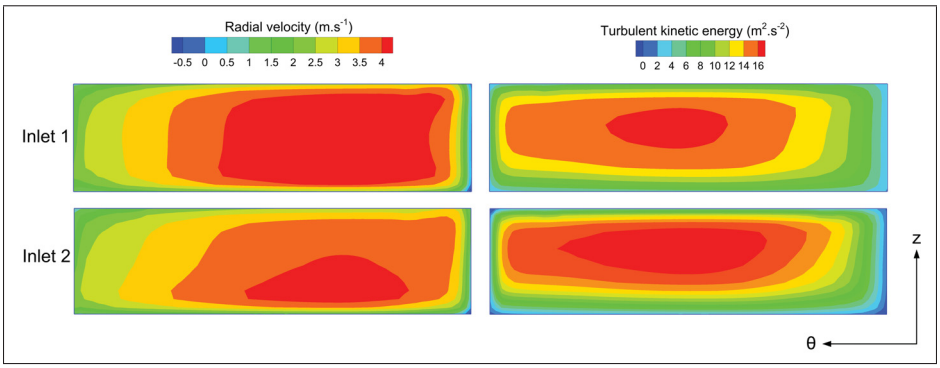

Figure 6.3 Radial velocity and turbulent kinetic energy contours at inlet boundaries.

ary conditions are specified on the rotor rim ducts walls, the surfaces of rotor pole, and stator wall. The outlet boundary is specified using a zero static pressure with a blending factor of 0.5% (ANSYS, 2015). At the lower and upper XY planes of each fluid and the solid domains, symmetry boundary conditions are defined. In the circumferential direction of rotating and stationary fluid and solid rotor domains, periodic boundary conditions are applied. Since the inner surface of the heating pads is coated with an insulating foam and it comes into contact with stagnant air inside the salient pole; the heat transfer on this surface is restricted. Therefore, the inner side of the pole surface is specified as the adiabatic boundary. In the solid domain, the volumetric heat source was defined in order that the temperature values on the pole surface be similar with the measured ones in Torriano *et al.* (2014), those are in the range of 80°-90°C. The rotor part of this system is imposed with a rotational speed of 300 rpm, for which the Reynolds number is of 2.95×10^4. The main properties of fluid, including the the specific heat capacity, the dynamic viscosity, and the thermal conductivity, are used as temperature dependent properties (Klomberg *et al.*, 2015b). For calculations carried out with the unchanging fluid properties, these values are given in Table 6.1.

At the rotor-stator interface, the mixing plane model was defined to couple the rotor and stator parts. In this interface model, the conserved flow variables are first circumferentially averaged at the exit of the rotating domain and then utilized to specify as the boundary condition at the entry of the stationary domain, and vice versa. Owing to this averaging, different angle pitches

Physical properties	Air	Solid
Density ($kg.m^{-3}$)	1.15	7.85×10^3
Thermal conductivity ($W.m^{-1}.K^{-1}$)	2.61×10^{-2}	6.05×10^1
Specific heat capacity ($J.kg^{-1}.K^{-1}$)	1.0044×10^3	4.34×10^2
Dynamic viscosity ($kg.m^{-1}.s^{-1}$)	1.831×10^{-5}	-

Table 6.1 Physical properties of fluid and solid used in the study.

can be used for the rotating and stationary domains, as illustrated above in the simplified model section. For the details on numerical treatment and characteristics of the mixing plane interface model, it is recommended to read Galpin *et al.* (1995); Stein *et al.* (2015); Bourgeois *et al.* (2011).

The convergence was assessed by examining residuals of flow variables as well as by monitoring the variation of relevant quantities at specific locations in the flow field. The convergence criteria were that the maximum residuals should be less than 10^{-4} for all flow variables excluding the energy equation, for which the criteria was 10^{-6}. In addition to monitoring residuals and variation of flow quantities, the global conservation in each domain was also checked, by allowing a maximum imbalance of 1% for flow and thermal variables.

6.2.5 Data reduction

In this study, the performance of the rotor-stator system is identified by the convective heat transfer on the pole face and the total windage loss in the rotating domain. These parameters are used as indicators to evaluate the sensitivity of numerical models and are defined as follows:

- The *convective heat transfer coefficient* is used to quantify the heat transfer characteristics:

$$\mathrm{CHTC} = \frac{q_w}{T_w - T_{ref}} \tag{6.8}$$

where q_w is the wall heat flux, T_w and T_{ref} are the wall temperature and reference temperature, respectively.

- The *total windage power loss* $P_{windage}$ within a control volume bounded by a control surface S is calculated from Toussaint *et al.* (2011), which is derived from the energy balance principle:

$$\left[\frac{1}{\rho}\int_S P_{tot}d\dot{m}\right]_{in} - \left[\frac{1}{\rho}\int_S P_{tot}d\dot{m}\right]_{out} + T_{rotor}\cdot\Omega - P_{windage} = 0 \tag{6.9}$$

  where two first terms in this equation represent the net work rate done by the total pressure, P_{tot}, on the control surfaces, and T_{rotor} is the total torque on a surface S.
- The average of any quantity ϕ, such as the CHTC or the wall shear stress, over the control surface S is computed as:

$$\overline{\phi} = \frac{\int_S \phi dS}{\int_S dS} \tag{6.10}$$

6.3 Results and discussion

6.3.1 Grid independence analysis

Parameters	Values
$N_{M_1}, N_{M_2}, N_{M_3}$	25×10^6, 12×10^6, 5.4×10^6
ϕ_1	0.26238
ϕ_2	0.26049
ϕ_3	0.25725
p	1.1831
$e^{21}_{ext}(\%)$	1.3248
$e^{21}_{a}(\%)$	0.7203
$GCI^{21}_{fine}(\%)$	1.6560
$GCI^{32}_{med}(\%)$	2.5750

Table 6.2 GCI calculation result.

In order to determine the optimal mesh size used in the numerical model, a mesh independence study was undertaken on three meshes with different resolutions. To estimate the discretization error, the Grid Convergence Index (GCI) method (gci, 2008) was selected. Since the prediction of the convective heat transfer is tightly connected to the wall shear stress estimation (Moradnia *et al.*, 2014a), the average value of this parameter on the pole face, $\overline{\tau_w}$, was used to evaluate

GCI values. The results of GCI calculation are presented in Table 6.2, where ϕ_i (in Pa) denotes the value of $\overline{\tau_w}$ calculated on the mesh M_i with number of nodes N_{M_i} $(i = 1,2,3)$. Also in this table, the apparent order p, the extrapolated relative error e_{ext}^{21} and the approximate relative error e_a^{21} are reported. According to data in Table 6.2, the GCI values decrease with the mesh refinement, i.e. $GCI_{fine}^{21} < GCI_{med}^{32}$, which indicates that the mesh independent solution has been obtained (ASME, 2009). Since the refinement from mesh M_2 to mesh M_1 only produces a discretization error of 1.66% while increasing the computational cost by a factor of 2, i.e. $N_{M_1} \approx 2 \times N_{M_2}$, the mesh M_2 was chosen for the further analysis.

6.3.2 Effect of rotor-stator interface location

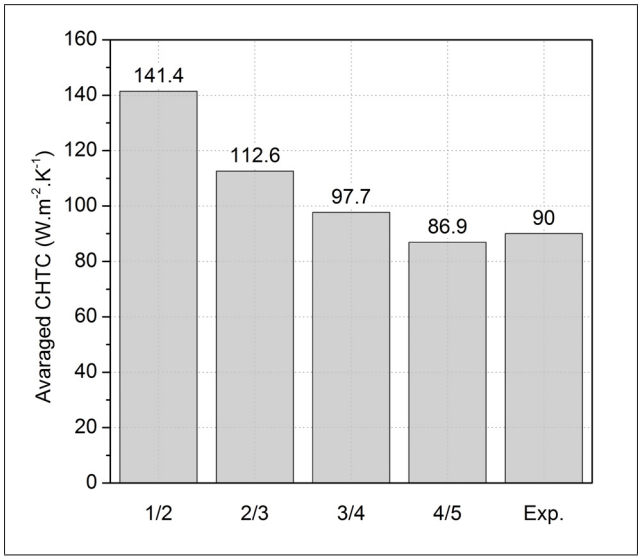

Figure 6.4 Averaged CHTC values on the pole face for different rotor stator interface positions.

Flows in rotor-stator systems are unsteady in nature due to the interaction between the rotor and the stator. The specification of the mixing plane interface allows to perform steady state calculations at a lower computational cost (Galpin *et al.*, 1995). However, in mixing plane simulations, the flow structures are broken at the rotor-stator interface (RSI) since this model introduces an artificial constraint that confines the flow patterns to develop within their local

frame of reference. Due to these constraints on the flow pattern in each frame of reference, the location of the RSI has a significant impact on the flow field prediction in the air gap (Pickering *et al.*, 2002). In order to study the effects of the RSI location, four RSI configurations ($g_R/g = 1/2,\ 2/3,\ 3/4,\ 4/5$), were considered, where g_R is the distance from the rotor outer surface to the RSI and g is the air gap width.

In Figure 6.4, the average CHTC on the pole face computed by different RSI configurations are reported and compared with the experimental data (Torriano *et al.*, 2014). One can observe that the configuration with g_R/g = 1/2 over-predicts the CHTC on the pole face by 57%. As the interface moves toward the stator surface, the average CHTC value decreases. According to this comparison, the best agreement with the experimental data is found for the RSI position between 3/4 and 4/5 with 8.5% and 3.4% errors, respectively.

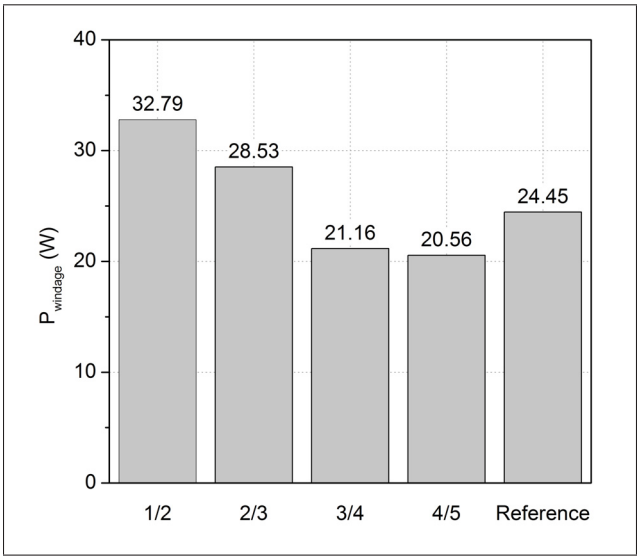

Figure 6.5 Windage loss in the rotating domain computed with different rotor-stator interface configuration.

In Figure 6.5, the windage losses in the rotating domain, computed using Equation 6.9, are plotted on different RSI locations. Seeing as the transient interface model fully takes into account the flow interaction between the rotor and the stator, the windage losses calculated using this model are almost identical for different RSI locations (Toussaint *et al.*, 2011) and are used as a

reference value. The transient simulations were performed using the timestep $\Delta t = 5.55 \times 10^{-5}$ s, and initialized by a mixing plane simulation to speed up the convergence. The results show that for the case with g_R/g=1/2, the windage losses are overestimated by 34% above the reference value, and that the overprediction decreases as the RSI is shifted toward the stator inner surface. At g_R/g= 3/4 and 4/5, the windage losses are underestimated by 13.4% and 15.9%, respectively. Thus, based on this comparison, suitable RSI location would be between 2/3 and 3/4.

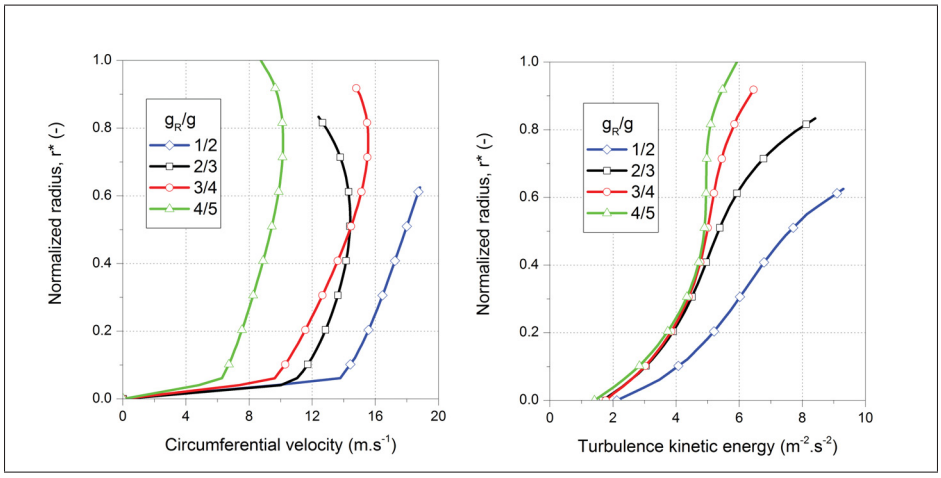

Figure 6.6 (a) Circumferential velocity profiles and (b) turbulence kinetic energy along a line normal to the pole face.

The reduction of the windage losses and the average CHTC on the pole face as the RSI is moved toward the stator can be explained by the increase of the effective cross area through which the airflow penetrates into the air gap region. Since the mass flow rate exiting from the rotor rim duct is unchanged, a lower momentum flow is obtained for the cases where the RSI is closer to the stator surface. This can be seen by examining the typical profiles of the circumferential velocity along a line normal to the pole face for different RSI configurations, as illustrated in Figure 6.6a. It is indicated that the gradients of the circumferential velocity in the radial direction, $\partial U_\theta / \partial r$, decrease as the RSI shifts towards the stator surface. In addition, a typical turbulence kinetic energy profile along a line normal to the pole face, plotted in Figure 6.6b, shows that there is a slight reduction of this quantity as the RSI is moved towards the

stator surface. As a consequence, a lower wall shear stress on the pole face are obtained when the RSI is moved away from the rotor surface. Note that the wall shear stress on the pole face is proportional to the effective viscosity $\mu_{eff} = \mu + \mu_t$ (the eddy viscosity μ_t is a function of the turbulence kinetic energy in the boundary layer) and the gradient of circumferential velocity evaluated at the surface. In turn, this effect results in a lower windage loss in the rotating domain and heat transfer rate in the air gap when the RSI is moved towards the stator surface. The trend of windage loss prediction in this study is diffrent from the one reported in Toussaint *et al.* (2011) where the windage losses increased as the RSI was moved further from the rotor surface. This opposite trend could be attributed to the differences in the computational domain and the velocity profiles used at the inlet boundaries in the two studies. It should be emphasized that Toussaint *et al.* (2011) used a simplified two-dimensional configuration, with which the three-dimensional flow structures, such as the counter-rotating vortex in the meridional (r,z) planes as shown in Figure 6.7, cannot be captured. Moreover, the two-dimensional analysis employed the uniform inlet boundary conditions at the entrance of the rotor rim duct, which consequently produce a flow structure in the air gap that would be inconsistent with the result computed on the full scale model (Bach *et al.*, 2015).

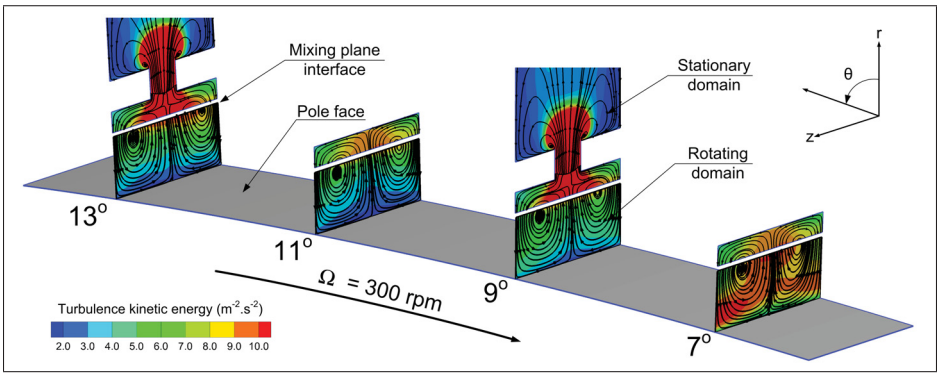

Figure 6.7 Flow structure on the pole face at different angular positions

In the literature, the RSI location was chosen based on past experience rather than on an exact theory, and the central neutral plane between outer rotor and inner stator surfaces are recommended, i.e. $g_R/g = 1/2$. However, as can be seen above, this is not the case for the current

configuration since both CHTC and windage loss computed by this RSI location are overestimated for the case $g_R/g = 1/2$, and a quite good agreement with the reference values was found for the cases where the RSI location is nearer to the stator surface. This phenomenon can be explained by the nature of the mixing plane model and the flow features in the air gap of the current configuration. In the mixing plane model, the steady state flow fields in the rotating and stationary domains are sought, for which a flow dynamics balance between two sides of the rotor-stator interface is satisfied. For the current configuration, the airflow penetrates into the air gap and forms a counter-rotating flow pattern in this region, as shown in Figure 6.7, where the flow structure near the pole face is much more complex as compared to that near the stator surface. Therefore, the flow dynamics contribution to the equilibrium state in the air gap is predominant by the flow feature in the region near pole face, and as a consequence, the appropriate location of the mixing plane interface is found for the case nearer to the stator surface.

In summary, the effect of the rotor-stator location was analyzed based on the CHTC on the pole face and the windage losses, the results suggest that the configuration corresponding to $g_R/g = 3/4$ provides the best accuracy.

6.3.3 Effect of thermal boundary conditions and turbulence models

	Turbulence model	**Thermal boundary condition**
Case 1	SST $k-\omega$	Conjugate heat transfer
Case 2	SST $k-\omega$	Pure convective heat transfer
Case 3	Standard $k-\varepsilon$	Conjugate heat transfer

Table 6.3 Effects of thermal boundary condition.

In the majority of thermal studies in the literature, the pure convective heat transfer method using the uniform temperature or uniform wall heat flux has been actively used to predict the heat transfer rate on the fluid-solid boundary. Many investigations, however, have demonstrated that this approach might induce errors in thermal performance prediction (Iaccarino *et al.*, 2002; Coletti *et al.*, 2012; Cukurel & Arts, 2013). This section presents a comparison

between the pure convective and conjugate heat transfer approaches, as well as, the effects of turbulence models, with respect to the prediction of solid temperature using different cases as summarized in Table 6.3. In the pure convective heat transfer cases, the wall heat flux applied on the fluid-solid boundary for Case 2 was chosen as the average values of wall heat flux over surfaces of the pole (*i.e.* the leading edge, the pole face, and the trailing edge) obtained by the conjugate heat transfer in Case 1 ($q_w = 2000\ W.m^{-2}$).

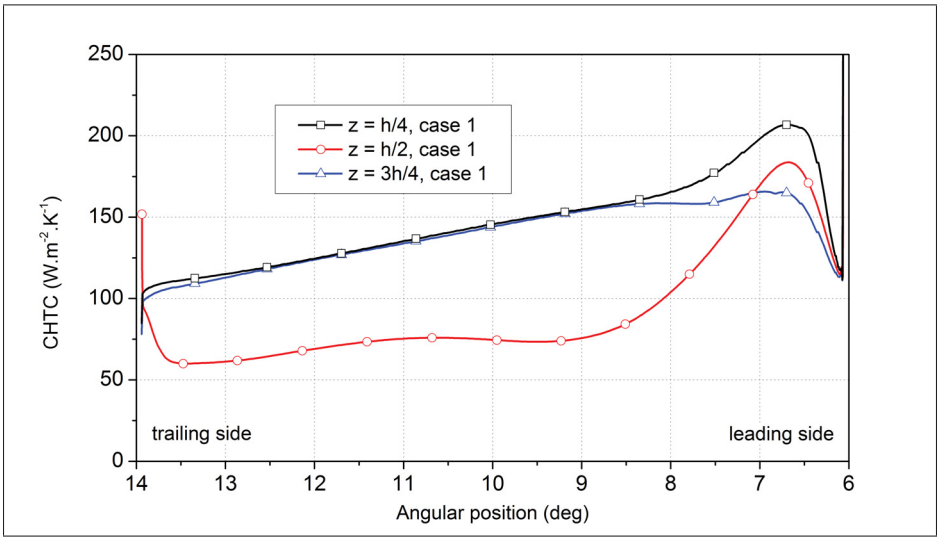

Figure 6.8 CHTC distribution on the pole face at different axial positions.

In Figure 6.8, the CHTC distribution on three lines along the pole face at different axial locations are plotted for the conjugate heat transfer simulation (Case 1). In the upstream region near the leading side, the local maximum of the CHTC are observed as an effect of the impingement of the flow exiting from the rotor rim duct on the pole face at the attachment region, then the CHTC profiles decrease as the flow develop over the pole face. It can be observed that a lower heat transfer rate at the central line ($z = h/2$) in comparison with the two sides ($z = h/4$ and $z = 3h/4$). Herein, h is the width of the computational domain in the axial direction. These findings can be explained by examining the mean flow structure and the turbulent field in the corresponding areas.

In Figure 6.9, the contour of the turbulent kinetic energy and streamlines are illustrated for

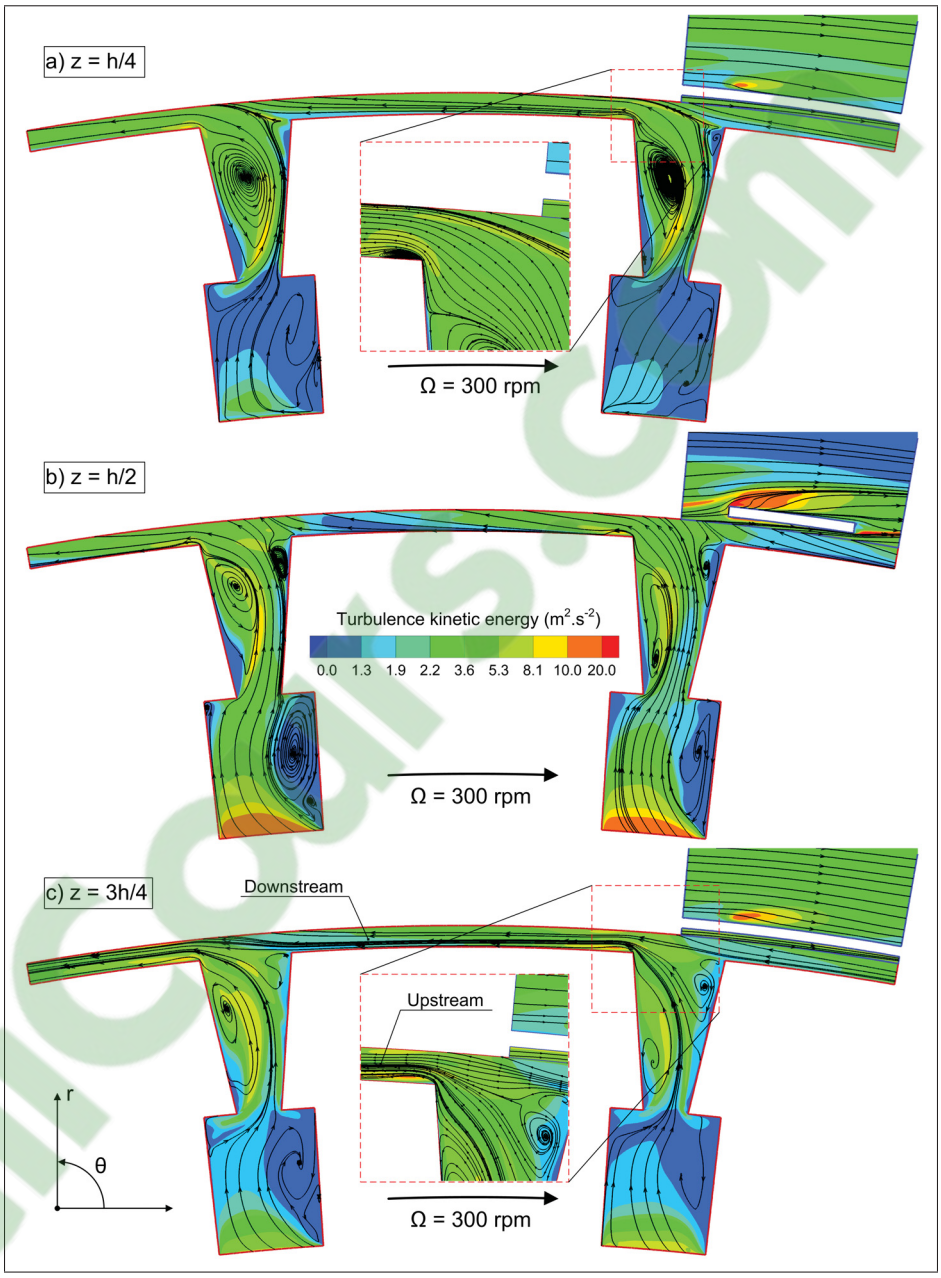

Figure 6.9 Streamlines and the turbulence kinetic energy contour in the $r-\theta$ planes at different axial positions.

the conjugate heat transfer simulation (Case 1) on different (r, θ) planes. In Figures 6.10, the Reynolds shear stress components (a) $\overline{u'_r u'_\theta}$, (b) $\overline{u'_\theta u'_z}$, (c) $\overline{u'_z u'_r}$; (d) the turbulence kinetic energy, and (e) the turbulent thermal conductivity are illustrated on a radial plane (z, θ) near the rotor pole face. It is observed from Figure 6.10 that in the upstream region of the air gap flow, almost

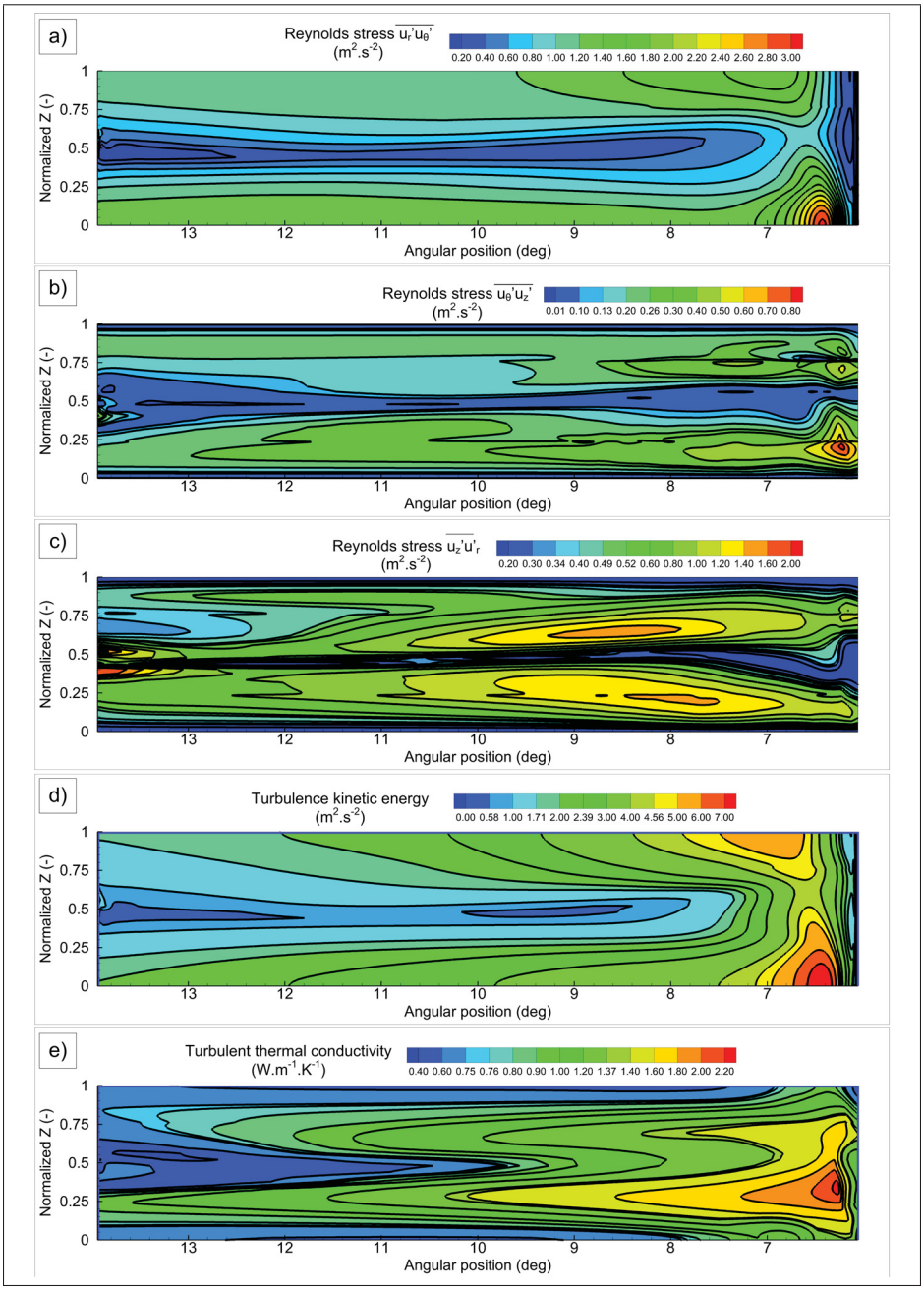

Figure 6.10 Contour of Reynolds stress component (a) $\overline{u_r'u_\theta'}$, (b) $\overline{u_\theta'u_z'}$, (c) $\overline{u_z'u_r'}$, (d) the turbulence kinetic energy and (e) turbulent thermal conductivity on radial iso-surfaces near the pole face.

the same magnitude of k are obtained for three locations. In the downstream region, the values of turbulence kinetic energy and Reynolds stress components on the two sides of the pole face

($z = h/4$ and $z = 3h/4$) are higher than those on the central line ($z = h/2$). The combination of higher turbulent normal stress and shear stress values results in a higher turbulent thermal conductivity, λ_t, on the two axial ends of the poles than those on the central region, as depicted in Figure 6.10e. Note that the turbulent thermal conductivity, λ_t, is proportional to the eddy viscosity μ_t, which is strongly correlated with local Reynolds stress components.

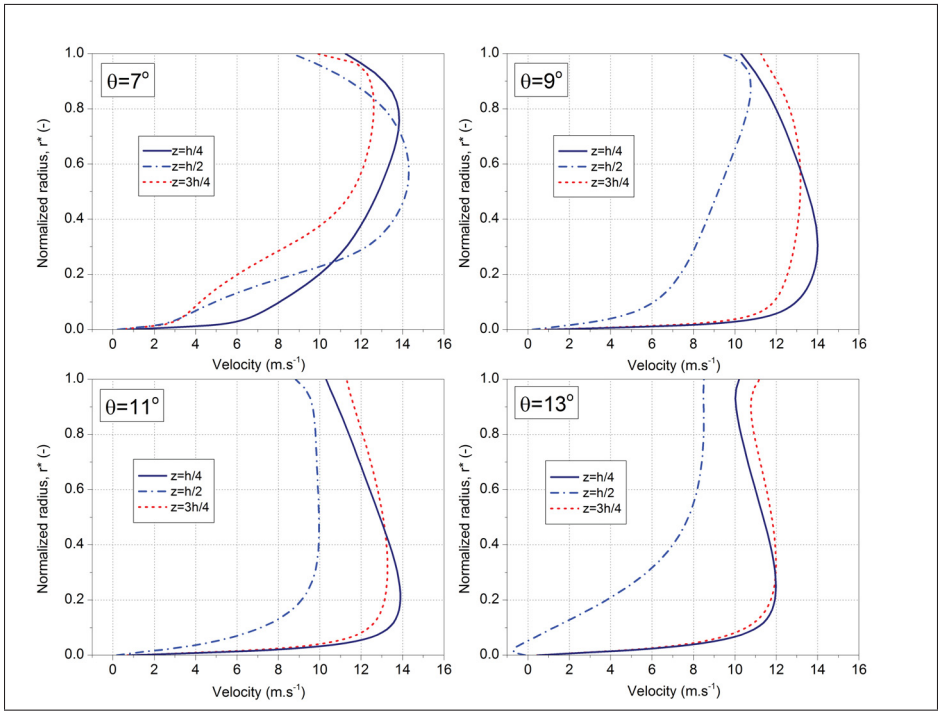

Figure 6.11 Profiles of circumferential velocity (U_θ) along different lines normal to pole face at different axial and angular positions.

In Figure 6.11, the circumferential velocity component along three axial lines normal to the pole face at different angular positions are plotted. Results show that in the vicinity of the pole face, the gradients of the circumferential velocity, $\partial U_\theta / \partial r$, at two sides of the pole face are higher than that on the central line. This variation of circumferential velocity results in the temperature gradients, $\partial T / \partial r$, along the corresponding lines as shown in Figure 6.12. These observations on the contours of the eddy viscosity and temperature gradients along different lines are well correlated with the CHTC values, as depicted in Figure 6.8 and discussed above.

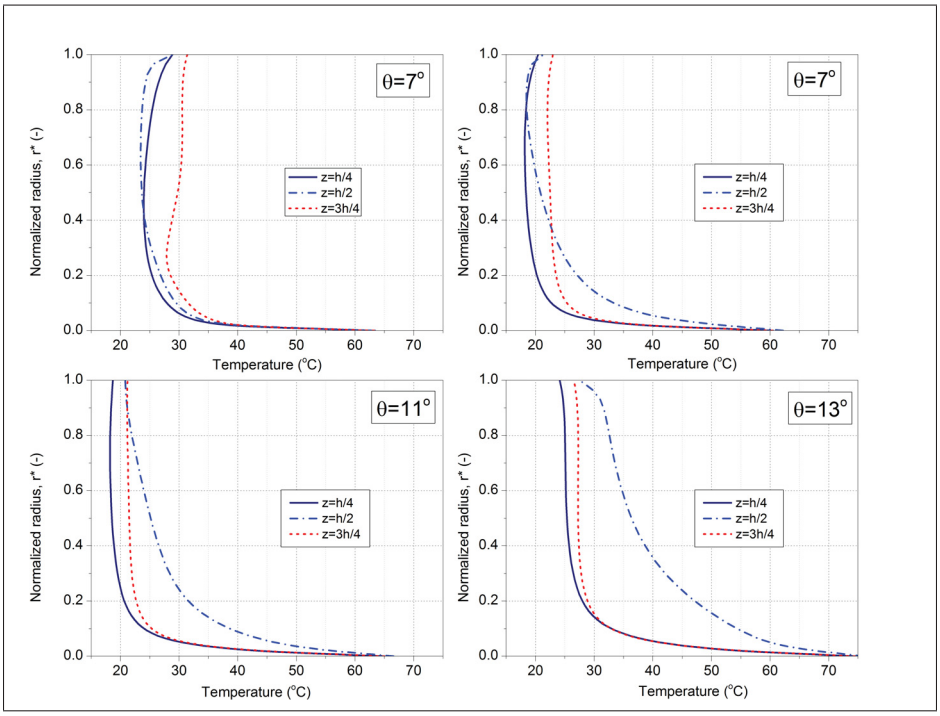

Figure 6.12 Temperature along different axial lines normal to pole face at different angular positions.

It should be noted that the amount of heat extraction from the solid is proportional to the effective thermal conductivity $\lambda_{eff} = \lambda_f + \lambda_t$ and the temperature gradient in the vicinity of the wall as follows:

$$q_w \approx \left(\lambda_f + \lambda_t\right) \left.\frac{\partial T}{\partial r}\right|_{r=r_{surface}} \tag{6.11}$$

In Figure 6.13, the solid temperature profiles along three lines at different axial locations are reported for Case 1. It was observed that the temperature profiles at different axial lines are nearly identical, which indicates that the variation of CHTC distribution on the pole face discussed above have less impact on the temperature prediction in the axial direction. This result is due to a very low Biot number based on the width of the pole face in axial direction, $Bi \approx 0.036$, is found for the typical CHTC level on the pole face, which results in a relatively uniform temperature distribution in the axial direction.

A comparison of CHTC and temperature distribution along the pole face at different axial loca-

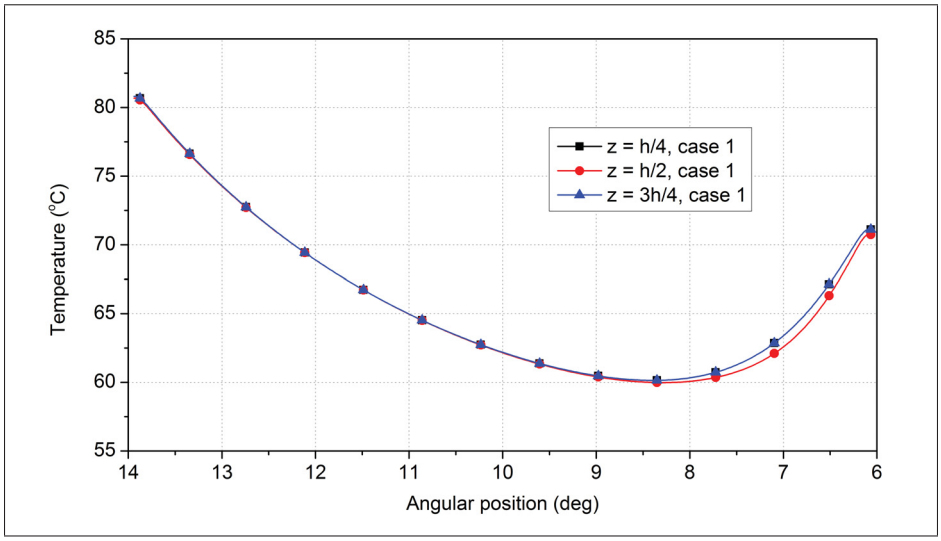

Figure 6.13 Temperature profiles on the pole face at different axial positions.

tions for different cases in Table 6.3 are reported in Figure 6.14 and 6.15, respectively. Herein, to obtain the temperature field in the solid components corresponding to Case 2, the following procedure has been performed. In the first step, the CHTC distribution on the fluid-solid interface was calculated from the simulation of pure convective method using a uniform wall heat flux as discussed above. The extracted CHTC distribution was then applied on the fluid-solid boundary of the solid domain and the heat conduction equation was solved to acquire the temperature field. In the later simulation, the physical properties of solid and heat source magnitude were taken as with the conjugate heat transfer (Case 1).

Results in Figure 6.14 point out that in general the CHTC predicted by the conjugate approach (Case 1) is higher than that computed by the pure convective approach (Case 2), except for the leading side ($\theta \leq 9°$) at the central line, where the CHTC levels predicted by both approaches are quite similar. Consequently, there is a certain miscalculation of temperature profiles between these cases, as demonstrated in Figure 6.15. The wall temperature is overpredicted by the pure convective approach as compared to that computed from the CHT method. The local maximum difference in temperature between Case 1 and Case 2 was found as 7°C, corresponding to a relative difference of 10%. This relatively large difference can be attributed to

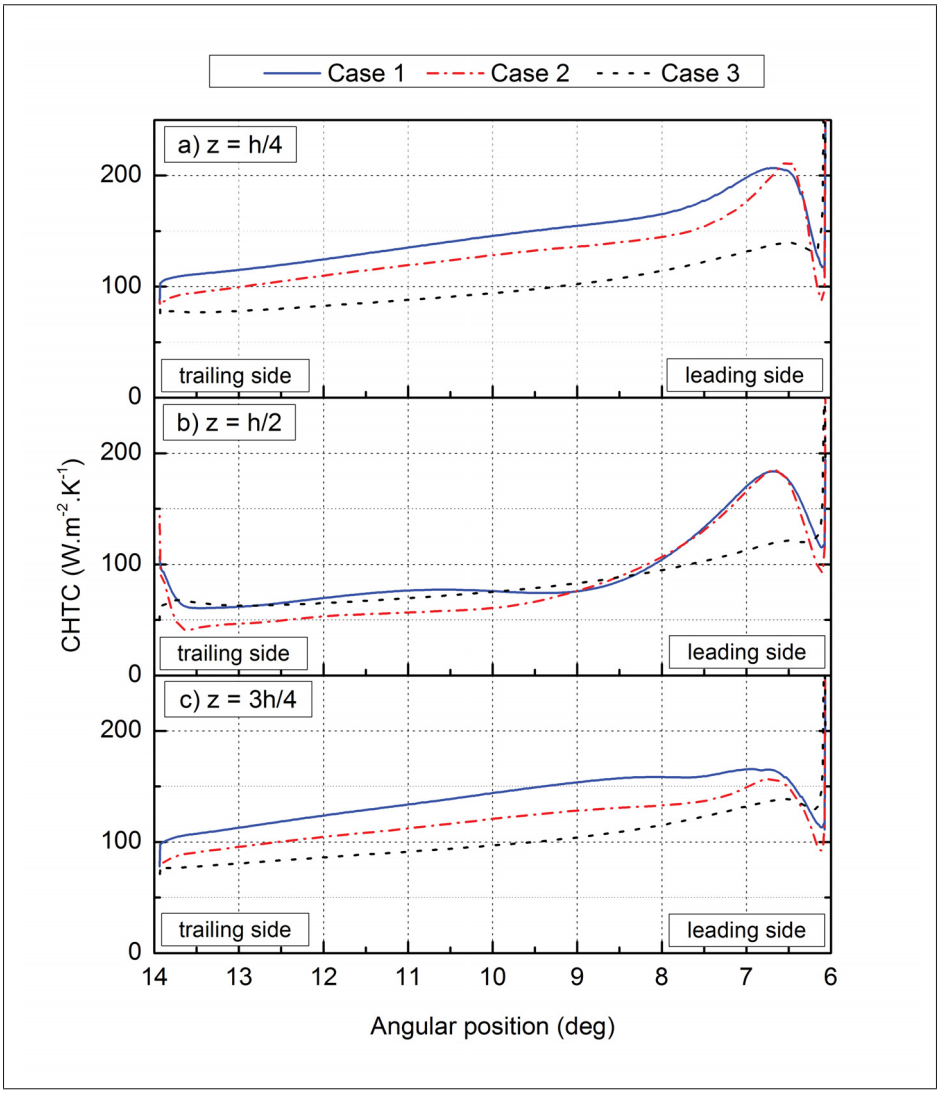

Figure 6.14 CHTC distribution along the pole face at different axial locations.

the inappropriate wall heat flux magnitudes prescribed on the surfaces of the pole in the pure convective heat transfer. Indeed, an analysis on the heat transfer rate on each surface of the pole indicates that there is a large variation of wall heat flux levels on the pole face (3524 $W.m^{-2}$), on the leading edge (1052 $W.m^{-2}$), and on the trailing edge (1436 $W.m^{-2}$) due to the local flow characteristics in each region. Therefore, using a single value of wall heat flux to impose on all surfaces of pole would lead to miscalculation of thermal performance.

Results in Figure 6.14 indicate that although a quite good agreement in CHTC prediction is ob-

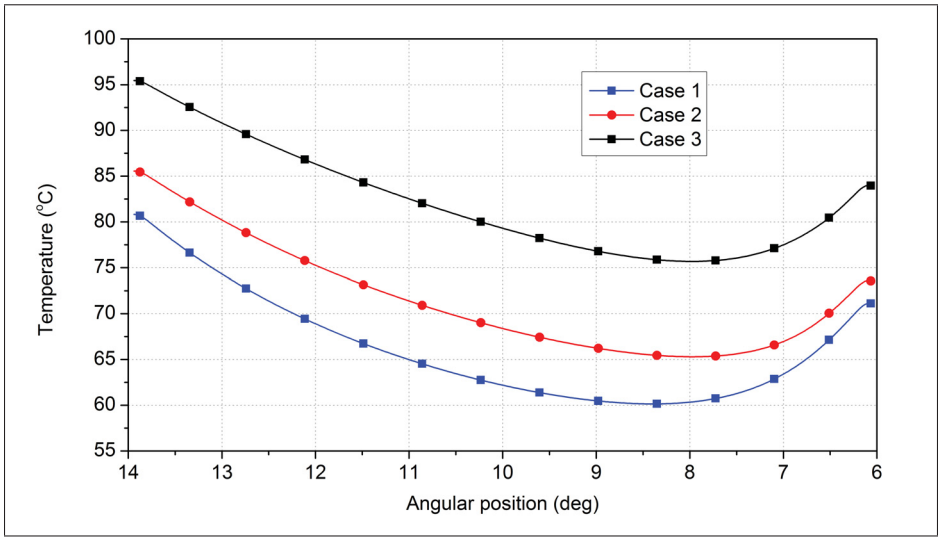

Figure 6.15 Temperature distribution along the central line of the pole face for different cases.

tained between the cases computed by the standard $k-\varepsilon$ model and the SST $k-\omega$ model, this match only occurs along the central line of the pole face and only in average manner. On two sides of the pole face, the CHTC values predicted by the standard $k-\varepsilon$ model are much lower than those predicted by the SST $k-\omega$ model with a maximum difference up to 35%. This results in a large difference of temperature profiles between two models with a mean difference of 15.9°C and a maximum difference of 17.5°C. It is well known that an accurate prediction of the solid temperature field is essential in being able to determine the operating regime of the large hydro-generator. For every 10°C increase in operating temperature of the hydro-generator, the winding insulating materials will thermally age twice as fast (Folting & Jenau, 2014). The accelerated aging of the insulating material might lead to premature failures that compromise the integrity of the hydro-generator. In addition, the maximum temperature in the machine is limited by the type of insulating materials. If the temperature is lower than the critical values, it means the hydro-generator can be pushed to operate at a higher power level without reducing the lifetime of the machine.

6.4 Conclusions

An understanding of the airflow features in the air-gap region is essential to ensuring an efficient cooling of the salient rotor in the hydro-generator. However, the experimental approach is highly costly and therefore not often applied to this region. The present work is dedicated to the computational fluid dynamics simulations on a rotor-stator system to predict the flow and thermal features in the air-gap region. Numerical simulations have been carried out using RANS turbulence closures and the mixing plane interface model for rotor-stator coupling. Calculations were performed on the simplified model of a rotor-stator system using the mean flow velocity and turbulent fields extracted from a validated CFD simulation on the full scale rotating model as the inlet boundary conditions. The effects of rotor-stator interface location were analyzed through the computations for different configurations. Also, the effect of the solid heat conduction in the numerical model is thoroughly discussed.

Results demonstrated that the rotor-stator interface location has a significant impact on the air ventilation and thermal performance prediction in the air gap. As the interface shifts toward the stator inner surface, the predicted convective heat transfer coefficient and windage loss values decrease. Based on a comparison of the windage loss and convective heat transfer coefficients computed on different rotor-stator locations with the reference values, the optimal rotor-stator interface location was found for the case with $g_R/g = 3/4$.

Results also indicated that the impingement of the flow at the upstream region near the leading side and the presence of the counter-rotating vortex in the air gap in the downstream region have a significant impact on the convective heat transfer coefficients profiles on the pole face. While this structure of flow has a strong influence on the temperature calculation on the pole face in the circumferential direction, it has less impact in the axial direction. It is apparent that the choice of turbulence models plays an important role in the prediction of the flow structure and thus has a great influence on the prediction of temperature on the pole face. In comparison with the Shear Stress Transport $k-\omega$ model, the standard $k-\varepsilon$ model typically overpredicts temperature profiles on the pole face 15.9°C , and the maximum difference was found to be 17.5°C. Furthermore, the temperature prediction on the pole face is also affected by the ther-

mal boundary conditions employed. The local maximum difference of 7°C, corresponds to an overestimation of 10% of temperature values in the pure convective case as compared to the conjugate heat transfer approach.

CONCLUSION AND RECOMMENDATIONS

The work presented in this thesis focuses on the application of computational fluid dynamics simulations to predict the turbulent convective heat transfer in the air gap of hydro-generators. The mean flow and turbulent fields in the rotor-stator air gap were taken into considerations, since a concentration of magnetic losses were found on the rotor tip, and thus efficient cooling is required. The numerical results are compared against the experimental data in each part of the presented chapters, the conclusions and recommendations for future works are outlined.

The thesis begins with an introduction on the convective cooling in the hydro-generator. Then, the mathematical model for the convective heat transfer phenomenon, that includes the fluid dynamics governing equations and the heat conduction equation, was presented in Chapter 1. A literature review on the application of computational fluid dynamics for the thermal analysis in the large hydro-generator was reported in Chapter 2. The methodology and numerical strategy used in the thesis are presented in Chapter 3.

In Chapter 4, the efficiency of a two-dimensional simplified model in predicting the flow and thermal fields in hydro-generators was assessed. A comparison of flow fields computed with different multiple frames of reference approaches, including the frozen rotor, the mixing plane and the transient interface models, indicated that the mixing plane model provided a flow field that better matches with the one obtained by the time-averaged transient interface model. The frozen rotor model, however, produced a result that showed a strong dependency on the position of the rotor relatively to the stator. Furthermore, in terms of computational cost, the simulations with the frozen rotor model required more computing resource compared to the mixing plane model since the same pitch angle must be defined for the stationary and rotating domains. Regarding the turbulence modelling, results showed that the standard $k-\varepsilon$ and the Wilcox's $k-\omega$ models over-predicted the turbulence kinetic energy in the air gap region and consequently over-estimated the convective heat transfer coefficients on the rotor pole face. On average, the Re-Normalization Group $k-\varepsilon$ and the Shear Stress Transport $k-\omega$ models were

found to be more appropriate for the prediction of the convective heat transfer coefficients on the pole face since they produced the results that better matched with the experimental data with relative differences of 13.3% and 6.6%, respectively. Furthermore, it was shown that the thermal boundary conditions have different effects on the convective heat transfer prediction depending on the local flow characteristics. The inclusion of the solid domain in the numerical model has a strong impact on the heat transfer prediction in recirculating regions, where the cooling air extracts the heat mainly via the conduction mode. On the contrary, in the regions of wall-attached flows, the CHTC values computed by the conjugate and pure convective heat transfer model were quite similar with a maximum relative difference smaller than 10%. Although the two-dimensional configuration is favoured because of its low computational cost, it unfortunately does not account for the effects of three-dimensional flows.

Based on the analysis discussed in Chapter 4, the improvement in terms of simplified geometrical configuration was made in Chapter 5. The computational domain extend axially to take into account the effect of three dimensional flows in the configuration. The mixing plane was used at the rotor-stator interface. The conjugate heat transfer was employed. A mesh sensitivity analysis indicated that for the low-Reynolds number model, the computational mesh should have at least 12×10^6 cells in total with a requirement on the dimensionless near-wall distance, $y^+ < 1$ to gain a mesh independent solution. Nevertheless, this requirement was not strict, the mesh with a slightly higher dimensionless near-wall distance, $y^+ \approx 5$, can be employed for quantitative prediction of the CHTC since it generally captured the trend of the CHTC and showed a relatively good agreement with the reference case (the finest mesh case).

The results of CHTC prediction on the pole face using different eddy-viscosity turbulence models showed that the best agreement with experimental data was obtained with the SST $k-\omega$ model. However, there still was a certain discrepancy between the numerical results and experimental data, especially in the trailing side region of the pole face. With respect to the flow and thermal prediction in the boundary layer, although the wall-function concept was not expected

to accurately predict the convective heat transfer calculations, the results computed in this particular study revealed that this model can be used for predicting the CHTC on the pole face. The thermal boundary conditions at the fluid-solid interface and the use of temperature-dependent fluid properties have an impact on the accuracy of the convective heat transfer calculation. The use of the conjugate heat transfer method with the temperature-dependent fluid properties shows a better agreement with the experimental data.

The paper presented in Chapter 6 is an extension of the previous article, in which there is an attempt to seek a further understanding on the ventilation airflow features in the rotor-stator air-gap region. Numerical CFD simulations were performed using Reynolds-averaged Navier-Stokes turbulence closures and the multiple frames of reference mixing plane interface model for rotor-stator coupling. To reduce the computational cost, computations were carried out on a three-dimensional simplified model of the hydro-generator rotor-stator system using the mean flow velocity and turbulent fields, extracted from a validated CFD simulation of the full scale rotating model, as the inlet boundary conditions.

The effects of the rotor-stator interface location on the convective heat transfer characteristics were analyzed through the numerical simulations on different configurations. Results have demonstrated that the rotor-stator interface location demonstrates a significant impact on the air ventilation and thermal performance prediction in the air gap region. As the interface shifts toward the stator inner surface, the convective heat transfer coefficient and windage loss prediction decrease. According to a comparison with the reference values, the optimal RSI location was found for configuration with $g_R/g = 3/4$.

Also, the effect of the solid heat conduction in the numerical model is thoroughly discussed. Although the presence of the counter-rotating vortex in the meridional planes has significant impact on the convective heat transfer coefficients, it has less influence on the solid temperature calculation. On the contrary, the prediction of temperature on the solid pole face is greatly affected by the thermal boundary condition prescribed. Indeed, a local difference of 10°C was

observed for the temperature values on the pole face between the conjugate and the pure convective heat transfer cases.

Recommendation for future work

Convective cooling in the hydro-generator is a complex phenomenon and contains a great deal of challenges that cannot be addressed within a doctoral thesis with limited duration. Although the numerical analysis of the simplified model presented in this thesis provided useful information on the flow and thermal aspects in the full scale model, the present work should be literally considered as a contribution towards the better understanding of the convective cooling in hydro-generators examined using the numerical modelling. Many improvements for the better prediction of the thermo-fluids phenomena in the machine might be suggested as follows:

- In the present study, the numerical simulations were performed on a configuration with only one section of the pole in the axial direction and a sector of 20° in the circumferential direction. The effects of imposing the symmetry boundary conditions in the axial directions are apparent. In the future, to improve the CHTC predictions at the pole face, the simulations will be carried out on the full three-dimensional geometry of the pole and the computed temperature on the pole surface will be compared with the measured values (Torriano *et al.*, 2014). In the event of limited computing resources, for which the full scale model cannot be performed, at least the extension of the simplified model in the axial direction is recommended to eliminate the effect of the imposed boundary condition to the flow field prediction in the configuration.
- With respect to the turbulence modelling, the current study employs the Reynolds-averaged Navier-Stokes turbulence model based on the Boussinesq approximation, in which the eddy-viscosity (turbulent viscosity) is considered to be isotropic. It is recommended to use higher fidelity models, such as the Reynolds Stress Models (RSM), the Large Eddy Simulation, or hybrid turbulence models.

- Regarding the rotor-stator flow interaction modelling, to reduce computational effort, the majority of studies in this thesis is based on the steady state multiple frames of reference mixing plane model, which evidently consists of approximations. The mixing plane model is employed to represent the effect of the unsteady flow interaction between rotor and stator via a steady state computations using the circumferential averaging on the interface. In the future, the transient interface model is recommended to fully take into account the inherent unsteadiness of rotor-stator configuration.
- More PIV measurement data, especially in the air gap between the rotor and stator, should be obtained to validate the numerical results.

APPENDIX I

REYNOLDS-AVERAGED TURBULENCE MODELS

1. The standard $k-\varepsilon$ model

In the standard $k-\varepsilon$ turbulence model, the turbulent kinetic energy, $k(m^2/s^2)$, and dissipation rate, $\varepsilon(m^2/s^3)$ are used to express the turbulent viscosity, which is calculated as:

$$\mu_t = \rho C_\mu \frac{k^2}{\varepsilon} \tag{A I-1}$$

The equation for the turbulent kinetic energy, k, is derived from the Navier-Stokes equations and reads

$$\frac{\partial}{\partial t}(\rho k) + \frac{\partial}{\partial x_j}(\rho U_j k) = \frac{\partial}{\partial x_j}\left[\left(\mu + \frac{\mu_t}{\sigma_k}\right)\frac{\partial k}{\partial x_j}\right] + \underbrace{\rho P_k}_{production} - \underbrace{\rho\varepsilon}_{dissipation} \tag{A I-2}$$

Specific turbulence dissipation, ε:

$$\frac{\partial}{\partial t}(\rho \varepsilon) + \frac{\partial}{\partial x_j}(\rho U_j \varepsilon) = \frac{\partial}{\partial x_j}\left[\left(\mu + \frac{\mu_t}{\sigma_\varepsilon}\right)\frac{\partial \varepsilon}{\partial x_j}\right] + \underbrace{C_{\varepsilon 1}\frac{\varepsilon}{k}P_k}_{production} - \underbrace{C_{\varepsilon 2}\rho\frac{\varepsilon^2}{k}}_{dissipation} \tag{A I-3}$$

where the production term is defined as:

$$P_k = \tau_{ij}\frac{\partial u_i}{\partial x_j} = 2\mu_t S_{ij} S_{ij} \tag{A I-4}$$

$$S_{ij} = \frac{1}{2}\left(\frac{\partial U_i}{\partial x_j} + \frac{\partial U_j}{\partial x_i}\right) \tag{A I-5}$$

The closure coefficients are: $C_{\varepsilon 1} = 1.44$, $C_{\varepsilon 2} = 1.92$, $C_\mu = 0.09$, $\sigma_k = 1.0$, $\sigma_\varepsilon = 1.3$.

2. The Re-normalization Group $k-\varepsilon$ model

The two-equation eddy-viscosity RNG $k-\varepsilon$ model is a variant of the standard $k-\varepsilon$ turbulence model, which is developed by Yakhot *et al.* (1992) and based on the Re-Normalization Group method. The Navier-Stokes equations are renormalized to account for the effects of small scales of motion. The transport equation for kinetic energy in this model is similar to the one for the standard $k-\varepsilon$ model. The transport equation for turbulence dissipation is expressed as:

$$\frac{\partial}{\partial t}(\rho\varepsilon)+\frac{\partial}{\partial x_j}(\rho U_j\varepsilon)=\frac{\partial}{\partial x_j}\left[\left(\mu+\frac{\mu_t}{\sigma_\varepsilon}\right)\frac{\partial\varepsilon}{\partial x_j}\right]+C_{\varepsilon 1}\frac{\varepsilon}{k}P_k-C^*_{\varepsilon 2}\rho\frac{\varepsilon^2}{k} \tag{A I-6}$$

where:

$$C^*_{\varepsilon 2}=C_{\varepsilon 2}+\frac{C_\eta\eta^3(1-\eta/\eta_0)}{1+\beta\eta^3} \tag{A I-7}$$

$$\eta=S\frac{k}{\varepsilon} \tag{A I-8}$$

$$S=\sqrt{2S_{ij}S_{ij}} \tag{A I-9}$$

$$\mu_t=\rho C_\mu\frac{k^2}{\varepsilon} \tag{A I-10}$$

The closure coefficients are $C_{\varepsilon 1}=1.4$, $C_{\varepsilon 1}=1.68$, $C_\mu=0.0845$, $\sigma_k=0.7194$, $\sigma_\varepsilon=0.7194$, $\eta_0=4.38$, and $\beta=0.012$.

3. The Wilcox $k-\omega$ model

This turbulence model was originally developed by Wilcox (1988), solves two transport equations: one for turbulent kinetic energy, k, and one for the turbulent frequency, ω.

$$\frac{\partial}{\partial t}(\rho k)+\frac{\partial}{\partial x_j}(\rho U_j k)=\frac{\partial}{\partial x_j}\left[(\mu+\sigma_k\mu_t)\frac{\partial k}{\partial x_j}\right]+P_k-\beta^*\rho\omega k \tag{A I-11}$$

$$\frac{\partial}{\partial t}(\rho\omega)+\frac{\partial}{\partial x_j}(\rho U_j\omega)=\frac{\partial}{\partial x_j}\left[(\mu+\sigma_k\mu_t)\frac{\partial\omega}{\partial x_j}\right]+\frac{\gamma\omega}{k}P_k-\beta\rho\omega^2 \tag{A I-12}$$

The eddy-viscosity is calculated by:

$$\mu_t=\frac{\rho k}{\omega} \tag{A I-13}$$

The closure coefficients are defined as: $\sigma_k = 0.5, \sigma_\omega = 0.5, \beta^* = 0.09, \beta = 3/40, \gamma = 5/9$. The $k-\omega$ model has become a widely used turbulence model for wall-bounded, aerodynamic flow, for two main reasons: it does not require any wall-damping functions for the computation of wall distances, and it is less stiff than the $k-\varepsilon$ models in the near-wall region. The first property is particularly desirable for complex configurations. However, the Wilcox $k-\omega$ model has one main drawback: the results depend strongly on the freestream eddy-viscosity levels. This freestream dependence seems to be the strongest for free shear layers but is also signicant for boundary layers.

4. The Shear Stress Transport (SST) $k-\omega$ model

The Menter's SST model (Menter, 1994) blends the $k-\varepsilon$ and the $k-\omega$ submodels according to the local flow regime, with the equations cast in $k-\omega$ form. Two transport equations for the turbulence kinetic energy and turbulence frequency written in conservation form are given by the following:

$$\frac{\partial}{\partial t}(\rho k) + \frac{\partial}{\partial x_j}(\rho U_j k) = \frac{\partial}{\partial x_j}\left[(\mu + \sigma_k \mu_t)\frac{\partial k}{\partial x_j}\right] + P_k - \beta^* \rho \omega k \tag{A I-14}$$

$$\frac{\partial}{\partial t}(\rho \omega) + \frac{\partial}{\partial x_j}(\rho U_j \omega) = \frac{\partial}{\partial x_j}\left[(\mu + \sigma_\omega \mu_t)\frac{\partial \omega}{\partial x_j}\right] + \alpha \frac{\omega}{k} P_k - \beta \rho \omega^2 + 2(1-F_1)\frac{\rho \sigma_{\omega 2}}{\omega}\frac{\partial k}{\partial x_i}\frac{\partial \omega}{\partial x_i} \tag{A I-15}$$

The coefficients in the SST model are blended as a linear combination of the corresponding coefficients of the $k-\omega$ model (inner region, subscript 1) and the $k-\varepsilon$ (outer region, subscript 2), i.e.:

$$\phi_3 = \phi_1 F_1 + \phi_2 (1 - F_1) \tag{A I-16}$$

Additional functions are given by:

$$F_1 = tanh\left(min\left[max\left(\frac{\sqrt{k}}{\beta^*\omega y}, \frac{500\nu}{y^2\omega}\right), \frac{4\sigma_{\omega 2}k}{CD_{k\omega}y^2}\right]^4\right) \tag{A I-17}$$

$$F_2 = tanh\left(max\left[\frac{\sqrt{k}}{\beta^*\omega y}, \frac{500\nu}{y^2\omega}\right]\right) \tag{A I-18}$$

$$CD_{k\varepsilon} = max\left(2\frac{\rho\sigma_{\omega 2}}{\omega}\frac{\partial k}{\partial x_i}\frac{\partial \omega}{\partial x_i}, 10^{-10}\right) \tag{A I-19}$$

$$P_k = min\left(\tau_{ij}\frac{\partial U_i}{\partial x_i}, 10\beta^* k\omega\right) \tag{A I-20}$$

Here y is the distance to the nearest wall and μ is the molecular dynamic viscosity.

The turbulent viscosity is computed from:

$$\mu_t = \frac{\rho a_1 k}{max(a_1\omega, \Omega F_2)} \tag{A I-21}$$

where $\Omega = \sqrt{2W_{ij}W_{ij}}$ is vorticity magnitude with:

$$W_{ij} = \frac{1}{2}\left(\frac{\partial U_i}{\partial x_j} - \frac{\partial U_j}{\partial x_i}\right) \tag{A I-22}$$

The recommended boundary conditions are:

$$\omega_{wall} = 10\frac{6\nu}{\beta_1 y^2} \tag{A I-23}$$

$$k_{wall} = 0 \tag{A I-24}$$

The closure coefficients are specified as follows: $\beta^* = 0.09$, $\alpha_1 = 5/9$, $\alpha_2 = 0.44$, $\beta_1 = 0.075$, $\beta_2 = 0.0828$, $\sigma_{k1} = 0.5$, $\sigma_{k1} = 1.0$, $\sigma_{\varepsilon 1} = 0.5$, $\sigma_{\varepsilon 2} = 107/125$.

The model has been seen to be more advantageous than the submodels in terms of prediction of the location of separation and the size of separated regions. The SST model retains the robustness and accuracy near the wall associated with the Wilcox $k-\varepsilon$ model while preserving

the free-stream independence and the more accurate prediction of free-shear layers obtained by the Jones and Launder $k-\omega$ model.

APPENDIX II

REYNOLDS STRESSES IN THE CYLINDRICAL COORDINATES

Denote $\partial_s(.) = \partial(.)/\partial s$, the Reynolds stress components in the cylindrical coordinates are expressed as follows:

$$\tau_{r\theta} = -\rho\overline{u'_r u'_\theta} = \mu_t\left(\frac{1}{r}\frac{\partial U_r}{\partial\theta} - \frac{U_\theta}{r} + \frac{\partial U_\theta}{\partial r}\right) = \mu_t\left(\frac{1}{r}\partial_\theta U_r - \frac{U_\theta}{r} + \partial_r U_\theta\right) \tag{A II-1}$$

$$\tau_{\theta z} = -\rho\overline{u'_\theta u'_z} = \mu_t\left(\frac{1}{r}\frac{\partial U_z}{\partial\theta} + \frac{\partial U_\theta}{\partial z}\right) = \mu_t\left(\frac{1}{r}\partial_\theta U_z + \partial_z U_\theta\right) \tag{A II-2}$$

$$\tau_{zr} = -\rho\overline{u'_z u'_r} = \mu_t\left(\frac{\partial U_z}{\partial r} + \frac{\partial U_r}{\partial z}\right) = \mu_t\left(\partial_r U_z + \partial_z U_r\right) \tag{A II-3}$$

Let the mean velocity vector $\mathbf{U} = U_r\mathbf{e}_r + U_\theta\mathbf{e}_\theta + U_z\mathbf{e}_z$ in the cylindrical coordinates with basis $(\mathbf{e}_r, \mathbf{e}_\theta, \mathbf{e}_z)$ and $\mathbf{U} = U_x\mathbf{i} + U_y\mathbf{j} + U_z\mathbf{k}$ in the Cartesian coordinates with basic $(\mathbf{i}, \mathbf{j}, \mathbf{k})$. The velocity components in these two coordinates are related by:

$$\begin{pmatrix} U_r \\ U_\theta \\ U_z \end{pmatrix} = \begin{pmatrix} cos\theta & sin\theta & 0 \\ -sin\theta & cos\theta & 0 \\ 0 & 0 & 1 \end{pmatrix} \begin{pmatrix} U_x \\ U_y \\ U_z \end{pmatrix} \tag{A II-4}$$

Each expressions of the rate-of-strain in the Reynolds stress components are calculated as follows:

$$\begin{aligned} \partial_\theta U_r &= \partial_\theta\left(cos\theta U_x\right) + \partial_\theta\left(sin\theta U_x\right) \\ &= -sin\theta U_x + cos\theta\,\partial_\theta U_x + cos\theta U_y + sin\theta\,\partial_\theta U_y \\ &= -sin\theta U_x + cos\theta\left(\partial_x U_x\cdot\partial_\theta x + \partial_y U_x\cdot\partial_\theta y\right) + cos\theta U_y + sin\theta\left(\partial_x U_y\cdot\partial_\theta x + \partial_y U_y\cdot\partial_\theta y\right) \end{aligned} \tag{A II-5}$$

$$\begin{aligned} \partial_r U_\theta &= -sin\theta\,\partial_r U_x + cos\theta\,\partial_r U_y \\ &= -sin\theta\left(\partial_x U_x\cdot\partial_r x + \partial_y U_x\cdot\partial_r y\right) + cos\theta\left(\partial_x U_y\cdot\partial_r x + \partial_y U_y\cdot\partial_r y\right) \end{aligned} \tag{A II-6}$$

$$\partial_\theta U_z = \partial_x U_z \cdot \partial_\theta x + \partial_y U_z \cdot \partial_\theta y \tag{A II-7}$$

$$\partial_z U_\theta = -sin\theta \partial_z U_x + cos\theta \partial_z U_y \tag{A II-8}$$

$$\partial_r U_z = \partial_x U_z \cdot \partial_r x + \partial_y U_z \cdot \partial_r y \tag{A II-9}$$

$$\partial_z U_r = cos\theta \partial_z U_x + sin\theta \partial_z U_y \tag{A II-10}$$

Noted that as a results of post-processing $\partial_i \phi$ with $i = r, \theta, z$ and $\phi = x, y, z$ are available for calculations.

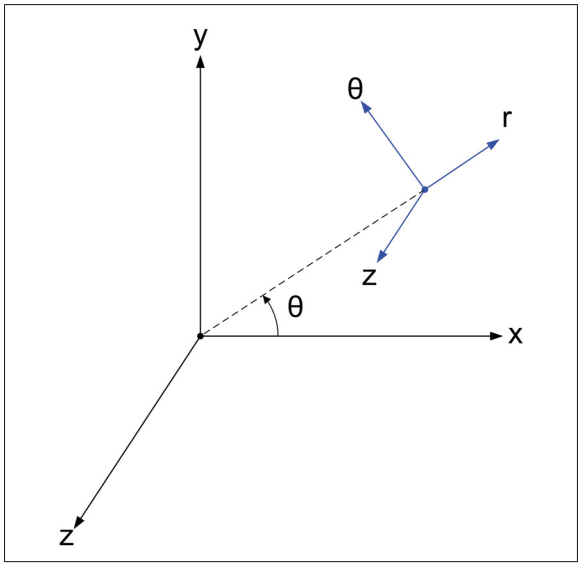

Figure-A II-1 Cylindrical coordinates

LIST OF REFERENCES

(2008). Procedure for Estimation and Reporting of Uncertainty Due to Discretization in CFD Applications. *J. fluids eng.*, 130(7), 078001. doi: 10.1115/1.2960953.

ANSYS. (2015). ANSYS CFX Solver Theory Guide, 16.0. Inc. ANSYS.

ASME. (2009). *V&V 20 - Standard for verification and validation in computational fluid dynamics and heat transfer*.

Bach, E., Mydlarski, L., Torriano, F., Charest-Fournier, J.-P., Sirois, H., Morissette, J.-F. & Hudon, C. (2015). PIV Characterization of the Air Flow in a Scale Model of a Hydrogenerator. *Asme 2015 power conf.*, pp. V001T12A003. doi: 10.1115/POWER2015-49124.

Baliga, B. R. & Patankar, S. V. (1980). A new finite-element formulation for convection-diffusion problems. *Numer. heat transf.*, 3(4), 393–409. doi: 10.1080/01495728008961767.

Blocken, B., Janssen, W. D. & van Hooff, T. (2012). CFD simulation for pedestrian wind comfort and wind safety in urban areas: General decision framework and case study for the Eindhoven University campus. *Environ. model. softw.*, 30, 15–34. doi: 10.1016/j.envsoft.2011.11.009.

Boglietti, A., Cavagnino, A., Staton, D., Shanel, M., Mueller, M. & Mejuto, C. (2009). Evolution and Modern Approaches for Thermal Analysis of Electrical Machines. *Ieee trans. ind. electron.*, 56(3), 871–882. doi: 10.1109/TIE.2008.2011622.

Bourgeois, J. A., Martinuzzi, R. J., Savory, E., Zhang, C. & Roberts, D. A. (2011). Assessment of Turbulence Model Predictions for an Aero-Engine Centrifugal Compressor. *J. turbomach.*, 133(1), 011025. doi: 10.1115/1.4001136.

CIGRE. (2003). *Survey of Hydrogenerator Failures*.

Coletti, F., Scialanga, M. & Arts, T. (2012). Experimental Investigation of Conjugate Heat Transfer in a Rib-Roughened Trailing Edge Channel With Crossing Jets. *J. turbomach.*, 134(4), 041016. doi: 10.1115/1.4003727.

Connor, P. H., Pickering, S. J., Gerada, C., Eastwick, C. N., Micallef, C. & Tighe, C. (2013). Computational fluid dynamics modelling of an entire synchronous generator for improved thermal management. *Iet electr. power appl.*, 7(3), 231–236. doi: 10.1049/iet-epa.2012.0278.

Cukurel, B. & Arts, T. (2013). Local Heat Transfer Dependency on Thermal Boundary Condition in Ribbed Cooling Channel Geometries. *J. heat transfer*, 135(10), 101001. doi: 10.1115/1.4024494.

Dang, D.-D., Pham, X.-T., Labbe, P., Torriano, F., Morissette, J.-F. & Hudon, C. (2018). CFD analysis of turbulent convective heat transfer in a hydro-generator rotor-stator system. *Appl. therm. eng.* doi: 10.1016/j.applthermaleng.2017.11.034.

Ferziger, J. H. & Peric, M. (2002). *Computational Methods for Fluid Dynamics*. Springer. doi: 10.1016/S0898-1221(03)90046-0.

Folting, C. & Jenau, F. (2014, sep). Implementation and analysis of multi-factor aging tests on the winding insulation of original sized generator stator bars used in large rotating machines. *2014 ichve int. conf. high volt. eng. appl.*, pp. 1–4. doi: 10.1109/ICHVE.2014.7035396.

Galpin, P., Broberg, R. & Hutchinson, B. (1995). Three-Dimensional Navier-Stokes Predictions of Steady State Rotor-Stator Interaction With Pitch Change. *Proc. 3rd annu. conf. cfd soc. canada*.

Hanimann, L., Mangani, L., Casartelli, E., Mokulys, T. & Mauri, S. (2014). Development of a Novel Mixing Plane Interface Using a Fully Implicit Averaging for Stage Analysis. *J. turbomach.*, 136(8), 081010. doi: 10.1115/1.4026323.

Hellsten, A. (1998). Some improvements in Menter's k-omega SST turbulence model. *29th aiaa, fluid dyn. conf.* doi: 10.2514/6.1998-2554.

Hettegger, M., Streibl, B., Biro, O. & Neudorfer, H. (2012). Measurements and Simulations of the Convective Heat Transfer Coefficients on the End Windings of an Electrical Machine. *Ieee trans. ind. electron.*, 59(5), 2299–2308. doi: 10.1109/TIE.2011.2161656.

Hosain, M. L., Bel Fdhila, R. & Rönnberg, K. (2017). Taylor-Couette flow and transient heat transfer inside the annulus air-gap of rotating electrical machines. *Appl. energy*, 207, 624–633. doi: 10.1016/j.apenergy.2017.07.011.

Howey, D. A., Holmes, A. S. & Pullen, K. R. (2011). Measurement and CFD Prediction of Heat Transfer in Air-Cooled Disc-Type Electrical Machines. *Ieee trans. ind. appl.*, 47(4), 1716–1723. doi: 10.1109/TIA.2011.2156371.

Howey, D. A., Childs, P. R. N. & Holmes, A. S. (2012). Air-Gap Convection in Rotating Electrical Machines. *Ieee trans. ind. electron.*, 59(3), 1367–1375. doi: 10.1109/TIE.2010.2100337.

Hydro-Québec. (2017). *Hydro-Québec's Annual Report 2017*. Consulted at http://www.hydroquebec.com/data/documents-donnees/pdf/annual-report.pdf.

Iaccarino, G., Ooi, A., Durbin, P. A. & Behnia, M. (2002). Conjugate heat transfer predictions in two-dimensional ribbed passages. *Int. j. heat fluid flow*, 23(3), 340–345. doi: 10.1016/S0142-727X(02)00181-9.

Internaltional Energy Agency. (2017). *World Energy Outlook 2017*. IEA. Consulted at http://www.oecd-ilibrary.org/energy/world-energy-outlook-2017{_}weo-2017-en.

Jamshidi, H., Nilsson, H. & Chernoray, V. (2015). CFD-based Design and Analysis of the Ventilation of an Electric Generator Model, Validated with Experiments. *Int. j. fluid mach. syst.*, 8(2), 113–123. doi: 10.5293/IJFMS.2015.8.2.113.

Jones, W. P. & Launder, B. E. (1973). The calculation of low-Reynolds-number phenomena with a two-equation model of turbulence. *Int. j. heat mass transf.* doi: 10.1016/0017-9310(73)90125-7.

Klomberg, S., Farnleitner, E., Kastner, G. & Bíró, O. (2015a). Validation of a heat transfer model for end winding bars of large hydro generators. *Compel - int. j. comput. math. electr. electron. eng.*, 34(5), 1589–1597. doi: 10.1108/COMPEL-02-2015-0060.

Klomberg, S., Farnleitner, E., Kastner, G. & Bíró, O. (2015b). Characteristics of the Convective Heat Transfer Coefficient at the End Winding of a Hydro Generator. *J. therm. sci. eng. appl.*, 7(1), 011011. doi: 10.1115/1.4028978.

Lancial, N., Torriano, F., Beaubert, F., Harmand, S. & Rolland, G. (2017). Taylor-Couette-Poiseuille flow and heat transfer in an annular channel with a slotted rotor. *Int. j. therm. sci.*, 112, 92–103. doi: 10.1016/j.ijthermalsci.2016.09.022.

Li, W., Yang, L., Ren, J. & Jiang, H. (2016). Effect of thermal boundary conditions and thermal conductivity on conjugate heat transfer performance in pin fin arrays. *Int. j. heat mass transf.*, 95, 579–592. doi: 10.1016/j.ijheatmasstransfer.2015.12.010.

Li, W., Li, D., Li, J. & Zhang, X. (2017). Influence of rotor radial ventilation ducts number on temperature distribution of rotor excitation winding and fluid flow state between two poles of a fully air-cooled hydro-generator. *Ieee trans. ind. electron.*, 64(5), 3767–3775. doi: 10.1109/TIE.2017.2650871.

Lim, T. T., New, T. H. & Luo, S. C. (2001). On the development of large-scale structures of a jet normal to a cross flow. *Phys. fluids*, 13(3), 770–775. doi: 10.1063/1.1347960.

Liu, Z. & Hill, D. L. (2000). Issues surrounding multiple frames of references models for turbo compressor applications. *Int. compress. eng. conf.*, 1–9.

Menter, F. R. (1994). Two-equation eddy-viscosity turbulence models for engineering applications. *Aiaa j.*, 32(8), 1598–1605. doi: 10.2514/3.12149.

Moffat, R. J. (1998). What's new in convective heat transfer? *Int. j. heat fluid flow*, 19(2), 90–101. doi: 10.1016/S0142-727X(97)10014-5.

Moradnia, P., Chernoray, V. & Nilsson, H. (2014a). Experimental assessment of a fully predictive CFD approach, for flow of cooling air in an electric generator. *Appl. energy*, 124, 223–230. doi: 10.1016/j.apenergy.2014.02.064.

Moradnia, P., Golubev, M., Chernoray, V. & Nilsson, H. (2014b). Flow of cooling air in an electric generator model - An experimental and numerical study. *Appl. energy*, 114, 644–653. doi: 10.1016/j.apenergy.2013.10.033.

Patankar, S. (1980). *Numerical heat transfer and fluid flow*. doi: 10.1016/j.watres.2009.11.010.

Pickering, S., Lampard, D. & Shanel, M. (2001). Modelling ventilation and cooling of the rotors of salient pole machines. *Iemdc 2001. ieee int. electr. mach. drives conf.*, pp. 806–808. doi: 10.1109/IEMDC.2001.939411.

Pickering, S., Lampard, D. & Shanel, M. (2002). Ventilation and heat transfer in a symmetrically ventilated salient pole synchronous machine. *Int. conf. power electron. mach. drives*, 2002, 462–467. doi: 10.1049/cp:20020161.

Raithby, G. D. & Schneider, G. E. (1979). Numerical solution of problems in incompressible fluid flow: Treatment of the velocity pressure coupling. *Numer. heat transf.*, 2(4), 417–440. doi: 10.1080/10407787908913423.

Rasekh, A., Sergeant, P. & Vierendeels, J. (2015). Convective heat transfer prediction in disk-type electrical machines. *Appl. therm. eng.*, 91, 778–790. doi: 10.1016/j.applthermaleng.2015.08.093.

Rasekh, A., Sergeant, P. & Vierendeels, J. (2017). Fully predictive heat transfer coefficient modeling of an axial flux permanent magnet synchronous machine with geometrical parameters of the magnets. *Appl. therm. eng.*, 110, 1343–1357. doi: 10.1016/j.applthermaleng.2016.09.019.

Schneider, G. E. & Raw, M. J. (1986). A skewed, positive influence coefficient upwinding procedure for control-volume-based finite-element convection-diffusion computation. *Numer. heat transf.*, 9(1), 1–26. doi: 10.1080/10407788608913462.

Schneider, G. E. & Raw, M. J. (1987). Control volume finite-element method for heat transfer and fluid flow using colocated variables- 1. computational procedure. *Numer. heat transf.*, 11(4), 363–390. doi: 10.1080/10407788708913560.

Schrittwieser, M., Marn, A., Farnleitner, E. & Kastner, G. (2014). Numerical Analysis of Heat Transfer and Flow of Stator Duct Models. *Ieee trans. ind. appl.*, 50(1), 226–233. doi: 10.1109/TIA.2013.2267191.

Shanel, M., Pickering, S. J. & Lampard, D. (2000). Application of Computational Fluid Dynamics to the Cooling of Salient Pole Electtical Machines. *Ieee int. electr. mach. drives conf. icem2000*.

Shanel, M., Pickering, S. J. & Lampard, D. (2003). Conjugate heat transfer analysis of a salient pole rotor in an air cooled synchronous generator. *Iemdc 2003 - ieee int. electr. mach. drives conf.*, 2, 737–741. doi: 10.1109/IEMDC.2003.1210318.

Stein, P., Pfoster, C., Sell, M., Galpin, P. & Hansen, T. (2015). Computational Fluid Dynamics Modeling of Low Pressure Steam Turbine Radial Diffuser Flow by Using a Novel Multiple Mixing Plane Based Coupling—Simulation and Validation. *J. eng. gas turbines power*, 138(4), 041604. doi: 10.1115/1.4031388.

Tennekes, H. (1972). *A First Course in Turbulence*. doi: 10.1017/S002211207321251X.

Torriano, F., Lancial, N., Lévesque, M., Rolland, G., Hudon, C., Beaubert, F., Morissette, J. F. & Harmand, S. (2014). Heat transfer coefficient distribution on the pole face of a hydrogenerator scale model. *Appl. therm. eng.* doi: 10.1016/j.applthermaleng.2014.04.048.

Toussaint, K., Torriano, F., Morissette, J.-F., Hudon, C. & Reggio, M. (2011). CFD Analysis of Ventilation Flow for a Scale Model Hydro-Generator. *Asme 2011 power conf. vol. 2*, pp. 627–637. doi: 10.1115/POWER2011-55202.

Traxler-Samek, G., Zickermann, R. & Schwery, A. (2010a). Cooling Airflow, Losses, and Temperatures in Large Air-Cooled Synchronous Machines. *Ieee trans. ind. electron.*, 57(1), 172–180. doi: 10.1109/TIE.2009.2031191.

Traxler-Samek, G., Zickermann, R. & Schwery, A. (2010b). Cooling airflow, losses, and temperatures in large air-cooled synchronous machines. *Ieee trans. ind. electron.*, 57(1), 172–180. doi: 10.1109/TIE.2009.2031191.

Venne, K., Mydlarski, L., Torriano, F., Charest-Fournier, J.-P., Hudon, C. & Morissette, J.-F. (2016). Design of an anemometer to characterize the flow in the ducts of a hydrogenerator rotor rim. *Aps div. fluid dyn. 2016*. Consulted at http://adsabs.harvard.edu/abs/2016APS..DFD.L4009V.

Versteeg, H. K. & Malalasekera, W. (2007). *An introduction to computational fluid dynamics : the finite volume method*. Pearson Education Ltd.

Wegner, B., Huai, Y. & Sadiki, A. (2004). Comparative study of turbulent mixing in jet in cross-flow configurations using LES. *Int. j. heat fluid flow*, 25(5), 767–775. doi: 10.1016/j.ijheatfluidflow.2004.05.015.

Weili, L., Chunwei, G. & Yuhong, C. (2013). Influence of rotation on rotor fluid and temperature distribution in a large air-cooled hydrogenerator. *Ieee trans. energy convers.*, 28(1), 117–124. doi: 10.1109/TEC.2012.2220852.

Wilcox, D. C. (1988). Reassessment of the scale-determining equation for advanced turbulence models. *Aiaa j.*, 26(11), 1299–1310. doi: 10.2514/3.10041.

Wilcox, D. (1993). *Turbulence modeling for CFD*. doi: 0963605151.

Yakhot, V., Orszag, S. A., Thangam, S., Gatski, T. B. & Speziale, C. G. (1992). Development of turbulence models for shear flows by a double expansion technique. *Phys. fluids a fluid dyn.*, 4(7), 1510–1520. doi: 10.1063/1.858424.